UNIVERSITY OF CALIFORNIA, SAN DIEGO

Vibration Suppression, Stabilization, Motion Planning and Tracking for Flexible Beams

A Dissertation submitted in partial satisfaction of the requirements for the degree Doctor of Philosophy

in

Engineering Sciences (Mechanical Engineering)

by

Antranik Antonio Siranosian

Committee in charge:

Professor Miroslav Krstic, Chair
Professor Joel Conte
Professor Raymond de Callafon
Professor Robert Skelton
Professor Michael Todd

2009

The Dissertation of Antranik Antonio Siranosian is approved, and it is acceptable in quality and form for publication on microfilm and electronically:

_____

_____

_____

_____

_____
Chair

University of California, San Diego

2009

To my family.

TABLE OF CONTENTS

LIST OF FIGURES

LIST OF TABLES

ACKNOWLEDGEMENTS

This dissertation is the product of the work and support of many people and I am extremely grateful to all who have had an influence throughout the years. First, I would like to express my gratitude to my advisor Professor Miroslav Krstic for his excellent guidance and mentoring in all facets of my research.

I would like to thank my parents Antonio and Isabel, my sisters Veronica and Maro, and brother Haig for all the years of love, support and encouragement.

I would like to thank my fiancé Jennifer Bogosian for her unending love, support and friendship while I spent most weekdays about a hundred miles away.

I would like to thank Dr. Matt Bement, from the Los Alamos National Laboratory, for providing motivation for my research topic and for his time and effort in supporting the experimental aspects of my work. I would also like to thank the Los Alamos National Laboratory for providing financial support, and Kathie Womack for all her help with my trips to the lab.

I would like to thank the members of my committee for their helpful questions and comments.

I would like to thank my uncle Ago and aunt Tere for giving me a place to stay.

I would like to thank my fellow graduate students Andrey Smyshlyaev, Jennie Cochran, Nima Ghods, Nick Killingsworth, Rafael Vazquez, Charles Kinney, and Chunlei Zhang for their many helpful discussions. I would also like to thank Jennie, Nima, Paul Frihauf, Jamie Gray, and James Krieger for providing a fun and positive research environment.

I would like to thank Jeff Butterworth, Anne Katherine Butterworth, Keunmo Kang, Charles Kinney, Sierra Kinney, and Joe Moore for being great friends.

I am grateful to Professor Kevin Anderson from Cal Poly Pomona for introducing me to the field of control systems, and encouraging me to pursue a master degree and Ph.D.

This dissertation includes reprints or adaptations of the following papers:
A. A. Siranosian, M. Krstic, A. Smyshlyaev, and M. Bement, "Motion Planning and Tracking for Tip Displacement and Deflection Angle for Flexible Beams," *ASME Journal of Dynamic Systems, Measurement and Control*, to appear. (Chapter 3)

A. A. Siranosian, M. Krstic, A. Smyshlyaev, and M. Bement "Gain Scheduling-Inspired Control for Nonlinear PDEs," submitted to the *ASME Journal of Dynamic Systems, Measurement and Control*. (Chapter 4)

A. A. Siranosian, M. Krstic, and M. Bement, "Generation and Tracking of Sinusoids for Shake Table Control via Extremum Seeking," *Proc. of the ASME International Mechanical Engineering Congress and Exposition*, 2007. (Chapter 6)

C. Zhang, A. A. Siranosian, and M. Krstic, "Extremum Seeking for Moderately Unstable Systems and for Autonomous Vehicle Target Tracking Without Position Measurements," *Automatica*, vol. 43, pp. 1832-1839, 2007. (Appendix A)

VITA

2003	B.S. in Mechanical Engineering, California State Polytechnic University, Pomona
2005	Teaching Assistant, Department of Mechanical Engineering, University of California, San Diego
2005	M.S. in Engineering Sciences (Mechanical Engineering), University of California, San Diego
2009	Ph.D. in Engineering Sciences (Mechanical Engineering), University of California, San Diego

PUBLICATIONS

A. A. Siranosian, M. Krstic and M. Bement, "Generation and Tracking of Sinusoids for Shake Table Control via Extremum Seeking," *Proc. of the ASME International Mechanical Engineering Congress and Exposition*, 2007.

C. Zhang, A. A. Siranosian, and M. Krstic, "Extremum Seeking for Moderately Unstable Systems and for Autonomous Vehicle Target Tracking Without Position Measurements," *Automatica*, vol. 43, pp. 1832-1839, 2007.

C. Zhang, D. Arnold, N. Ghods, A. A. Siranosian and M. Krstic, "Source Seeking with Non-Holonomic Unicycle Without Position Measurement and With Tuning of Forward Velocity," *Systems & Control Letters*, vol. 56, issue 3, 245–252, 2007.

J. Cochran, N. Ghods, A. A. Siranosian, and M. Krstic, "3D Source Seeking for Underactuated Vehicles without Position Measurement," *IEEE Transactions on Robotics*, to appear.

A. A. Siranosian, M. Krstic, A. Smyshlyaev, and M. Bement, "Motion Planning and Tracking for Tip Displacement and Deflection Angle for Fexible Beams," *ASME JDSMC*, to appear.

A. A. Siranosian, M. Krstic, A. Smyshlyaev and M. Bement, "Gain Scheduling-Inspired Control for Nonlinear PDEs," submitted to the *ASME JDSMC*.

ABSTRACT OF THE DISSERTATION

Vibration Suppression, Stabilization,
Motion Planning and Tracking for Flexible Beams

by

Antranik Antonio Siranosian
Doctor of Philosophy in Engineering Sciences (Mechanical Engineering)
University of California San Diego, 2009
Professor Miroslav Krstic, Chair

The problems of vibration suppression, stabilization, motion planning, and tracking for flexible beams are important for many practical mechanical systems, such as the cantilevered beam in an atomic force microscope, a solar panel array on a satellite, the boom on a crane, or a structure mounted on a shake table. This work approaches the aforementioned control design problems using two methods; backstepping for partial differential equations (PDEs), and extremum seeking.

PDE backstepping is a form of model reference control for infinite dimensional systems where boundary control is used to make a closed-loop system perform like a target system, which is the reference model with desirable performance characteristics. Infinite dimensional state transformations, relating plant and target systems, are the key to PDE backstepping designs and are used to find the desired boundary controllers. PDE backstepping techniques are presented for motion planning and tracking for the string and shear beam with Kelvin-Voigt (KV) damping, and a combination of PDE backstepping and gain scheduling is presented for extending linear PDE backstepping techniques to stabilization, motion planning, and tracking for the string and shear beam with KV damping and boundary-displacement dependent free-end nonlinearities. Explicit motion planning reference solutions for the shear beam are found, using backstepping transformations, as a function of the target system reference solution, which itself is a function of the string solution. The

string solution is the easiest to find, and is done using traditional motion planning tools. Tracking controllers are found as a combination of vibration suppression and motion planning controllers. Gain scheduling is a method that replaces nonlinear control design with the design of a family of linear controllers. When combined with linear PDE backstepping techniques, it provides a means of extending vibration suppression, stabilization, motion planning and tracking results to the string and shear beam with free-end nonlinearities. Gain scheduling based designs, which produce locally stabilizing controllers parameterized by a function of the nonlinearity, are a more simple and manageable alternative to full-state feedback linearizing nonlinear PDE control designs.

Extremum seeking (ES) is a non-model based method used for tuning parameter(s) to optimize an unknown nonlinear map. ES tuning for positive-position-feedback compensators is presented as a method of selecting the parameter(s) of the compensator to improve vibration suppression on a mechanical system forced by a persistent sinusoidal disturbance. ES tuning for motion planning and tracking is presented as a method for tuning the amplitude and phase of a sinusoidal input to a stable linear plant to generate and track a sinusoid of desired amplitude and phase at the output.

1

Introduction

Vibration suppression, stabilization, motion planning and tracking for flexible beams are important control problems for many practical mechanical systems, such as the cantilevered beam in an atomic force microscope, an array of solar panels deployed on a satellite, or the boom on a crane. Particular motivation for this work comes from a shake table control problem for the Los Alamos National Laboratory where a shake table is used to actuate the base of a flexible structure in order to impart a desired motion near the structure's free-end. Motivation also comes from an experimental testbed provided by the laboratory, on which control designs could be implemented. This work addresses the aforementioned control problems via two approaches. The first approach employs backstepping techniques for partial differential equations (PDEs), while the second approach uses extremum seeking techniques to tune the parameters of finite dimensional compensators.

PDE backstepping is a form of model reference control for infinite dimensional systems where the open-loop system is related to a target system—a reference model with desirable performance characteristics—using infinite dimensional state transformations. The same state transformations are then used to find the desired boundary controllers. Advantages of using PDE backstepping theory is that the design can be done for an infinite dimensional system without having to discretize and truncate the model, and it allows for the design of non-collocated controllers that use actuation at the base and sensing at the free-end. This work expands on previous results for vibration suppression for linear string and shear beam PDEs, with

Kelvin-Voigt damping, in two ways. First, a combination of motion planning and PDE backstepping tools has been employed for the formulation of explicit motion planning reference solutions for the tip displacement (string, target system, and shear beam) and tip deflection angle (shear beam) using only actuation at the base. PDE backstepping tools simplify the problem of finding reference solutions for the shear beam by using transformations to relate the string reference solution, which is the easiest to find, to the target system, and then to the beam. Second, PDE backstepping tools for linear systems have been extended to nonlinear PDEs using gain scheduling techniques. Gain scheduling is a technique that replaces nonlinear control design with the design of a family of linear controllers that are applied according to a scheduling signal. The combination of gain scheduling and linear PDE backstepping tools provides a more simple and manageable design alternative for the challenging problem of nonlinear control design for PDEs, as compared to exactly linearizing nonlinear full-state feedback. The resulting gain scheduling based designs in this work are not scheduled in the traditional sense, rather they are implemented as nonlinear controllers (linear PDE backstepping controllers with boundary-value dependent gains).

Extremum seeking (ES) is a non-model based adaptive control technique for tuning parameters to optimize an unknown nonlinear map. ES relies on persistency of excitation—usually a sinusoid—to perturb the parameters being tuned in order to quantify their effects on the output of the nonlinear map, then uses that information to generate estimates of the optimal parameter values. This work presents two applications of extremum seeking. The first employs ES to tune the parameter of a positive-position-feedback compensator for improved vibration suppression for a system forced by a sinusoidal disturbance. The second employs it to tune the parameters of a sinusoidal input in order to generate and track a sinusoid at the output of an unknown, stable plant.

1.1 Thesis Overview

This section outlines the contents of this thesis.

Chapter 2 presents the experimental testbed provided by the Los Alamos National Laboratory, and its analytical modeling and experimental identification by trial-and-error.

Chapter 3 presents explicit motion planning reference solutions, and tracking results for the string and shear beam PDEs with Kelvin-Voigt damping using PDE backstepping techniques.

Chapter 4 presents gain scheduling-inspired control designs for the stabilization of nonlinear PDEs. The control design, with a result for local exponential stability of the origin of a closed-loop system, is presented for a benchmark first-order hyperbolic PDE with boundary-value dependent in-domain nonlinearity. The design is then applied to the string and shear beam with Kelvin-Voigt damping and boundary-displacement dependent free-end nonlinearity.

Chapter 5 presents an extremum seeking based design for the real-time tuning of the parameter of a positive-position-feedback compensator. The compensator is used to suppress vibrations on a system forced by a sinusoidal disturbance.

Chapter 6 presents an extremum seeking based design for the generation and tracking of a sinusoid at the output of a stable linear system. Motion planning is done by assuming a sinusoidal form for the system input, then extremum seeking is used to tune its amplitude and phase.

Chapter 7 summarizes the results of this thesis, and presents concluding remarks.

Appendix A presents results for the extremum seeking control of a point mass for target tracking without position measurements.

Appendix B presents experimental results for active vibration absorbers applied to the testbed.

2

Modeling and Identification of a Shake Table-Specimen Testbed

This chapter presents the experimental testbed provided by the Los Alamos National Laboratory (LANL), and its analytical modeling and experimental identification by trial-and-error. Figure 2.1 shows the testbed with an electrodynamic shaker attached to a cantilevered beam. Locally hardening or softening nonlinearities can be introduced by arranging magnets around the free-end of the beam, which has magnets or steel plates attached to it. The testbed captures pertinent characteristics of a LANL shake table with specimen. The work done in modeling the cantilevered beam helped to gain an understanding of flexible beams and their models, which are used in Chapters 3 and 4. Experimental identification of the testbed proved to be a valuable learning experience and provided insights to the its characteristics, which were used for the work in Chapter 6 and Appendix B.

The testbed is composed of an Aluminum cantilevered beam with nominal dimensions 15 in $\times$ 2 in $\times$ 0.088 in (380 mm $\times$ 50 mm $\times$ 2.24 mm). The beam is forced by in-domain actuation, approximately five inches (127 mm) from the base, by an electrodynamic shaker [49]. Piezoelectric accelerometers [81] can be placed at desired locations on the beam, depending on what is chosen as the testbed output. Not shown are a linear power amplifier [79], signal conditioner and data acquisition system [80], and host and target computers. Matlab and Simulink are used on the

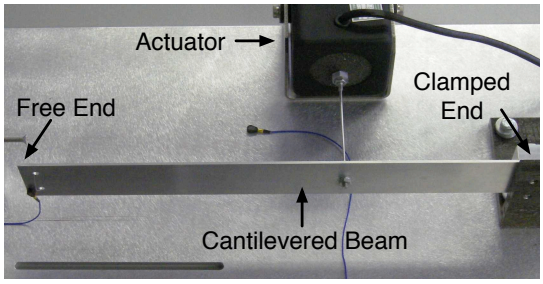

Figure 2.1: Photograph of testbed showing the cantilevered beam attached to the electrodynamic shaker/actuator. Also shown is an accelerometer placed at the free end of the beam.

host computer to design experiments to be run on the testbed. The xPC Target toolbox is used to interface the Matlab code with data acquisition hardware in the target computer. Matlab translates the Simulink block diagrams into executable code that is downloaded and run on the target computer.

This chapter is organized as follows. Section 2.1 presents the analytical modeling of the electrodynamic shaker, cantilevered beam, nonlinear interaction force, and testbed (shaker attached to beam, with possible nonlinearities). Section 2.2 presents the compilation of parameter values for the models in Section 2.1, along with the experimental identification of the amplifier, shaker, cantilevered beam, and testbed (amplifier, shaker attached to beam, with possible nonlinearities).

2.1 Analytical Modeling

2.1.1 Electrodynamic Shaker

An electrodynamic shaker is an electromechanical device whose operation is similar to a that of a loudspeaker. Current is passed through coils wound on an armature, which produces an electro-magnetic field that interacts with a magnetic field produced by permanent magnets in the shaker housing. The interaction between the electro-magnetic and magnetic fields causes translation of the armature, which is supported on springs mounted in the shaker body.

The dimensional shaker dynamics are [13]

$$i^*_{t^*}(t^*) = -\frac{1}{L^*_s}(R^* i^*(t^*) + B^* l^* y^*_{t^*}(t^*)) + \frac{1}{L^*_s} v^*(t^*) \tag{2.1}$$

$$y^*_{t^*t^*}(t^*) = -\frac{1}{m^*}(d^*_s y^*_{t^*}(t^*) + k^*_s y^*(t^*)) + \frac{B^* l^*}{m^*} i^*(t^*)\,, \tag{2.2}$$

where B^* is the air-gap flux density in teslas (T), L^*_s is the armature coil inductance in henries (H), R^* is the armature coil resistance in ohms (Ω), d^*_s is the shaker damping coefficient in newton-seconds-per-meter (N·s/m), k^*_s is the shaker spring constant in newtons-per-meter (N/m), l^* is the armature coil length in meters (m), m^* is the mass of the shaker armature (including any attached hardware) in kilograms (kg), t^* is time in seconds (s), $v^*(t^*)$ is the input to the shaker in volts (V), $i^*(t^*)$ is the armature current in amperes (A), and $y^*(t^*)$ is the armature displacement in meters (m). The superscript $*$ signifies dimensional parameters. The subscript t^* denotes a derivative with respect to time. The dimensional shaker transfer function, from the input voltage $v^*(t^*)$ to the armature displacement $y^*(t^*)$, is

$$\frac{Y^*(s)}{V^*(s)} = \frac{B^* l^*}{(m^* s^2 + d^*_s s + k^*_s)(L^*_s s + R^*) + (B^* l^*)^2 s} \tag{2.3}$$

$$= \frac{\frac{B^* l^*}{m^* L^*_s}}{s^3 + \left(\frac{R^*}{L^*_s} + \frac{d^*_s}{m^*}\right) s^2 + \left(\frac{R^* d^*_s}{L^*_s m^*} + \frac{(B^* l^*)^2}{L^*_s m^*} + \frac{k^*_s}{m^*}\right) s + \frac{R^* k^*_s}{L^*_s m^*}}\,, \tag{2.4}$$

where $V^*(s)$ and $Y^*(s)$ represent the Laplace transforms of $v^*(t^*)$ and $y^*(t^*)$.

The nondimensionalized shaker dynamics are

$$i_t(t) = -\frac{1}{L_s}(R i(t) + y_t(t)) + \frac{1}{L_s} v(t) \tag{2.5}$$

$$y_{tt}(t) = -(d_s y_t(t) + y(t)) + i(t)\,, \tag{2.6}$$

where the dimensionless parameters are defined as $L_s = \frac{L^*_s k^*}{B^{*2} l^{*2}}$, $R = \frac{R^* \sqrt{k^*_s m^*}}{B^{*2} l^{*2}}$, $d_s = \frac{d^*_s}{\sqrt{k^*_s m^*}}$, $i = \frac{i^* B^*}{k^*}$, $t = t^* \sqrt{\frac{k^*}{m^*}}$, $v = \frac{v^*}{B^* l^{*2}} \sqrt{\frac{m^*}{k^*}}$, and $y = \frac{y^*}{l^*}$. The nondimensional shaker transfer function is

$$\frac{Y(s)}{V(s)} = \frac{1}{(s^2 + d_s s + 1)(L_s s + R) + s} \tag{2.7}$$

$$= \frac{\frac{1}{L_s}}{s^3 + \left(\frac{R}{L_s} + d_s\right) s^2 + \left(1 + \frac{1}{L_s} + \frac{d_s R}{L_s}\right) s + \frac{R}{L_s}}\,. \tag{2.8}$$

2.1.2 Cantilevered Beam

The cantilevered beam is modeled as a Timoshenko beam with Kelvin-Voigt damping (internal material damping)—which is the most complete and accurate of the beam models—and is written as two coupled wave equations (second-order-in-time, second-order-in-space partial differential equations). The dimensional model for a beam that is free at the tip $x^* = 0$ and clamped at the base $x^* = L^*$ is [74, 91]

$$\begin{aligned}
\rho^* A^* u^*_{t^*t^*}(x^*,t^*) &= kA^*G^*(1+d^*\partial_{t^*})\left\{u^*_{x^*x^*}(x^*,t^*) - \alpha_{x^*}(x^*,t^*)\right\} && (2.9)\\
\rho^* I^* \alpha_{t^*t^*}(x^*,t^*) &= (1+d^*\partial_{t^*})\left\{E^*I^*\alpha_{x^*x^*}(x^*,t^*)\right. \\
&\quad \left. + kA^*G^*(u^*_{x^*}(x^*,t^*) - \alpha(x^*,t^*))\right\} && (2.10)\\
u^*_{x^*}(0,t) &= kA^*G^*\alpha(0,t) && (2.11)\\
\alpha_{x^*}(0,t) &= 0 && (2.12)\\
u^*(L^*,t) &= 0 && (2.13)\\
\alpha(L^*,t) &= 0\,, && (2.14)
\end{aligned}$$

where A^* is the cross-sectional area in square-meters (m^2), E^* is Young's modulus (modulus of elasticity) in newtons-per-meter-squared ($\mathrm{N/m}^2$), G^* is shear modulus in newtons-per-meter-squared ($\mathrm{N/m}^2$), I^* is the moment of inertia of the cross-section about the neutral axis in quartic-meters (m^4), L^* is the length of the beam in meters (m), d^* is the Kelvin-Voigt damping coefficient in seconds (s), k is the shape factor, ρ^* is the material density in kilograms-per-meter-cubed ($\mathrm{kg/m}^3$), t^* is time in seconds (s), x^* is the axial location along the beam in meters (m), $u^*(x^*,t^*)$ is the transverse displacement of the beam in meters (m), and $\alpha(x^*,t^*)$ is the angle of rotation due to the bending moment in radians (rad). The subscripts t^* and x^* denote partial derivatives with respect to time and space, respectively. The shape factor depends on the cross-section, which for a rectangular cross-section is given by [32] $k = \frac{10(1+\nu)}{12+11\nu}$ where Poisson's ratio $\nu = -\frac{\epsilon_y}{\epsilon_x} = -\frac{\epsilon_z}{\epsilon_x}$ is the ratio of the induced strains ϵ_y and ϵ_z and the primary strain ϵ_x assuming the deforming force is applied along the x-axis, and is constant during elastic deformation [74].

The nondimensionalized Timoshenko beam model is [32, 91]

$$\rho A u_{tt}(x,t) = kAG(1+d\partial_t)\left\{u_{xx}(x,t) - \alpha_x(x,t)\right\} \qquad (2.15)$$

$$\begin{aligned}
\rho I \alpha_{tt}(x,t) &= (1 + d\partial_t)\left\{\alpha_{xx}(x,t) + kAG(u_x(x,t) - \alpha(x,t))\right\} && (2.16)\\
u_x(0,t) &= \alpha(0,t) && (2.17)\\
\alpha_x(0,t) &= 0 && (2.18)\\
u(1,t) &= 0 && (2.19)\\
\alpha(1,t) &= 0\,, && (2.20)
\end{aligned}$$

where the dimensionless parameters are defined as $A = \frac{A^*}{L^{*2}}$, $G = \frac{G^* L^{*4}}{E^* I^*}$, $I = \frac{I^*}{L^{*4}}$, $L = \frac{L^*}{L^*}$, $d = d^*\omega_1^*$, $t = t^*\omega_1^*$, $u = \frac{u^*}{L^*}$, $x = \frac{x^*}{L^*}$, $\rho = \rho^* \frac{L^{*6}\omega_1^{*2}}{E^* I^*}$, where ω_1^* is the first natural frequency of the beam in radians per second. A parameterized version of the dimensionless Timoshenko beam model can be written as [43, 44]

$$\begin{aligned}
\varepsilon u_{tt}(x,t) &= (1 + d\partial_t)\left\{u_{xx}(x,t) - \alpha_x(x,t)\right\} && (2.21)\\
\mu\varepsilon \alpha_{tt}(x,t) &= (1 + d\partial_t)\left\{\varepsilon\alpha_{xx}(x,t) + a(u_x(x,t) - \alpha(x,t))\right\} && (2.22)\\
u_x(0,t) &= \alpha(0,t) && (2.23)\\
\alpha_x(0,t) &= 0 && (2.24)\\
u(1,t) &= 0 && (2.25)\\
\alpha(1,t) &= 0\,, && (2.26)
\end{aligned}$$

where $a = \rho A = \frac{\rho^* \omega_1^{*2} L^{*4} A^*}{E^* I^*}$, $\varepsilon = \frac{\rho}{kG} = \frac{\rho^* \omega_1^{*2} L^{*2}}{kG^*}$, and $\mu = \rho I = \frac{\rho^* \omega_1^{*2} L^{*2}}{E^*}$. Figure 2.2 shows the relationships between the displacement $u(x,t)$, slope $u_x(x,t)$, and deflection angle $\alpha(x,t)$.

2.1.3 Nonlinear Interaction Force

Figure 2.3 shows a drawing depicting the top view of the testbed, focusing on the nonlinear interaction. The x-axis corresponds to the displacement of the beam tip, the y-axis is colinear with the neutral axis of the beam, r_1 and r_2 are the distances from the steel located at $(x, 0)$ to the magnets located at $(x_1, y_1) = (a_1, b_1)$ and $(x_2, y_2) = (-a_2, b_2)$, the constants k_1^{nl}, k_2^{nl} are proportional to the pull force for each magnet, and f is the interaction force in the x-axis. The interaction of stationary magnets with steel/magnets attached to the beam tip suggests dynamic characteristics of the magnetic field and the tip force it induces, however for low enough

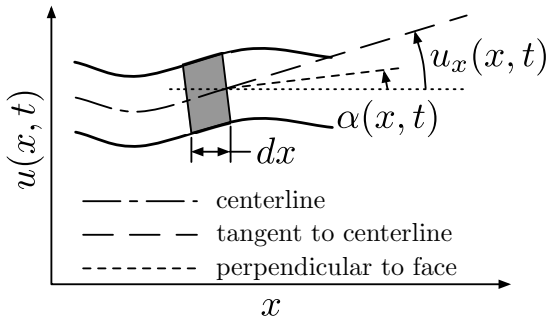

Figure 2.2: A differential element of length dx in the Timoshenko beam. The diagram shows the relationship between the beam displacement $u(x,t)$, the slope $u_x(x,t)$ and the deflection angle $\alpha(x,t)$. This diagram has been adapted from a figure in [74].

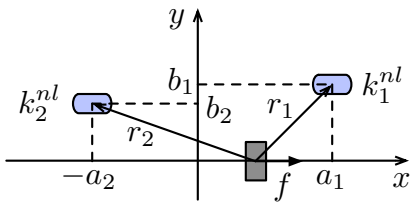

Figure 2.3: Top view of the geometry of the testbed nonlinearity. The neutral axis of the cantilevered beam is colinear to the y-axis. The steel or magnets placed at the tip of the beam displace in the x-axis, while the magnets at (a_1, b_1) and $(-a_2, b_2)$ are stationary.

natural frequencies of the testbed the interaction can be modeled as a magnetostatic phenomenon [37]. Also, the magnet/steel-magnet interaction force is expected to behave inversely proportional to a power of the relative distance between the magnets on the testbed table and steel-magnets at the beam tip. Qualitatively, the force is expected to increase as the tip of the beam approaches the magnet, drop to zero when the tip of the beam is directly under the magnet, then change signs and follow a similar trend as the tip passes below the magnet and moves away.

The total force f acting on the steel in the x-axis will be the sum of the x-components of the forces caused by each magnet, and can be written as $f = f_{1x} + f_{2x}$. The form of the individual force f_i, acting in the direction of r_i, is postulated as $f_i = \frac{k_i^{nl}}{r_i^n}$. Using the geometry of the problem, the magnitude of f_i in the x-direction

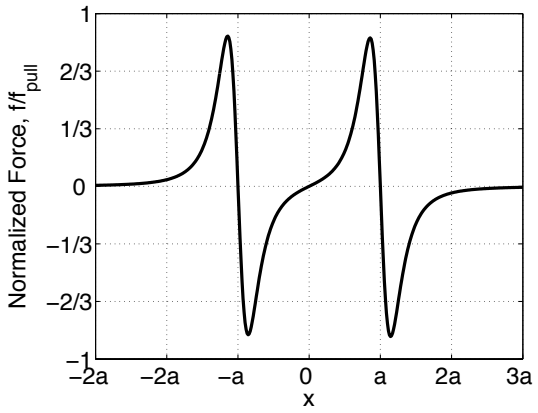

Figure 2.4: Plot of the nonlinear interaction force f as a function of the tip displacement x, for magnets placed at (a,b) and (-a,b). The interaction force has been normalized by the pull force.

is given by $f_{ix} = \frac{k_i^{nl}}{r_i^n}\frac{x_i - x}{r_i}$ where $r_i = \sqrt{(x_i - x)^2 + y_i^2}$. The expression for the total force given the magnet locations $(x_1, y_1) = (a_1, b_1)$ and $(x_2, y_2) = (-a_2, b_2)$ is then

$$f(x) = \frac{k_1^{nl}\,(a_1 - x)}{\left((a_1 - x)^2 + b_1^2\right)^{\frac{n+1}{2}}} - \frac{k_2^{nl}\,(a_2 + x)}{\left((a_2 + x)^2 + b_2^2\right)^{\frac{n+1}{2}}}\,. \tag{2.27}$$

Depending on the application, this model can be used as dimensional or dimensionless.

Figure 2.4 is a plot of the total x-direction interaction f, normalized by the maximum pull force f_{pull} (the force required to pull a magnet away from a steel plate) as a function of tip displacement x, for a pair of magnets of arbitrary strength placed symmetrically about the y-axis at (a, b), $(-a, b)$. The plot shows that the model (2.27) captures the expected behavior of the interaction force as the tip of the beam moves across the magnets.

2.1.4 Testbed

The dimensional testbed model is derived by combining the shaker model (2.1), (2.2), beam model (2.9)–(2.12) with $u^*(L^*, t)$ and $\alpha(L^*, t)$ actuated.

The nondimensional testbed model is

$$i_t(t) = -\frac{1}{L_s}(Ri(t) + y_t(t)) + \frac{1}{L_s}v(t) \tag{2.28}$$

$$y_{tt}(t) = -(d_s y_t(t) + k_s y(t)) + li(t)\,, \tag{2.29}$$

with (2.21)–(2.24), and $u(1,t)$ and $\alpha(1,t)$ actuated, and the redefined nondimensional shaker parameters $L_s = \frac{L_s^* \omega_1^* m^*}{B^{*2} L^{*2}}$, $R = \frac{R^* \omega_1^* m^*}{B^{*2} L^{*2}}$, $d_s = \frac{d^*}{\omega_1^* m^*}$, $k_s = \frac{k_s^*}{m^* \omega_1^{*2}}$, $l = \frac{l^*}{L^*}$, $i = \frac{i^* B^*}{\omega_1^{*2} m^*}$, $v = \frac{v^*}{B^* L^{*2} \omega_1^*}$, $t = t^* \omega_1^*$, $y = \frac{y^*}{L^*}$, with ω_1^* redefined as the first natural frequency of the testbed.

State dependent nonlinearities acting on the beam tip are accounted for by augmenting the boundary condition (2.23) with the additive term $f\left(u(0,t)\right)$, i.e. $u_x(0,t) = \alpha(0,t) + f\left(u(0,t)\right)$. Depending on the sign of $f'\left(u(0,t)\right) = \frac{df(u(0,t))}{du(0,t)}$, the nonlinearity can either have positive stiffness ($f' > 0$) or negative stiffness ($f' < 0$).

2.2 Identification

This section discusses the parameter selection for the analytical models presented in the previous section, and trial-and-error experimental identification of the testbed and its individual components. Parameters for the shaker and cantilevered-beam models were measured, given by manufacturer's specifications, or found in the literature.

Experimental identification by trial-and-error was done for the amplifier, shaker, and testbed based on magnitude-frequency and phase-frequency (Bode) plots generated from experimental data. First, output data was recorded for a sine sweep input. Then a discrete Fourier transform was performed on the collected input and output data, and the ratio of the transformed data was used to compute the magnitude and phase relationships from input to output. Observations of the experimental magnitude-frequency and phase-frequency plots were used to find the form of a transfer function or finite dimensional model, whose parameters were then chosen based on trial-and-error comparisons of the experimental and identified models. This work was done without a formal education in experimental system identification techniques. All identification has been done for the physical, dimensional systems. The superscript-star has been omitted for clarity.

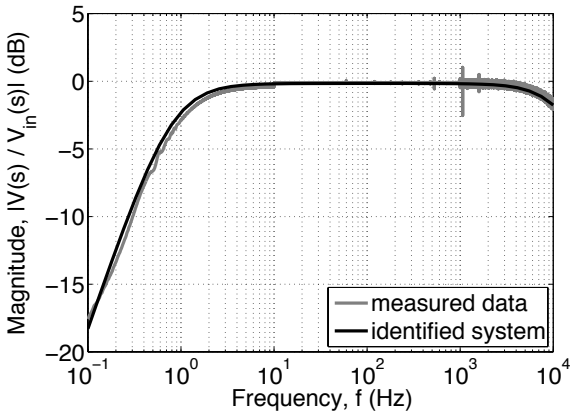

Figure 2.5: Comparison of experimental and identified amplifier input-voltage-to-output-voltage magnitude-frequency plots.

2.2.1 Amplifier

Experimental Identification by Trial-and-Error

Input data was generated by the target PC. Output data was measured by a probe connected to the output (load) on the back panel of the amplifier, and collected by the target PC. The data was produced with three sine sweeps in the frequency ranges 10^{-1}–10^{1} Hz, 10^{1}–10^{3} Hz and 10^{3}–10^{4} Hz. The sampling rate in the first two ranges was chosen to be ten times the upper limit in each range, i.e., 10^{2} Hz and 10^{4} Hz respectively. The sampling rate in the last range was chosen to be 2×10^{4} Hz, based on the minimum acceptable rate needed to accurately measure the highest frequency signals [26] and the limitations of the data acquisition system.

Figure 2.5 shows the experimental and identified amplifier input-voltage-to-output-voltage magnitude-frequency plots. The experimental data has a low frequency slope of positive twenty decibels-per-decade. It then levels off around ten hertz and stays level until around one-thousand hertz. Lastly, it drops off at an estimated slope of negative twenty decibels-per-decade. Based on these observations, and knowledge of the frequency response of linear systems, the amplifier transfer function has the form

$$\frac{V(s)}{V_{in}(s)} = \frac{Ks}{(s + 2\pi f_1)(s + 2\pi f_2)}, \tag{2.30}$$

where V_{in} is the input voltage to the amplifier, V is the amplifier output voltage, $K > 0$ is a constant gain, $f_1 > 0$ is the frequency at which the magnitude first levels off, and $f_2 > 0$ is the frequency at which the magnitude drops off. The gain K is arbitrary, in the sense that it depends on a gain adjustment dial located on the front panel of the amplifier. For all experiments, the dial was set such that the amplifier transfer function had unity gain in the frequency range 10^1–10^3 Hz. The model values, based on trial-and-error estimates, were found to be $K = 92.5 \times 10^3$, $f_1 = 0.8$ Hz and $f_2 = 15 \times 10^3$ Hz. The measured and estimated magnitude-frequency plots agree with the performance data provided by the manufacturer [79].

2.2.2 Electrodynamic Shaker

Parameter Selection

The nondimensional shaker parameters are $L_s = \frac{L_s^* \omega_1^* m^*}{B^{*2} L^{*2}}$, $R = \frac{R^* \omega_1^* m^*}{B^{*2} L^{*2}}$, $d_s = \frac{d_s^*}{\omega_1^* m^*}$, $k_s = \frac{k_s^*}{m^* \omega_1^{*2}}$, and $l = \frac{l^*}{L^*}$, which require identification of dimensional physical properties of the shaker electronics (air-gap flux density B^*, armature coil inductance L_s^*, armature coil resistance R^*, armature coil length l^*) and mechanical sub-system (damping coefficient d_s^*, spring constant k_s^*, mass of armature with attachment m^*), as well as the first natural frequency ω_1^* and length L^* of the beam. Beam parameters appear in the nondimensional shaker values, since the nondimensionalization was done for the testbed as a whole.

Table 2.1 summarizes the manufacturer specified, computed and measured dimensional shaker properties. The armature coil inductance L_s^*, armature mass m^* and the force-to-current ratio F^*/i^* were given by manufacturer's specifications [49, 53]. The product $B^* l^*$ was computed using the manufacturer's specification of $F^*/i^* = 1.38$ lbf/A and the force-current relationship $F^* = 2.54^2 K_1 i^* B^* l^*$ [49]. The armature coil resistance R^* was measured with an ohmmeter. The spring constant k_s^* was measured experimentally using a pull scale to measure force, a ruler to measure displacement, and a linear proportional relationship to relate the applied force and resulting displacement to the spring constant k_s^*.

Table 2.1: Manufacturer's specifications, computed properties and measured properties of the electrodynamic shaker.

Manufacturer's Specifications	
L_s^*, H	$0.28 \times 10^{-}3$
m^*, kg (lbm)	0.031 (0.069)
Computed Properties	
B^*l^*, T·m (T·in)	6.14 (242)
Measured Properties	
R^*, Ω	1.6
k_s^*, N/m (lbf/in)	2940 (16.8)

Experimental Identification by Trial-and-Error

An estimate of the shaker damping d_s^* was to be made by comparing the experimental shaker Bode plot to that of the shaker transfer function (2.4), but a comparison of the plots showed that the analytical model did not match the experimental data. The source of the discrepancy was that R^* and L_s^* were assumed to be static parameters, but were in fact functions of the input voltage frequency [13]. While one option was to estimate $R^* = R^*(\omega^*)$ and $L_s^* = L_s^*(\omega^*)$ [13], the simple solution was to group their effects into the shaker transfer function. Therefore, a new transfer function was derived for the input-output characteristics of the shaker based on the experimental magnitude-frequency data.

Experiments were conducted with the shaker disconnected from the beam. The data generation method used for the amplifier-shaker system, was similar to that used for the amplifier. Input data was generated and collected by the target PC. Output data was collected with an accelerometer attached to the shaker armature. Sine sweeps were used to produce data in the overlapping frequency ranges 10^{-1}–10^3 Hz, 10^1–10^4 Hz, and 10^2–10^4 Hz. Sampling rates were chosen as they were for the amplifier data collection.

Figure 2.6 shows the experimental and identified shaker voltage-to-acceleration magnitude-frequency plots. The collected data is for the combined amplifier-shaker system, however the amplifier dynamics are mostly unity gain between 10^0–10^3 Hz and were ignored. The experimental magnitude-frequency plot shows zero slope for

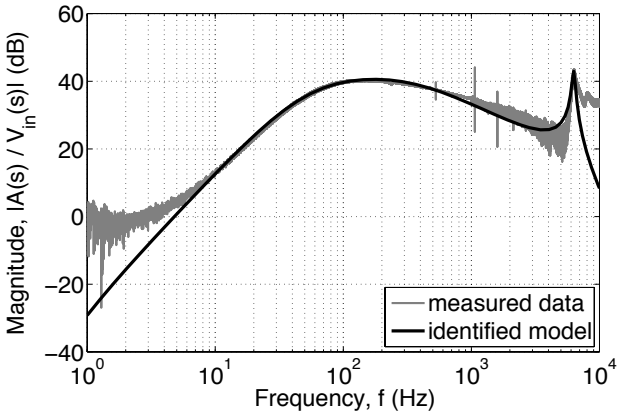

Figure 2.6: Comparison of experimental and identified shaker voltage-to-acceleration magnitude-frequency plots.

low frequencies, but that data was deemed unreliable since it was collected near the lower bound of the accelerometer bandwidth of 1–10^4 Hz [81], and because a positive forty decibel-per-decade slope is expected when measuring acceleration. Ignoring the initial zero slope portion of the plot, the experimental magnitude-frequency plot begins with a positive forty decibel-per-decade slope. Next it levels off, then drops off with a slope of negative twenty decibels per decade. Lastly, the plot has a lightly damped resonant peak, which agrees with the manufacturer's specification for the fundamental resonance of the shaker lying between $9.5\text{–}10 \times 10^4$ Hz [49]. Observations suggest a shaker transfer function of the form

$$\frac{A(s)}{V_{in}(s)} = \frac{Ks^2}{(s+2\pi f_1)^2\,(s+2\pi f_2)\left(s^2+2\zeta\,(2\pi f_3)\,s+(2\pi f_3)^2\right)}, \qquad (2.31)$$

where $K > 0$ is a constant gain, $f_1 > 0$ is the frequency at which the curve levels off, $f_2 > 0$ is the frequency at which the curve rolls over, and $f_3 > 0$ is the natural frequency of the resonant pole with damping ratio $\zeta > 0$. The parameter values, based on trial-and-error estimates, were found to be $K = 160 \times 10^{12}$, $f_1 = 54$ Hz, $f_2 = 370$ Hz, $f_3 = 6.3 \times 10^3$ Hz and $\zeta = 0.025$.

Table 2.2: Physical properties, measured dimensions, computed properties, first natural frequency and nondimensional parameters for the cantilevered beam.

Physical Properties	
E^*, Pa (psi)	70.3×10^9 (10.2×10^6)
G^*, Pa (psi)	26.2×10^9 (3.80×10^6)
ν	0.35
ρ^*, kg/m^3 (lb/in^3)	2.71×10^3 (0.098)
Measured Dimensions	
L^*, m (in)	381×10^{-3} (15.0)
h^*, m (in)	50.0×10^{-3} (1.97)
b^*, m (in)	2.24×10^{-3} (0.0880)
Computed Properties	
A^*, m^2 (in^2)	0.112×10^{-3} (0.173)
I^*, m^4 (in^4)	46.8×10^{-12} (0.112×10^{-3})
k	0.852
Natural Frequency	
ω_1^*, rad/s (Hz)	79.2 (12.6)
Nondimensional Parameters	
a	12.2
ε	$0.111 \times 10^{-}3$
μ	$0.0351 \times 10^{-}3$

2.2.3 Cantilevered Beam

Parameter Selection

The nondimensional beam parameters are $a = \frac{\rho^* \omega_1^{*2} L^{*4} A^*}{E^* I^*}$, $d = d^* \omega_1^*$, $\varepsilon = \frac{\rho^* \omega_1^{*2} L^{*2}}{k G^*}$ and $\mu = \frac{\rho^* \omega_1^{*2} L^{*2}}{E^*}$, with $A^* = b^* h^*$, $I^* = \frac{h^* b^{*3}}{12}$ and $k = \frac{10(1+\nu)}{12+11\nu}$, which require identification of the beam's material properties (Young's modulus E^*, shear modulus G^*, Poisson's ratio ν, density ρ^*), measured physical dimensions (clamped length L^*, height h^*, thickness b^*), computed physical properties (cross-sectional area A^*, moment of inertia I^*, shape factor k) and estimated physical properties (Kelvin-Voigt damping d^*, first natural frequency ω_1^*).

Table 2.2 tabulates the material properties of 6061-T6 Aluminum [58], the measured beam dimensions, the computed properties, the estimated first natural frequency (found experimentally), and the nondimensional parameters. Figure 2.7 shows a magnitude-frequency plot highlighting the first three natural frequencies of

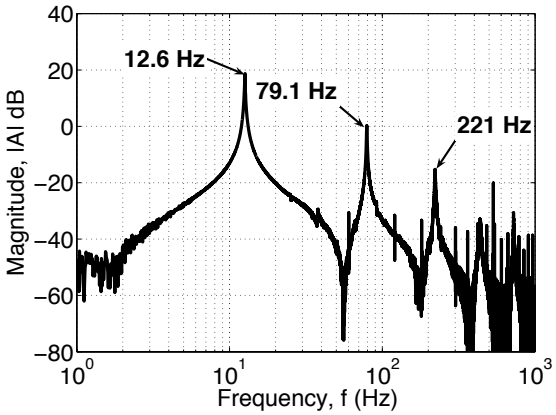

Figure 2.7: Magnitude-frequency plot of beam tip acceleration for response to initial conditions, showing first three natural frequencies of the cantilevered beam.

Table 2.3: Comparison of first three theoretical and identified natural frequencies of cantilevered beam.

	Frequency, rad/s (Hz)	
	theoretical	identified
ω_1^*	79.7 (12.7)	79.2 (12.6)
ω_2^*	499 (79.4)	497 (79.1)
ω_3^*	1400 (223)	1390 (221)

the cantilevered beam, in response to an initial displacement. Table 2.3 compares the experimentally estimated natural frequencies with the frequencies computed by the formula [32] $\omega_i^* = \sqrt{\frac{E^*I^*}{\rho^*A^*L^{*4}}}a_i^2$, where ω_i^* is the i^{th} natural frequency in radians-per-second, and a_i is the i^{th} wave number ($a_1 = 1.875$, $a_2 = 4.694$, $a_3 = 7.855$). The largest error between the experimentally estimated and theoretical computed values is less than one percent, with all the theoretical values overestimating their corresponding experimental values. Aside from confirming the estimated natural frequencies, this also shows that the beam properties summarized in Table 2.2, and used for the ω_i^* computations, are correct.

An attempt was made to find the Kelvin-Voigt (KV) damping coefficient by simulating a cantilevered beam with a, ε and μ given in Table 2.2 and adjusting the KV damping to match experimental data. The simulated data and nondimensionalized experimental data did not match, suggesting that either the parameters used to

compute a, ε and μ were incorrect, or the Timoshenko beam model did not account for extraneous effects on the beam. As another means of checking the beam properties, the beam's "spring constant" was measured and compared to the theoretical spring constant found using $f^* = \frac{3E^*I^*}{L^{*3}}x^*$ [58]. A comparison of the theoretical and experimental force-deflection curves showed that the theoretical and experimental spring constants were within one-half of a percent of each other. This again verified that the beam properties in Table 2.2 were correct.

Since the theoretical beam model required base actuation, while the testbed provided in-domain actuation, further work to identify the Kelvin-Voigt damping coefficient was suspended in favor of identification the testbed as a whole (amplifier, shaker with beam attached, and possible nonlinearities).

2.2.4 Testbed and Nonlinear Force

Experimental Identification by Trial-and-Error of the Testbed Without Nonlinearities

Input data was generated and collected by the target computer. Output data was collected with an accelerometer attached to the tip of the beam. Sine sweep ranges, and sampling rates were chosen the same as for the shaker identification experiments.

Figure 2.8 shows the experimental testbed Bode plot, showing multiple resonant peaks becoming more closely spaced as the frequency increases, along with the occasional anti-resonant peaks. The phase-frequency figure is plotted in the range $\pm 180^\circ$ ($\pm\pi$ rad) as wrapped data, i.e. when the curve reaches -180° it jumps up to 180° rather than continue into more negative values. While Figure 2.8 suggests low frequency slope and phase of zero, this is once again an issue of unreliable accelerometer data, which is further supported by a magnitude-frequency plot for the voltage-to-displacement output. Figure 2.9 compares the voltage-to-acceleration, voltage-to-displacement, and voltage-to-twice differentiated displacement (found by adding a line of slope +40 db/dec to the voltage-to-displacement data). Beam tip displacement data was measured using a laser displacement meter [34] (located at

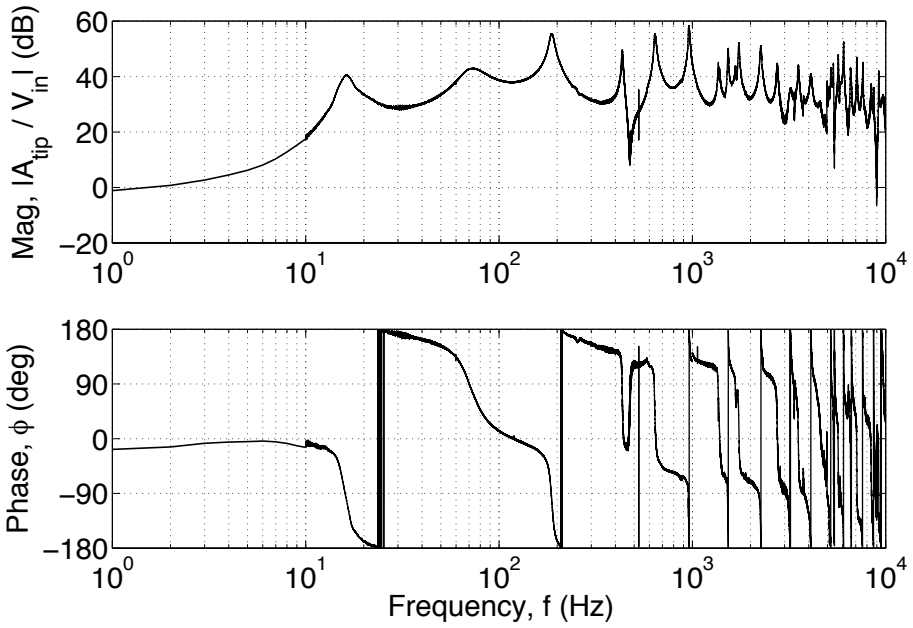

Figure 2.8: Experimental testbed voltage-to-acceleration Bode plot for an accelerometer attached to the tip of the beam.

the LANL), which provided reliable data in the low frequency range. The voltage-to-displacement curve has zero slope for low frequencies. The twice differentiated voltage-to-acceleration curve matches the trends of the experimental voltage-to-acceleration curve well, but is shifted by an arbitrary constant. This confirms that the voltage-to-acceleration curve should have a low frequency slope of positive forty decibels-per-decade.

Figure 2.10 compares the experimental and identified testbed voltage-to-acceleration magnitude-frequency plots. Based on observations of figures 2.8 and 2.9, focusing on the first three resonant modes, the voltage-to-acceleration testbed transfer function has the form

$$\begin{aligned}\frac{A_{tip}(s)}{V_{in}(s)} &= \frac{Ks^2\left(s+2\pi z_1\right)\left(s+2\pi z_2\right)}{\left(s^2+2\zeta_1\left(2\pi f_1\right)s+\left(2\pi f_1\right)^2\right)\left(s^2+2\zeta_2\left(2\pi f_2\right)s+\left(2\pi f_2\right)^2\right)} \\ &\quad\times\frac{1}{\left(s^2+2\zeta_3\left(2\pi f_3\right)s+\left(2\pi f_3\right)^2\right)}, \end{aligned} \tag{2.32}$$

where the $K > 0$ is a constant gain, the $z_i > 0$ are zeros, and the $f_i > 0$ are

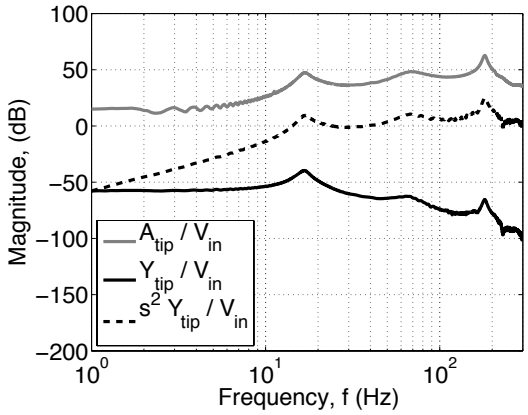

Figure 2.9: Comparison of the experimental magnitude-frequency plots from the input voltage to output acceleration and displacement, as well as a curve generated by twice differentiating (added line with +40 dB/dec slope) the voltage-to-displacement data.

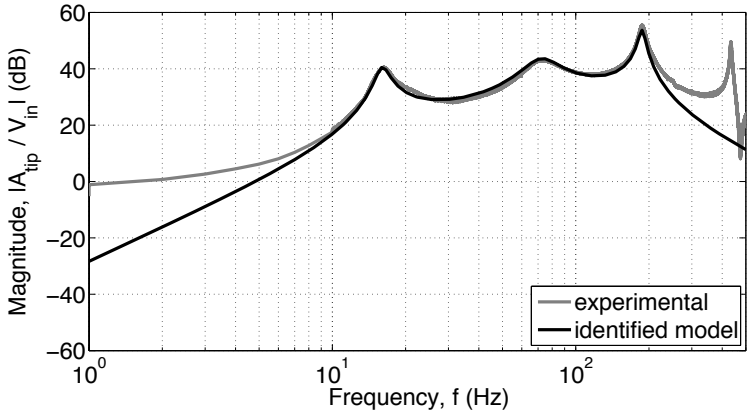

Figure 2.10: Comparison of experimental and identified testbed voltage-to-acceleration magnitude-frequency plots.

frequencies of the resonant poles with damping rations $\zeta_i > 0$. The parameter values, based on trial-and-error estimates, were found to be $K = 15 \times 10^6$, $f_1 = 16$ Hz, $f_2 = 72$ Hz, $f_3 = 188$ Hz, $z_1 = 23$ Hz, $z_2 = 102$ Hz, $\zeta_1 = 0.06$, $\zeta_2 = 0.06$, and $\zeta_3 = 0.03$.

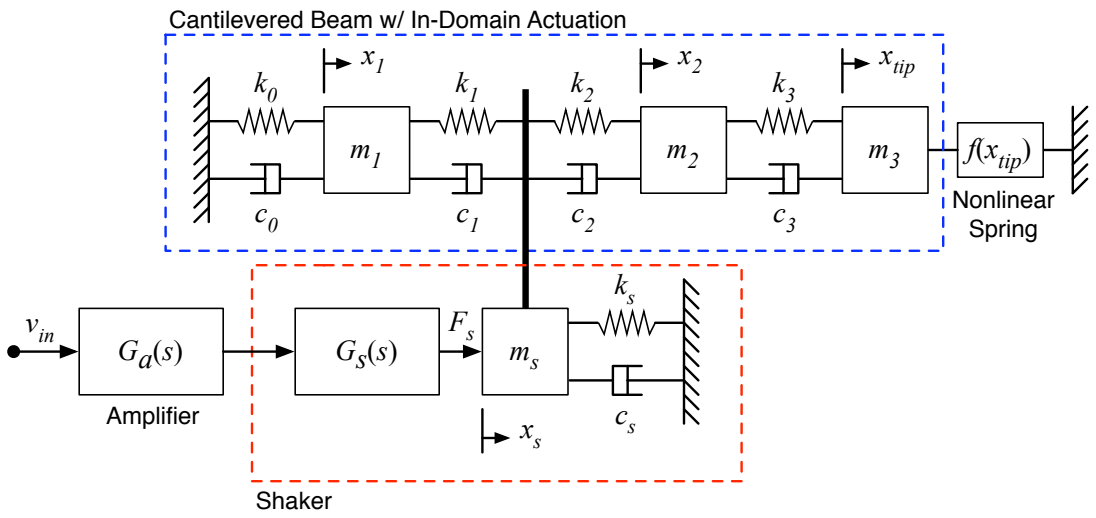

Figure 2.11: Model used for experimental identification of the testbed with nonlinearities.

Finite Dimensional Model for Testbed with Nonlinearities

Based on the resulting finite dimensional model for the testbed without nonlinearities, given in (2.32), the choice was made to find a finite dimensional model for the testbed with nonlinearities then identify its parameters experimentally. Figure 2.11 shows the model whose parameters must be identified. The cantilevered beam is modeled as three coupled spring-mass-damper systems, with a fixed base and nonlinear spring providing the nonlinear interaction force at the tip. The beam is actuated by the shaker modeled as a spring-mass-damper and transfer function.

The model to be matched to the experimental data is

$$F_s(s) = G_s(s)G_a(s)V_{in}(s) \tag{2.33}$$

$$\begin{aligned} m_s\ddot{x}_s(t) + (c_s + c_1 + c_2)\,\dot{x}_s(t) + (k_s + k_1 + k_2)\,x_s(t) &= f_s(t) + c_1\dot{x}_1(t) + k_1x_1(t) \\ &\quad + c_2\dot{x}_2(t) + k_2x_2(t) \end{aligned} \tag{2.34}$$

$$m_1\ddot{x}_1(t) + (c_0 + c_1)\,\dot{x}_1(t) + (k_0 + k_1)\,x_1(t) = c_1\dot{x}_s(t) + k_1x_s(t) \tag{2.35}$$

$$\begin{aligned} m_2\ddot{x}_2(t) + (c_2 + c_3)\,\dot{x}_2(t) + (k_2 + k_3)\,x_2(t) &= c_2\dot{x}_s(t) + k_2x_s(t) \\ &\quad + c_3\dot{x}_{tip}(t) + k_3x_{tip}(t) \end{aligned} \tag{2.36}$$

$$m_3\ddot{x}_{tip}(t) + c_3\dot{x}_{tip}(t) + k_3x_{tip}(t) \pm f\,(x_{tip}) = c_3\dot{x}_2(t) + k_3x_2(t)\,, \tag{2.37}$$

where $f_s(t)$ is the electromagnetic force of the shaker armature, $G_a(s)$ is the amplifier transfer function given in (2.30), $G_s(s)$ is a transfer function accounting for the shaker electronics and is to be identified along with the damping coefficients, $c_i > 0$, spring constants, $k_i > 0$ and masses, $m_i > 0$, and the nonlinear interaction force $f(x_{tip})$ given in (2.27). The significance of the $\pm$ sign in (2.37) is that the magnet-steel/magnet interaction can be locally softening $(-)$ or hardening $(+)$.

Experimental Identification by Trial-and-Error of the Testbed with Nonlinearities

Experimental system identification was done in three parts. First the parameters for the shaker spring-mass-damper and transfer function were identified with the beam disconnected. Second, the testbed model with $f(x_{tip}) = 0$ was used to identify parameters of the three coupled spring-mass-damper systems modeling the beam. Lastly, nonlinearities were introduced to identify the parameters of $f(x_{tip})$.

The shaker parameters c_s, k_s, and the transfer function $G_s(s)$ were experimentally identified by trial-and-error by comparison to a voltage-to-acceleration Bode plot for the shaker with hardware, but disconnected from the beam. The total mass of the shaker armature, with hardware to attach it to the beam, is $m_s = 0.039$ kg. Figure 2.12 compares the experimental Bode plot of the shaker and the identified model. The identified parameters and transfer function, based on trial-and-error estimates, were $c_s = 200$ N·s/m and $k_s = 110.5 \times 10^6$ N/m, and

$$G_s(s) = \frac{K_s f_1^{s2} f_2^s}{(s + 2\pi f_1^s)^2 (s + 2\pi f_2^s)}, \tag{2.38}$$

with $f_1^s = 54$ Hz, $f_2^s = 200$ Hz and $K_s = 2.8 \times 10^9$. The identified model matches the experimental Bode plot in the frequency range of interest, which captures the first three modes of the testbed.

Next the cantilevered beam portion of the model was identified for $f(x_{tip}) = 0$. The mass of the cantilevered beam was equally distributed to the three spring-mass-damper systems, hence $m_1 = m_2 = m_3 = 0.04$ kg. The damping and spring constants c_0, c_1, c_2, c_3, k_0, k_1, k_2, and k_3 were experimentally identified using acceleration data collected at the beam tip for the testbed without nonlinearities. Figure

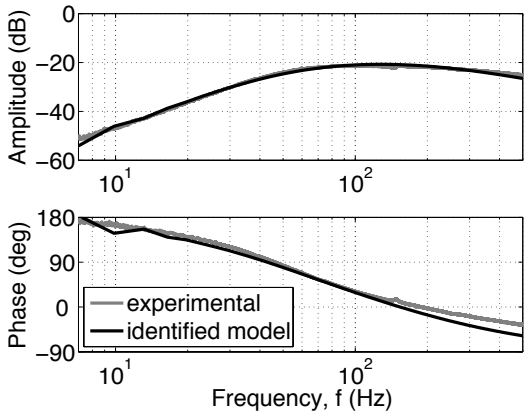

Figure 2.12: Comparison of experimental and identified voltage-to-acceleration Bode plots for shaker portion of finite dimensional testbed model for nonlinear identification.

2.13 compares the experimental and identified voltage-to-acceleration Bode plots of the linear portion of the identified nonlinear testbed. The parameter values are $c_0 = 2.2$ N·s/m, $c_1 = 1.1$ N·s/m, $c_2 = 1.1$ N·s/m, $c_3 = 2.2$ N·s/m, $k_0 = 1750$ N/m, $k_1 = 875$ N/m, $k_2 = 875$ N/m, and $k_3 = 4375$ N/m. A gain of two-and-a-half was also needed to adjust the level of the magnitude-frequency plot. The identified model does a good job matching the first mode, which is exhibits the most displacement and would therefore interact most with the nonlinear force at the tip. The discrepancy between the phase plots was caused by a poorly chosen cut-off frequency of a high-pass filter used on the experimental data. Comparisons of experimental data and the identified system were also made to evaluate the performance of the identified model when extra mass was placed at the end of the cantilevered beam. The identified model performed very well with either steel plates or magnets attached to the tip of the beam.

The parameters of the nonlinearity a_1, a_2, b_1 and b_2 depend on the geometry of the magnet locations with respect to the steel/magnets at the end of the beam. Their values, measured for the particular experimental set-up, were $a_1 = a_2 = 0.038$ m, and $b_1 = b_2 = 0.022$ m. First a locally hardening set-up was made by attaching magnets at the end of the beam to repel the magnets on the testbed. The nonlinear

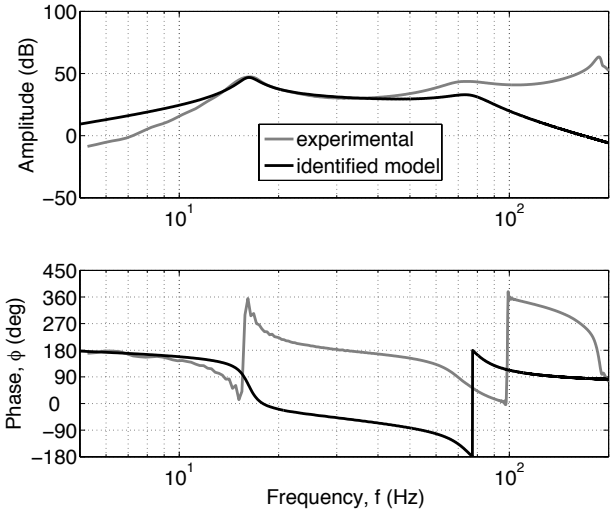

Figure 2.13: Comparison of experimental and identified voltage-to-acceleration Bode plots of finite dimensional testbed model without nonlinearities.

spring constants for the locally hardening set-up, identified by trial-and-error comparisons of experimental and simulated data, were $k_{n1} = k_{n2} = 0.2 \times 10^{-3}$ N·m^2. Comparisons of voltage-to-acceleration Bode plots showed that the model captured the nonlinear effects and matched the increase in resonant frequency of the first mode caused by the locally hardening nonlinearity.

A locally softening set-up was made by attaching steel plates at the end of the beam, which are attracted to the magnets on the testbed. The nonlinear spring constants for the locally softening set-up, identified by trial-and-error comparisons of experimental and simulated data, were $k_{n1} = k_{n2} = 0.35 \times 10^{-3}$ N·m^2. The model captured the decrease in resonant frequency of the first mode caused by the locally softening nonlinearity.

Experiments were also done to characterize the effects of the amplitude of the sine sweep input to the testbed with locally hardening and softening nonlinearities. Simulation results showed that the identified model captured those nonlinear behaviors of the testbed.

3

Motion Planning and Tracking for the Shear Beam PDE

This chapter presents explicit motion planning reference solutions for flexible beams with Kelvin-Voigt (KV) damping. The goal is to generate periodic reference signals for the displacement and deflection angle at the free-end of the beam using only actuation at the base. The explicit deflection angle reference solution is found as a result of writing the shear beam model in a strict-feedback form. PDE backstepping transformations relate the strict-feedback model to a target system, governed by an exponentially stable wave equation with KV damping, whose displacement reference solution is relatively easy to find. The explicit beam displacement reference solution is found using the target system solution and an inverse backstepping transformation. The explicit reference solutions for the wave equation and shear beam with KV damping are novel results. State-feedback tracking boundary controllers are found by extending previous PDE backstepping stabilization results. Application of the shear beam results to the more complicated Timoshenko beam is discussed.

3.1 Introduction

Great strides have been made in the design and implementation of collocated boundary controllers—a control architecture with sensing and actuation implemented at the same boundary point—for flexible beams for vibration suppression and stabilization. A comprehensive monograph on collocated boundary control of flexible beams [52] presents the key approaches for studying stability and for imparting damping via boundary control. Work done in [10, 11, 20, 21, 90] has achieved analytical and experimental success in designing collocated boundary controllers for flexible beams. Recent work has also been done to extend vibration suppression and stabilizing controllers to non-collocated systems [71, 75, 76, 88]—systems with actuation and sensing at different points. This work pursues the line of non-collocated boundary control, going beyond the problem of equilibrium stabilization to solve the problems of motion planning and reference tracking for flexible beams. Motion planning (trajectory generation) is the problem of finding the appropriate boundary input to produce a desired output. The full-state motion planning reference solution can be used to find an open-loop boundary input, or combined with tracking boundary controllers to improve the rate of convergence to the reference solution.

Motion planning results for strings and flexible structures without Kelvin-Voigt (KV) damping—internal/material damping—have been presented in [1, 27, 55, 56, 60, 62]. This work considers systems with KV damping since they are more physically relevant, and note that the damping terms make finding the reference solution more difficult (though they make the stabilization problem slightly easier). The system models being considered are the wave equation (string and target system) and the shear and Timoshenko beams. A string is a single-input-single-output system, with the displacement at the base as the input, and the same quantity at the free-end as the output. A beam is a two-input-two-output system with the displacement and deflection angle at the base as the inputs, and the same quantities at the free-end as outputs. Figure 3.1 shows a diagram representing the problem set-up. Motivation for this set-up comes from a particular shake table control problem where the table provides boundary actuation to a structure, modeled here as a flexible beam, in order to impart a desired reference trajectory at its free-end. This set-up also

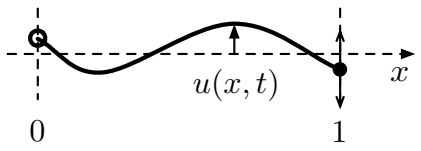

Figure 3.1: Diagram depicting a string/beam with transverse displacement $u(x,t)$. The goal is to generate and track a reference trajectory at $x = 0$. The arrows at $x = 1$ represent actuation, and the circle at $x = 0$ represents the desired reference trajectory.

applies directly to the control of dynamic mode atomic force microscopy (AFM), where a cantilevered beam is actuated at the base to produce a sinusoidal output at the free-end.

The shear beam design begins by writing the model in a strict-feedback (spatially causal) form to which PDE backstepping techniques can be applied [39, 40, 43, 44]. The deflection angle boundary controller is found as a result of this step, and a clever modification of that controller produces the explicit deflection angle reference solution. PDE backstepping transformations—state transformations that relate one PDE and boundary condition(s) to another—are used to relate the strict-feedback shear beam model to the target system—a reference model used in control design, governed by a wave equation with KV damping. The inverse state transformation is used to find the explicit beam displacement reference solution given the target system reference solution. The target system reference solution is found using the direct transformation between the target and string states and the explicit string reference solution. The explicit motion planning reference solution for the string model is found by postulating the reference solution as a power series of the spatial variable with time dependent coefficients [1, 24, 27, 28, 50, 55, 56, 60, 62]. The advantage of employing PDE backstepping techniques is that they provide a means for the rather complicated shear beam reference solution to be found using the relatively simple reference solution for the string.

The motion planning results in the presence of Kelvin-Voigt damping for the string, target system, and especially for the shear beam models are novel and non-trivial results. The KV damping introduces a new complexity in propagating the

control signal from one boundary to the other boundary, and the shear beam requires a two-stage construction of the motion-planning solution, which does not arise with simple wave equations and Euler-Bernoulli beams. Furthermore, explicit motion planning results are novel.

Aside from facilitating the motion planning designs, the PDE backstepping approach is also used to combine the open-loop reference solutions with state-feedback boundary controllers to achieve exponential convergence to the reference trajectories. These results are extensions of the stabilizing boundary controller designs for the string model, and the shear and Timoshenko beams [39, 40, 41, 42, 43, 44].

This Chapter is organized as follows. Section 3.2 presents the system models. Section 3.3 presents the reference solutions for the string, target system, and shear beam. Section 3.4 presents stabilizing tracking boundary controllers for the string and the shear beam. Section 3.5 presents simulation results for the generation and tracking of sinusoids for the string and the Timoshenko beam.

3.2 System Models

3.2.1 String

The string model is given by the wave equation

$$\varepsilon u_{tt}(x,t) = (1 + d\partial_t)\, u_{xx}(x,t) \tag{3.1}$$

$$u_x(0,t) = 0\,, \tag{3.2}$$

where $u(x,t)$ is the displacement of the string along $0 \leq x \leq 1$ at time $0 \leq t < \infty$, with initial conditions $u_0(x) = u(x,0)$ and $\dot{u}_0(x) = u_t(x,0)$, d is the Kelvin-Voigt (KV) damping coefficient, and ε is the inverse of the nondimensional string stiffness. Partial derivatives with respect to space and time are denoted by sub-scripts x and t respectively. The boundary condition (3.2) at $x = 0$ represents a free-end. The boundary input $u_x(1,t)$ is used as a control input.

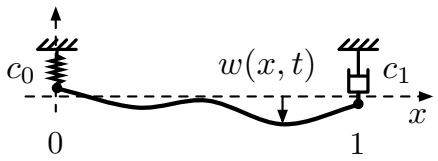

Figure 3.2: Diagram representing the target system.

3.2.2 Target System

The target system is an exponentially stable reference model used in PDE backstepping control design. It is not necessarily unique or optimal, but is chosen to have desirable performance characteristics and work well within the framework of PDE backstepping theory. The target system model used for string, shear beam and Timoshenko beam designs [39, 40, 41, 42, 43, 44], shown in Fig. 3.2 as a string with a spring at $x = 0$ and a damper at $x = 1$, is given by the wave equation

$$\begin{aligned} \varepsilon w_{tt}(x,t) &= (1 + d\partial_t)\, w_{xx}(x,t) && (3.3)\\ w_x(0,t) &= c_0 w(0,t) && (3.4)\\ w_x(1,t) &= -c_1 w_t(1,t)\,, && (3.5) \end{aligned}$$

where $w(x,t)$ is the displacement of the target system, and has initial conditions $w_0(x) = w(x,0)$ and $\dot{w}_0(x) = w_t(x,0)$. The parameters $c_0 > 0$ and $c_1 > 0$ are design gains representing the spring stiffness and damping coefficient of the spring and damper located at opposite ends of the string. The spring stiffness c_0 should be large to emulate a pinned boundary condition at $x = 0$, and the damping coefficient c_1 should be chosen near $\sqrt{\varepsilon}$ to emulate a tuned damper at the end $x = 1$.

3.2.3 Flexible Beams

The Timoshenko beam model is written as the two coupled wave equations (2.21), (2.22) with the free-end boundary conditions (2.23), (2.24), with actuation at the base $x = 1$ through the boundary inputs $u_x(1,t)$ and $\alpha(1,t)$. The states $u(x,t)$ and $\alpha(x,t)$ denote the displacement and deflection angle, with initial conditions $u_0(x) = u(x,0)$, $\dot{u}_0(x) = u_t(x,0)$, $\alpha_0(x) = \alpha(x,0)$ and $\dot{\alpha}_0(x) = \alpha_t(x,0)$ respectively.

The shear beam model can be written as a singular perturbation ($\mu = 0$) of the Timoshenko beam model, and is given by the wave equation (2.21) coupled with the second-order-in-space ordinary differential equation

$$0 \;=\; \varepsilon\alpha_{xx}(x,t) + a\left(u_x(x,t) - \alpha(x,t)\right) . \tag{3.6}$$

This model also has free end boundary conditions (2.23), (2.24), and boundary inputs $u_x(1,t)$, $\alpha(1,t)$.

The shear and Timoshenko beam models are considered for this work since they are the more physically relevant and complete beam models. The Timoshenko beam model is the most accurate of the four, accounting for transverse displacement, bending moment, shear distortion and rotary inertia [32].

3.3 Motion Planning

Motion planning for the displacement (string, target system, shear beam) and deflection angle (shear beam) is done for sinusoidal reference trajectories since they are relevant functions in the fields of shake table control and dynamic mode atomic force microscopy, where reference trajectories tend to be oscillatory, and since they can form a basis for more complicated functions.

3.3.1 String

The solution to the motion planning problem for the string model (3.1), (3.2), is found for the sinusoidal tip displacement reference trajectory

$$u^r(0,t) = A_u \sin\left(\omega_u t\right) \tag{3.7}$$

by postulating the reference solution $u^r(x,t)$ as a power series of the spatial variable with time dependent coefficients, i.e., $u^r(x,t) = \sum_{i=0}^{\infty} a_i(t)\frac{x^i}{i!}$. Applications of this approach can be found in [1, 28, 50, 62]. The string reference solution is

$$u^r(x,t) \;=\; -\frac{jA_u}{2}\left[\cosh\left(j\sigma x\right)\mathrm{e}^{j\omega_u t} - \cosh\left(j\bar{\sigma}x\right)\mathrm{e}^{-j\omega_u t}\right], \tag{3.8}$$

with the complex valued constant $\sigma = \frac{\omega_u\sqrt{\varepsilon}}{\sqrt{1+j\omega_u d}}$. Equation (3.8) can be written as the purely real function

$$u^r(x,t) = \frac{A_u}{2}\left[e^{\hat{\beta}(\omega_u)x}\sin\left(\omega_u t+\beta(\omega_u)x\right)+e^{-\hat{\beta}(\omega_u)x}\sin\left(\omega_u t-\beta(\omega_u)x\right)\right], \quad (3.9)$$

where the real functions $\beta(n)$ and $\hat{\beta}(n)$ are defined as

$$\beta(n) = n\sqrt{\varepsilon}\sqrt{\frac{\sqrt{1+n^2d^2}+1}{2\left(1+n^2d^2\right)}} \quad (3.10)$$

$$\hat{\beta}(n) = n\sqrt{\varepsilon}\sqrt{\frac{\sqrt{1+n^2d^2}-1}{2\left(1+n^2d^2\right)}}. \quad (3.11)$$

The open-loop displacement (Dirichlet) control $u^r(1,t)$ is found by evaluating (3.9) at $x = 1$. The expression for the open-loop slope/force (Neumann) control input $u^r_x(1,t)$, found by evaluating the partial derivative with-respect-to-x of (3.9) at $x = 1$, is

$$\begin{aligned} u^r_x(1,t) = \frac{A_u}{2}\Big[&\hat{\beta}(\omega_u)e^{\hat{\beta}(\omega_u)}\sin\left(\omega_u t+\beta(\omega_u)\right)+\beta(\omega_u)e^{\hat{\beta}(\omega_u)}\cos\left(\omega_u t+\beta(\omega_u)\right) \\ &-\hat{\beta}(\omega_u)e^{-\hat{\beta}(\omega_u)}\sin\left(\omega_u t-\beta(\omega_u)\right)-\beta(\omega_u)e^{-\hat{\beta}(\omega_u)}\cos\left(\omega_u t-\beta(\omega_u)\right)\Big]. \end{aligned} \quad (3.12)$$

Theorem 3.1 *The string model* (3.1), (3.2) *is satisfied by the state reference trajectory* (3.9). *The output of the system satisfies the tip displacement reference trajectory* (3.7) *given the open-loop Neumann control input* (3.12), *assuming* $u_0(x) = u^r(x,0)$ *and* $\dot{u}_0(x) = u^r_t(x,0)$.

Proof: The reference solution (3.9) evaluated at $x = 0$ satisfies the desired reference trajectory (3.7). Equation (3.9) substituted into (3.1) and (3.2) satisfies the string PDE and free-end boundary condition. ■

3.3.2 Target System

The solution to the motion planning problem for the target system model (3.3), (3.4) is found using the reference solution for the string model and a PDE backstepping state transformation. The string model (3.1), (3.2) with boundary actuation

$u_x(1,t)$, and the target system (3.3)–(3.5) are related via the direct backstepping transformation $w(x,t) = u(x,t) + c_0 \int_0^x u(y,t)\,dy$ [41, 42], which when substituted into (3.3), (3.4) satisfies (3.1), (3.2). Therefore, the target system reference solution $w^r(x,t)$, found as a function of the string reference solution $u^r(x,t)$, is given by

$$w^r(x,t) \;=\; u^r(x,t) + c_0 \int_0^x u^r(x,t)\,dy\,. \tag{3.13}$$

Backstepping transformations preserve values at the boundary $x = 0$, i.e. $w(0,t) = u(0,t)$, and so the target system tip displacement reference trajectory

$$w^r(0,t) \;=\; A_u \sin(\omega_u t) \tag{3.14}$$

is equivalent to the string reference trajectory $u^r(0,t)$. The reference solution, found by substituting (3.8) into (3.13) and evaluating the integral, is

$$\begin{aligned} w^r(x,t) \;=\; & -\frac{jA_u}{2}\left[\cosh(j\sigma x)\,\mathrm{e}^{j\omega_u t} - \cosh(j\bar{\sigma}x)\,\mathrm{e}^{-j\omega_u t}\right] \\ & -\frac{c_0 A_u}{2}\left[\frac{1}{\sigma}\sinh(j\sigma x)\mathrm{e}^{j\omega_u t} - \frac{1}{\bar{\sigma}}\sinh(j\bar{\sigma}x)\,\mathrm{e}^{-j\omega_u t}\right], \end{aligned} \tag{3.15}$$

with the complex valued constant $\sigma = \frac{\omega_u\sqrt{\varepsilon}}{\sqrt{1+j\omega_u d}}$. The expression for $w^r(x,t)$ can be written as the purely real function

$$\begin{aligned} w^r(x,t) \;=\; & \frac{A_u}{2}\left[\mathrm{e}^{\hat{\beta}(\omega_u)x}\sin(\omega_u t + \beta(\omega_u)x) + \mathrm{e}^{-\hat{\beta}(\omega_u)x}\sin(\omega_u t - \beta(\omega_u)x)\right] \\ & -\frac{c_0 A_u}{2} \\ & \times\Big\{\gamma(\omega_u)\left[\mathrm{e}^{\hat{\beta}(\omega_u)x}\cos(\omega_u t + \beta(\omega_u)x) - \mathrm{e}^{-\hat{\beta}(\omega_u)x}\cos(\omega_u t - \beta(\omega_u)x)\right] \\ & -\hat{\gamma}(\omega_u)\left[\mathrm{e}^{\hat{\beta}(\omega_u)x}\sin(\omega_u t + \beta(\omega_u)x) - \mathrm{e}^{-\hat{\beta}(\omega_u)x}\sin(\omega_u t - \beta(\omega_u)x)\right]\Big\}\,, \end{aligned} \tag{3.16}$$

where the real valued functions $\beta(n)$, and $\hat{\beta}(n)$ are defined in (3.10), (3.11) respectively, and $\gamma(n)$, and $\hat{\gamma}(n)$ are defined as

$$\gamma(n) \;=\; \frac{1}{n\sqrt{\varepsilon}}\sqrt{\frac{\sqrt{1+n^2d^2}+1}{2}} \tag{3.17}$$

$$\hat{\gamma}(n) \;=\; \frac{1}{n\sqrt{\varepsilon}}\sqrt{\frac{\sqrt{1+n^2d^2}-1}{2}}\,. \tag{3.18}$$

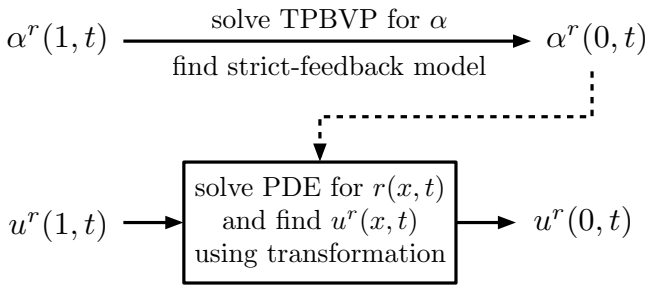

Figure 3.3: Pictorial representation of the structure of the input-output relationship $\{u^r(1,t), \alpha^r(1,t)\} \mapsto \{u^r(0,t), \alpha^r(0,t)\}$, and a description of the types of problems involved in solving the simultaneous motion planning problem for the shear beam.

The open-loop displacement (Dirichlet) control $w^r(1,t)$ is found by evaluating (3.16) at $x = 1$. The open-loop slope/force (Neumann) control $w^r_x(1,t)$ is found by evaluating the partial derivative with-respect-to-x of (3.16) at $x = 1$.

Theorem 3.2 *The target system* (3.3), (3.4) *is satisfied by the state reference trajectory* (3.16). *The output of the system satisfies the tip displacement reference trajectory* (3.14) *given the open-loop Neumann control input* $w^r_x(1,t)$, *assuming* $w_0(x) = w^r(x,0)$ *and* $\dot{w}_0(x) = w^r_t(x,0)$.

Proof: The reference solution (3.16) evaluated at $x = 0$ satisfies the reference trajectory (3.14). Equation (3.16) substituted into (3.3) and (3.4) satisfies the target system PDE and $x = 0$ boundary condition. ■

3.3.3 Shear Beam

Figure 3.3 shows a pictorial representation of the two-part structure of the simultaneous motion planning problem for the shear beam. Finding $\alpha^r(1,t)$ involves solving a two point boundary value problem (TPBVP) for $\alpha(x,t)$, then modifying the resulting boundary input $\alpha(1,t)$ to satisfy both spatial causality of the shear beam and motion planning. Finding $u^r(1,t)$ requires solving a PDE for an auxiliary system $r(x,t)$, then employing a direct transformation from $w^r(x,t)$ to $u^r(x,t)$.

A backstepping transformation is ultimately used to find the state reference trajectory, therefore the first part requires writing the shear beam model (2.21), (3.6),

$$u(x,t) \underset{-c_0 e^{-c_0(x-y)}}{\overset{-c_0}{\rightleftarrows}} w(x,t) \underset{k(x,y)}{\overset{l(x,y)}{\rightleftarrows}} u(x,t)$$

string target strict-feedback shear beam

Figure 3.4: The string of invertible transformations involved in solving the shear beam motion planning problem. The functions above and below the arrows represent the appropriate transformation gains.

(2.23), (2.24) in a strict-feedback (spatially causal) form that makes PDE backstepping tools applicable. The second part requires solving the simultaneous motion planning problem by first finding the reference solution for the free-end deflection angle $\alpha(0,t)$, and then using a backstepping transformation to find the reference solution for the free-end displacement $u(0,t)$. Figure 3.4 shows the transformations relating the string, target system, and strict-feedback shear beam used to relate the string displacement reference solution (easiest to find) to the strict-feedback shear beam solution.

Strict-Feedback Shear Beam Model

The ordinary differential equation (ODE) in (3.6), with the boundary condition (2.24) and $\alpha(1,t)$ available as the control input, constitutes a two-point-boundary-value problem. The general solution of that problem is [39, 40, 43, 44]

$$\begin{aligned} \alpha(x,t) &= \cosh(bx)\alpha(0,t) + b\sinh(bx)u(0,t) \\ &\quad -b^2\int_0^x \cosh\left(b(x-y)\right)u(y,t)\,dy\,, \end{aligned} \tag{3.19}$$

with $b = \sqrt{\frac{a}{\varepsilon}}$, which can be evaluated at $x = 1$ and written as

$$\begin{aligned} \alpha(0,t) &= \frac{1}{\cosh(b)}\left(\alpha(1,t) - b\sinh(b)u(0,t)\right. \\ &\quad \left. +b^2\int_0^1 \cosh\left(b(1-y)\right)u(y,t)\,dy\right)\,. \end{aligned} \tag{3.20}$$

Substituting the partial derivative with-respect-to-x of (3.19) into (2.21), and (3.20) into (2.23), produces

$$\varepsilon u_{tt}(x,t) = (1+d\partial_t)\Big[u_{xx}(x,t) + b^2 u(x,t) - b^2\cosh(bx)\,u(0,t)$$

$$
\begin{aligned}
& +b^3 \int_0^x \sinh\left(b\left(x-y\right)\right) u(y,t)\, dy \\
& -\frac{b\sinh(bx)}{\cosh(b)} \left\{\alpha(1,t) - b\sinh(b) u(0,t) \right. \\
& \left. +b\int_0^1 \sinh\left(b(1-y)\right) u(y,t)\, dy \right\} \Big] \qquad (3.21) \\
u_x(0,t) \;=\; & \frac{1}{\cosh(b)} \left\{\alpha(1,t) - b\sinh(b) u(0,t) \right. \\
& \left. +b\int_0^1 \sinh\left(b(1-y)\right) u(y,t)\, dy \right\} . \qquad (3.22)
\end{aligned}
$$

Backstepping tools require that the plant model be in a strict-feedback form, therefore (3.21) and (3.22) cannot contain terms that violate spatial causality, i.e., integrals over the entire spatial domain $\left(\int_0^1 \cdot\, dy\right)$. Therefore, the boundary control $\alpha(1,t)$ is chosen as

$$
\alpha(1,t) \;=\; b\sinh(b) u(0,t) - b\int_0^1 \sinh\left(b(1-y)\right) u(y,t)\, dy\,, \qquad (3.23)
$$

which simplifies (3.21), (3.22) into the strict-feedback model [39, 40, 43, 44]

$$
\begin{aligned}
\varepsilon u_{tt}(x,t) \;=\; & (1+d\partial_t) \left\{ u_{xx}(x,t) + b^2 u(x,t) - b^2 \cosh\left(bx\right) u(0,t) \right. \\
& \left. +b^3 \int_0^x \sinh\left(b\left(x-y\right)\right) u(y,t)\, dy \right\} \qquad (3.24) \\
u_x(0,t) \;=\; & 0 \qquad (3.25)
\end{aligned}
$$

to which backstepping tools can now be applied.

The strict-feedback shear beam model (3.24), (3.25) with boundary actuation $u_x(1,t)$, and the target system (3.3)–(3.5) are related by the direct backstepping transformation

$$
w(x,t) = u(x,t) - \int_0^x k(x,y) u(y,t)\, dy\,, \qquad (3.26)
$$

with $k(x,y)$ satisfying the partial-integro differential equation (PIDE) [39, 40, 43, 44]

$$
\begin{aligned}
k_{xx}(x,y) \;=\; & k_{yy}(x,y) + b^2 k(x,y) - b^3 \sinh\left(b(x-y)\right) \\
& +b^3 \int_y^x k(x,\xi) \sinh\left(b(\xi-y)\right)\, d\xi \qquad (3.27) \\
k(x,x) \;=\; & -\frac{b^2}{2} x - c_0 \qquad (3.28) \\
k_y(x,0) \;=\; & -b^2 \cosh(bx) + b^2 \int_0^x k(x,y) \cosh(by)\, dy \qquad (3.29)
\end{aligned}
$$

on the domain $0 \leq y \leq x \leq 1$, which when substituted into (3.3), (3.4) satisfies (3.24), (3.25). The two systems are also related through the inverse backstepping transformation

$$u(x,t) = w(x,t) + \int_0^x l(x,y)w(y,t)\,dy\,, \tag{3.30}$$

where $l(x,y)$ satisfies the PIDE

$$\begin{aligned} l_{xx}(x,y) &= l_{yy}(x,y) - b^2 l(x,y) - b^3 \sinh\left(b(x-y)\right) \\ &\quad -b^3 \int_y^x \sinh\left(b(x-\xi)\right) l(\xi,y)\,d\xi \end{aligned} \tag{3.31}$$

$$l(x,x) = -\frac{b^2}{2}x - c_0 \tag{3.32}$$

$$l_y(x,0) = c_0 l(x,0) - b^2 \cosh(bx) \tag{3.33}$$

on the domain $0 \leq y \leq x \leq 1$.

Lemma 3.1 *The inverse backstepping transformation* (3.30)*, with* $l(x,y)$ *satisfying* (3.31)–(3.33)*, substituted into* (3.24)*,* (3.25) *satisfies* (3.3)*,* (3.4)*.*

Proof: Substituting (3.30) and its appropriate partial derivatives into (3.24), (3.25), and using the relationships in (3.3), (3.4), shows that $l(x,y)$ must satisfy (3.31)–(3.33) in order to satisfy the transformation from target to plant states. ■

Simultaneous Motion Planning

The boundary control signal (3.23) satisfies the need for the shear beam model to be spatially causal, but it also forces $\alpha(0,t) = 0$ in (3.20) and eliminates the opportunity to do motion planning for the tip deflection angle. However, for a given reference signal $\alpha^r(0,t)$, augmenting the boundary control law (3.23) with the additive term $\cosh(b)\alpha^r(0,t)$ produces the boundary condition $\alpha(0,t) = \alpha^r(0,t)$ and satisfies the desired tip deflection angle reference trajectory. The strict-feedback shear beam model for motion planning is then

$$\begin{aligned} \varepsilon u_{tt}(x,t) &= (1 + d\partial_t)\Big\{u_{xx}(x,t) + b^2 u(x,t) - b^2 \cosh\left(bx\right) u(0,t) \\ &\quad +b^3 \int_0^x \sinh\left(b\left(x-y\right)\right) u(y,t)\,dy - b\sinh\left(bx\right)\alpha^r(0,t)\Big\} \end{aligned} \tag{3.34}$$

$$u_x(0,t) = \alpha^r(0,t)\,. \tag{3.35}$$

The explicit deflection angle reference solution is given by

$$\begin{aligned}\alpha^r(x,t) &= \cosh(bx)\alpha^r(0,t) + b\sinh(bx)u^r(0,t) \\ &\quad -b^2\int_0^x \cosh\left(b(x-y)\right)u^r(y,t)\,dy\,, \end{aligned} \tag{3.36}$$

and the boundary control for motion planning is

$$\begin{aligned}\alpha^r(1,t) &= \cosh(b)\alpha^r(0,t) + b\sinh(b)u^r(0,t) \\ &\quad -b^2\int_0^1 \cosh\left(b(1-y)\right)u^r(y,t)\,dy\,, \end{aligned} \tag{3.37}$$

where $u^r(x,t)$ is the state reference trajectory for the strict-feedback shear beam model (3.34), (3.35), and can be found using a PDE backstepping transformation from the target system to the strict-feedback shear beam model.

The strict-feedback shear beam model for motion planning (3.34), (3.35) with boundary actuation $u_x(1,t)$, and the target system (3.3)–(3.5) are related through the direct backstepping transformation

$$w(x,t) = u(x,t) - \int_0^x k(x,y)u(y,t)\,dy + r(x,t) \tag{3.38}$$

where $k(x,y)$ satisfies (3.27)–(3.29), and $r(x,t)$ is the state of an auxiliary system satisfying the PDE

$$\begin{aligned}\varepsilon r_{tt}(x,t) &= (1+d\partial_t)\left\{r_{xx}(x,t)\right. \\ &\quad \left. + \left(-b\sinh(bx) + b\int_0^x k(x,y)\sinh(by)\,dy\right)\alpha^r(0,t)\right\} \qquad (3.39) \\ r(0,t) &= 0 \qquad (3.40) \\ r_x(0,t) &= \alpha^r(0,t)\,. \qquad (3.41)\end{aligned}$$

The auxiliary state $r(x,t)$ is required in order to satisfy the transformation from target to plant when the reference solution for the tip deflection angle is introduced into the design. The two systems are also related through the inverse backstepping transformation

$$u(x,t) = w(x,t) - r(x,t) + \int_0^x l(x,y)\left[w(y,t) - r(y,t)\right]\,dy\,, \tag{3.42}$$

where $l(x,y)$ and $r(x,t)$ satisy (3.31)–(3.33) and (3.39)–(3.41).

Lemma 3.2 *The direct backstepping transformation* (3.38)*, with* $k(x,y)$ *satisfying* (3.27)–(3.29) *and* $r(x,t)$ *satisfying* (3.39)–(3.41)*, substituted into* (3.3)*,* (3.4) *satisfies* (3.34)*,* (3.35)*.*

Proof: Substituting (3.38) and its partial derivatives into (3.3), (3.4), using the relationships in (3.34), (3.35), shows that $k(x,y)$ and $r(x,t)$ must satisfy (3.27)–(3.29) and (3.39)–(3.41). ■

Lemma 3.3 *The inverse backstepping transformation* (3.42)*, with* $l(x,y)$ *satisfying* (3.31)–(3.33) *and* $r(x,t)$ *satisfying* (3.39)–(3.41)*, substituted into* (3.34)*,* (3.35) *satisfies* (3.3)*,* (3.4)*.*

Proof: Substituting (3.42) and its appropriate partial derivatives into (3.34), (3.35), and using the relationships in (3.3), (3.4), shows that $l(x,y)$ and $r(x,t)$ must satisfy (3.31)–(3.33) and (3.39)–(3.41) respectively. ■

The explicit displacement reference solution for the strict-feedback shear beam model for motion planning, found using the inverse transformation (3.42), is

$$u^r(x,t) = w^r(x,t) - r(x,t) + \int_0^x l(x,y)\left[w^r(y,t) - r(y,t)\right] dy\,, \tag{3.43}$$

where $w^r(x,t)$ is given in (3.16), and $r(x,t)$ must be found for a particular tip deflection angle reference trajectory $\alpha^r(0,t)$. The shear beam tip displacement reference trajectory, found by evaluating (3.43) at $x=0$, is given by (3.7).

The open-loop displacement (Dirichlet) boundary control is found by evaluating (3.43) at $x=1$. The open-loop slope/force (Neumann) boundary control, found by evaluating the partial derivative with-respect-to-x of (3.43) at $x=1$, is

$$\begin{aligned} u_x^r(1,t) &= w_x^r(1,t) - r_x(1,t) + l(1,1)\left[w^r(1,t) - r(1,t)\right] \\ &\quad + \int_0^1 l_x(1,y)\left[w^r(y,t) - r(y,t)\right] dy\,, \end{aligned} \tag{3.44}$$

where $w^r(1,t)$ is given by (3.16) evaluated at $x=1$, and $w_x^r(1,t)$ is given by the partial derivative with-respect-to-x of (3.16) evaluated at $x=1$. The expressions $r(1,t)$ and $r_x(1,t)$ can be derived from the solution for $r(x,t)$.

To that end consider the sinusoidal tip deflection angle reference trajectory

$$\alpha^r(0,t) = A_\alpha \sin\left(\omega_\alpha t\right)\,, \tag{3.45}$$

where A_α and ω_α are the amplitude and frequency respectively. The solution to the auxiliary system $r(x,t)$ is found by first taking a Laplace transform in space of (3.39)–(3.41), which reduces the PDE in space and time to the ODE in time

$$\varepsilon\ddot{R}(s,t) - ds^2\dot{R}(s,t) - s^2R(s,t) \;=\; (\Phi(s)-1)(\alpha^r(0,t) + d\dot{\alpha}^r(0,t))\,, \quad (3.46)$$

where $\Phi(s)$ denotes the Laplace transform of

$$\phi(x) \;=\; -b\sinh(bx) + b\int_0^x k(x,y)\sinh(by)\,dy\,. \quad (3.47)$$

The solution to (3.46), ignoring transients, is assumed to be of the form

$$R(s,t) \;=\; A_1(s)\sin(\omega_\alpha t) + A_2(s)\cos(\omega_\alpha t)\;, \quad (3.48)$$

where $A_1(s)$ and $A_2(s)$ must by found.

Substituting (3.45) and (3.48) into (3.46), grouping terms common in $\sin(\omega_\alpha t)$ and $\cos(\omega_\alpha t)$, then solving the resulting linear algebra problem for $A_1(s)$ and $A_2(s)$ gives $A_1(s) = A_\alpha F_1(s)\,(1-\Phi(s))$ and $A_2(s) = A_\alpha F_2(s)\,(1-\Phi(s))$, where $F_1(s) = \frac{\left(1+\omega_\alpha^2 d^2\right)s^2+\varepsilon\omega_\alpha^2}{(1+\omega_\alpha^2 d^2)s^4+2\varepsilon\omega_\alpha^2 s^2+(\varepsilon\omega_\alpha^2)^2}$ and $F_2(s) = \frac{\varepsilon\omega_\alpha^3 d}{(1+\omega_\alpha^2 d^2)s^4+2\varepsilon\omega_\alpha^2 s^2+(\varepsilon\omega_\alpha^2)^2}$. The inverse Laplace transforms of $A_1(s)$, $A_2(s)$, $F_1(s)$, and $F_2(s)$ are

$$a_1(x) \;=\; A_\alpha\left(f_1(x) - \int_0^x f_1(x-y)\phi(y)\,dy\right) \quad (3.49)$$

$$a_2(x) \;=\; A_\alpha\left(f_2(x) - \int_0^x f_2(x-y)\phi(y)\,dy\right) \quad (3.50)$$

$$f_1(x) \;=\; \frac{1}{2}\left(\frac{1}{\nu}\sin(\nu x) + \frac{1}{\bar{\nu}}\sin(\bar{\nu}x)\right) \quad (3.51)$$

$$f_2(x) \;=\; \frac{j}{2}\left(\frac{1}{\nu}\sin(\nu x) - \frac{1}{\bar{\nu}}\sin(\bar{\nu}x)\right)\,, \quad (3.52)$$

with the complex valued constant $\nu = \omega_\alpha\sqrt{\varepsilon}\sqrt{\frac{1+j\omega_\alpha d}{1+\omega_\alpha^2 d^2}}$. The expressions in (3.51) and (3.52) can be written as the purely real functions

$$\begin{aligned} f_1(x) \;=\;& \gamma(\omega_\alpha)\sin(\beta(\omega_\alpha)x)\cosh(\hat{\beta}(\omega_\alpha)x) \\ &+\hat{\gamma}(\omega_\alpha)\cos(\beta(\omega_\alpha)x)\sinh(\hat{\beta}(\omega_\alpha)x) \end{aligned} \quad (3.53)$$

$$\begin{aligned} f_2(x) \;=\;& -\gamma(\omega_\alpha)\cos(\beta(\omega_\alpha)x)\sinh(\hat{\beta}(\omega_\alpha)x) \\ &+\hat{\gamma}(\omega_\alpha)\sin(\beta(\omega_\alpha)x)\cosh(\hat{\beta}(\omega_\alpha)x)\,, \end{aligned} \quad (3.54)$$

where the real valued functions $\beta(n)$, $\hat{\beta}(n)$, $\gamma(n)$ and $\hat{\gamma}(n)$ are defined in (3.10), (3.11), (3.17) and (3.18) respectively.

The solution to the auxiliary system, given by the inverse Laplace transform of (3.48) with $a_1(x)$ and $a_2(x)$ given in (3.49), (3.50), is then

$$\begin{aligned} r(x,t) &= A_\alpha \left(f_1(x) - \int_0^x f_1(x-y)\phi(y)\,dy \right) \sin(\omega_\alpha t) \\ &\quad + A_\alpha \left(f_2(x) - \int_0^x f_2(x-y)\phi(y)\,dy \right) \cos(\omega_\alpha t)\,. \end{aligned} \tag{3.55}$$

Theorem 3.3 *The shear beam model* (2.21), (3.6), (2.23), (2.24) *is satisfied by the state reference trajectories* (3.36) *and* (3.43), *where* $l(x,y)$ *satisfies* (3.31)–(3.33), $w^r(x,t)$ *is given in* (3.16), *and* $r(x,t)$ *is given in* (3.55). *The outputs of the system satisfy the tip displacement and deflection angle reference trajectories* (3.7), (3.45) *given the open-loop control inputs* (3.37), (3.44), *assuming* $u_0(x) = u^r(x,0)$ *and* $\dot{u}_0(x) = u_t^r(x,0)$.

Proof: The reference solutions (3.36) and (3.43) evaluated at $x = 0$ satisfy the desired free-end displacement and deflection angle reference trajectories. Equations (3.36) and (3.43) substituted into (2.21), (3.6), (2.23), (2.24) satisfy the shear beam PDE and free-end boundary conditions. ■

3.4 Reference Tracking

Reference tracking controllers combine the open-loop motion planning reference solutions with stabilizing feedback controllers. Their purpose is to stabilize the system and improve the rate of convergence to the reference solution when their exists a mismatch in initial conditions between the system state and reference solution.

Definition 3.1 *The reference trajectory* $u^r(x,t)$ *is said to be* exponentially stable *if there exist positive constants* M *and* m *such that*

$$\begin{aligned} &\left(\|u(t) - u^r(t)\|^2 + \|u_t(t) - u_t^r(t)\|^2 \right)^{1/2} \\ &\leq M\mathrm{e}^{-mt} \left(\|u_0 - u_0^r\|^2 + \|\dot{u}_0 - \dot{u}_0^r\|^2 \right)^{1/2}, \end{aligned} \tag{3.56}$$

where $\|\cdot\|$ *denotes the norm of* v, $\|v\| = \left(\int_0^1 v\,(x)^2\,dx \right)^{1/2}$, *and* $u_0(x) = u(x,0)$, $u_0^r(x) = u^r(x,0)$, $\dot{u}_0(x) = u_t(x,0)$, $\dot{u}_0^r(x) = u_t^r(x,0)$.

3.4.1 String

The tracking controller is an extension of the stabilizing controller in [41, 42].

Theorem 3.4 *The state feedback tracking controller*

$$\begin{aligned} u_x(1,t) &= -c_0 u(1,t) - c_1 u_t(1,t) - c_0 c_1 \int_0^1 u_t(y,t)\,dy \\ &\quad + w_x^r(1,t) + c_1 w_t^r(1,t)\,, \end{aligned} \tag{3.57}$$

exponentially stabilizes the string system (3.1), (3.2) *about the state reference trajectory* (3.9).

Proof: The expression for the boundary controller (3.57) is found by writing the standard boundary controller in [41, 42] in terms of the reference tracking error $\tilde{u}(x,t) = u(x,t) - u^r(x,t)$, where $w_x^r(1,t) + c_1 w_t^r(1,t) = u_x^r(1,t) + c_0 u^r(1,t) + c_1 u_t^r(1,t) + c_0 c_1 \int_0^1 u_t^r(y,t)\,dy$.

The string reference solution (3.9) satisfies the string model (3.1), (3.2), (3.57), and therefore has the same dynamics. The tracking error dynamics can then be written as

$$\varepsilon \tilde{u}_{tt} = (1 + d\partial_t)\,\tilde{u}_{xx} \tag{3.58}$$

$$\tilde{u}_x(0,t) = 0 \tag{3.59}$$

$$\tilde{u}_x(1,t) = -c_0 \tilde{u}(1,t) - c_1 \tilde{u}_t(1,t) - c_0 c_1 \int_0^1 \tilde{u}_t(y,t)\,dy\,, \tag{3.60}$$

which resemble the closed-loop string dynamics with a stabilizing controller. The direct and inverse backstepping transformations $\tilde{w}(x,t) = \tilde{u}(x,t) + c_0 \int_0^x \tilde{u}(y,t)\,dy$, and $\tilde{u}(x,t) = \tilde{w}(x,t) - c_0 \int_0^x \mathrm{e}^{-c_0(x-y)} \tilde{w}(y,t)\,dy$ relate the tracking error dynamics (3.58)–(3.60) and the exponentially stable tracking error target system

$$\varepsilon \tilde{w}_{tt} = (1 + d\partial_t)\,\tilde{w}_{xx} \tag{3.61}$$

$$\tilde{w}_x(0,t) = c_0 \tilde{w}(0,t) \tag{3.62}$$

$$\tilde{w}_x(1,t) = -c_1 \tilde{w}_t(1,t)\,. \tag{3.63}$$

The state of the tracking error system $\tilde{u}(x,t)$ can be bounded by the state of the tracking error target system $\tilde{w}(x,t)$ by $\|\tilde{u}(t)\| \leq (1 + c_0)\,\|\tilde{w}(t)\|$, and the same is true for the time derivatives, so the closed-loop system (3.1), (3.2), (3.57) is exponentially stable around the reference solution (3.9). ■

The string boundary controller (3.57) requires slope/force actuation at the base, but can also be written in a form that requires displacement actuation. When combined with the full state observers in [41, 42], the output-feedback tracking controller requires sensing of the free-end displacement and velocity.

3.4.2 Shear Beam

The tracking controllers for the shear beam are extensions of the stabilizing controllers in [39, 40, 43, 44].

Theorem 3.5 *The state feedback tracking controllers*

$$\begin{aligned} u_x(1,t) &= k(1,1)u(1,t) + \int_0^1 k_x(1,y)u(y,t)\,dy \\ &\quad -c_1 u_t(1,t) + c_1 \int_0^1 k(1,y)u_t(y,t)\,dy \\ &\quad +w_x^r(1,t) + c_1 w_t^r(1,t) - r_x(1,t) - c_1 r_t(1,t) \qquad (3.64) \\ \alpha(1,t) &= \cosh(b)\alpha^r(0,t) + b\sinh(b)u(0,t) \\ &\quad -b^2 \int_0^1 \cosh\left(b(1-y)\right) u(y,t)\,dy\,, \qquad (3.65) \end{aligned}$$

exponentially stabilize the shear beam (2.21), (3.6), (2.23), (2.24) *about the state reference trajectories* (3.36) *and* (3.43). *The tip displacement and deflection angle track* (3.7) *and* (3.45) *respectively.*

Proof: The expression for the boundary controller (3.64) is found by expressing the target system boundary condition (3.5) in terms of the tracking error $[w_x(1,t) - w_x^r(1,t)] = -c_1\left[w_t(1,t) - w_t^r(1,t)\right]$, and using the transformation (3.38) to substitute for $w_x(1,t)$ and $w_t(1,t)$.

Application of the boundary controller (3.65) makes the shear beam spatially causal. The shear beam reference solution (3.43) satisfies the strict-feedback shear beam model for motion planning (3.34), (3.35), (3.64), and therefore has the same

dynamics. The tracking error dynamics can then be written as

$$\begin{aligned}
\varepsilon\tilde{u}_{tt} &= (1+d\partial_t)\left(\tilde{u}_{xx}+b^2\tilde{u}-b^2\cosh(bx)\,\tilde{u}(0,t)\right.\\
&\quad \left.+b^3\int_0^x \sinh(b(x-y))\,\tilde{u}(y,t)\,dy\right) \qquad (3.66)\\
\tilde{u}_x(0,t) &= 0 \qquad (3.67)\\
\tilde{u}_x(1,t) &= k(1,1)\tilde{u}(1,t)+\int_0^1 k_x(1,y)\tilde{u}(y,t)\,dy-c_1\tilde{u}_t(1,t)\\
&\quad +c_1\int_0^1 k(1,y)\tilde{u}_t(y,t)\,dy\,, \qquad (3.68)
\end{aligned}$$

which resemble the closed-loop strict-feedback shear beam model dynamics. The direct and inverse backstepping transformations $\tilde{w}(x,t)=\tilde{u}(x,t)-\int_0^x k(x,y)\tilde{u}(y,t)\,dy$, and $\tilde{u}(x,t)=\tilde{w}(x,t)+\int_0^x l(x,y)\tilde{w}(y,t)\,dy$ relate the tracking error dynamics (3.66)–(3.68) to the exponentially stable tracking error target system (3.61)–(3.63). The state of the tracking error system can be upper bounded by the state of the tracking error target system, so the closed-loop system (2.21), (3.6), (2.23), (2.24), (3.64), (3.65) is exponentially stable around the reference solutions (3.36) and (3.43). ■

The shear beam boundary controllers (3.64), (3.65) require actuation of the slope (or displacement) and bending moment at the base. When combined with full state observers [39, 40, 43, 44], the output-feedback tracking controllers require sensing of the free-end displacement and velocity.

The Timoshenko beam control design in [43, 44] is done using a singular perturbation approach to reduce the Timoshenko beam to the shear beam model. The design is analogous to the shear beam design [39, 40], and all results for the shear beam apply *approximately* to the Timoshenko beam. Therefore the reference tracking results presented in Theorem 3.5 also apply approximately to the Timoshenko beam modulo an $O(\mu)$ residual in the tracking error.

3.5 Simulation Results

Simulations employ finite-differences to resolve partial derivatives in space, and the Crank-Nicolson method to march the equations forward in time.

3.5.1 String

This section presents simulation results for the string (3.1), (3.2) in closed-loop with the boundary controller (3.57). The spatial and temporal step sizes used in the simulations are $\Delta x = \frac{1}{100}$, and $\Delta t = \frac{1}{100}$ respectively. The string parameters are $d = 0.08$, and $\varepsilon = 5$, and the controller parameters are $c_0 = 100$, and $c_1 = 0.99\sqrt{5}$. The reference trajectory parameters are $A_u = \frac{1}{2}$ and $\omega_u = \pi$. The simulation was initialized with zero initial displacement and velocity.

Figures 3.5 and 3.6 present simulation results for the reference trajectory $u^r(0,t) = A_u[\sin(\omega_u t) + \sin(\sqrt{2}\omega_u t)]$. Generation and tracking of two sinusoids is achieved by implementing the boundary controller as a function of the linear combination of the target system reference solutions for each sinusoid. Figure 3.5 shows the evolution of the string state $u(x,t)$ as a sequence of snapshots in time, with increasing darkness corresponding to increasing time in each sequence. The reference trajectory at the corresponding time is represented by a circle at $x = 0$ of the same shade. Figure 3.6(a) compares the tip displacement $u(0,t)$ to the tip reference trajectory $u^r(0,t)$. Figure 3.6(b) compares the base displacement $u(1,t)$ to the reference displacement $u^r(1,t)$. Figure 3.6(c) compares the boundary input $u_x(1,t)$ to the reference boundary input $u_x^r(1,t)$.

3.5.2 Timoshenko Beam

This section presents simulation results for the Timoshenko beam model (2.21)–(2.24) in closed-loop with the state-feedback controllers (3.64), (3.65). The spatial and temporal step sizes used in simulation are $\Delta x = \frac{1}{100}$ and $\Delta t = \frac{1}{50}$ respectively. The beam parameters are $a = 5$, $d = 0.1$, $\varepsilon = 20$, and $\mu = 0.02$. The controller parameters are $c_0 = 100$ and $c_1 = 0.99\sqrt{20}$. The reference trajectory parameters are $A_u = \frac{1}{2}$, $\omega_u = \frac{\pi}{3}$, and $A_\alpha = \frac{1}{4}$, $\omega_\alpha = \pi$. The beam is initialized with an initial displacement $u(x,0) = -\frac{1}{10}(1-x)^2$, an initial deflection angle of $\alpha(x,0) = \frac{1}{5}(1-x)$, and zero initial velocity.

Figures 3.7–3.9 present results for the simultaneous tracking of the sinusoidal tip reference trajectories $u^r(0,t) = A_u \sin(\omega_u t)$ and $\alpha^r(0,t) = A_\alpha \sin(\omega_\alpha t)$. Figures

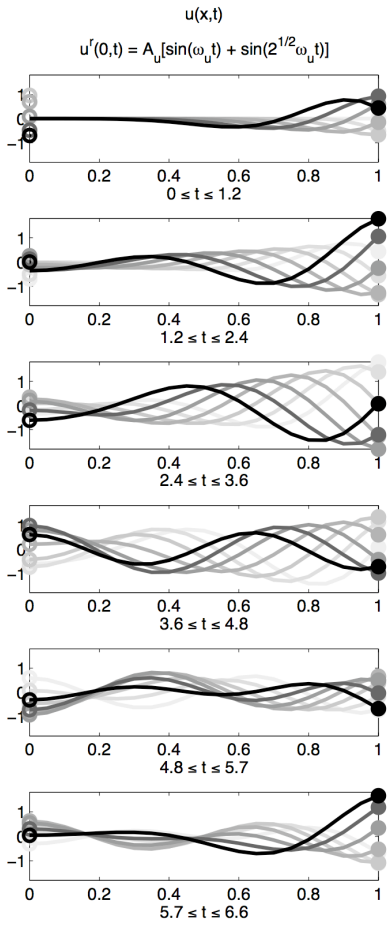

Figure 3.5: String simulation showing the state as snapshots in time.

3.7(a) and (b) show the evolution of the beam states $u(x,t)$ and $\alpha(x,t)$. Different time scales are used in Figures 3.7(a) and (b) since the u and α reference trajectories have different frequencies. Figures 3.8(a), (b) and (c) show the tip displacement tracking error $u(0,t) - u^r(0,t)$, the base displacement $u(1,t)$ and reference displacement $u^r(1,t)$, and the boundary control $u_x(1,t)$ and reference control $u_x^r(1,t)$ respectively. Figures 3.9(a) and (b) show the tip deflection angle tracking error $\alpha(0,t) - \alpha^r(0,t)$, and the boundary control $\alpha(1,t)$ and reference control $\alpha^r(1,t)$. Both tracking error plots show a periodic steady state error on the order of $\mu = 0.02$, with frequency ω_α.

Simultaneous tracking simulations have also been done for reference trajectories

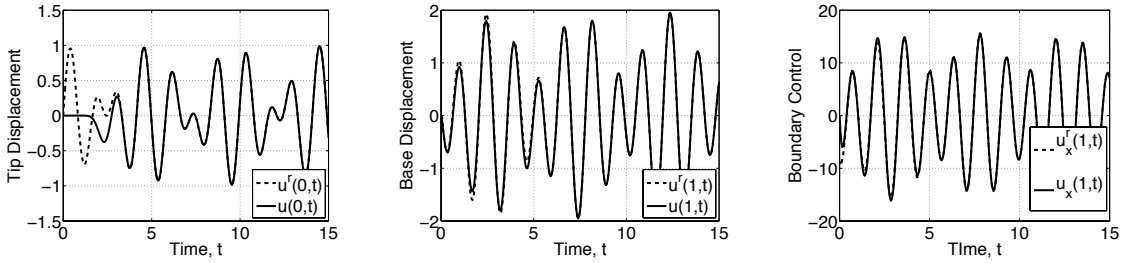

(a) (b) (c)

Figure 3.6: String simulation results comparing the (a) tip displacement $u(0,t)$ and reference trajectory $u^r(0,t)$, (b) base displacement $u(1,t)$ and reference displacement $u^r(1,t)$, and (c) boundary control input $u_x(1,t)$ and reference input $u_x^r(1,t)$.

where either $u^r(0,t)$ or $\alpha^r(0,t)$ are zero. Simulations with $u^r(0,t) = 0$, $\alpha^r(0,t) = A_\alpha \sin(\omega_\alpha t)$ show how the the approximate nature of the shear beam results applied to the Timoshenko beam appear as a periodic disturbance to the u-system. The $u_x(1,t)$ controller is not able to fully suppress the disturbance, and $u(x,t)$ exhibits $O(\mu)$ oscillations of frequency ω_α. Simulations with $u^r(0,t) = A_u \sin(\omega_u t)$, $\alpha^r(0,t) = 0$ do not exhibit the $O(\mu)$ tracking error, and the $\alpha(1,t)$ boundary controller stabilizes $\alpha(0,t)$ to zero.

Figures 3.10(a) and (b) show the control gains $k(1,y)$ and $k_x(1,y)$ on the interval $0 \leq y \leq 1$. The curves are relatively simple and can be approximated by quadratic and a linear functions respectively.

3.6 Conclusions

This chapter has presented explicit reference solutions to the motion planning problem for the wave equation (string and target system) and shear beam models with Kelvin-Voigt damping. The displacement reference solution was first found for the string, which is the simplest model being considered, then PDE backstepping transformations were used to find the displacement solutions for the target system and shear beam as a function of the string solution. PDE backstepping techniques were also used to find the deflection angle reference solution for the shear beam. Combining PDE boundary backstepping methods with classical trajectory gener-

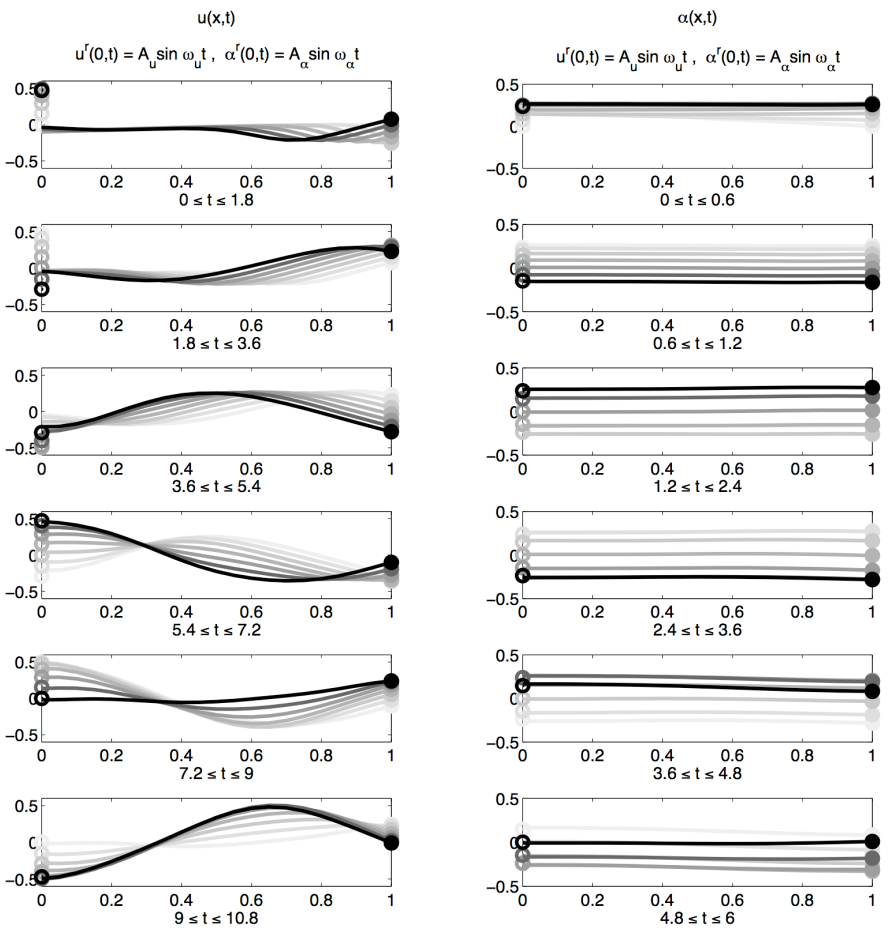

(a) (b)

Figure 3.7: Timoshenko beam simulation results showing snapshots of the beam states (a) $u(x,t)$ and (b) $\alpha(x,t)$.

ation methods simplified the problem of solving the motion planning problem for the shear beam, described by a wave equation coupled with an ODE, to finding the reference solution for the much simpler target system.

While this chapter has focused on motion planning for periodic trajectories, this approach extends to a far broader class of temporal waveforms, that includes polynomials, exponentials, sinusoids, and products thereof as special cases. With a slight modification one can obtain solutions to motion planning for all output reference trajectories that can be written in the form $u^r(0,t) = CX(t)$ where $X(t)$ is a solution of the autonomous linear 'exosystem' $\dot{X} = AX$ for a given initial condition

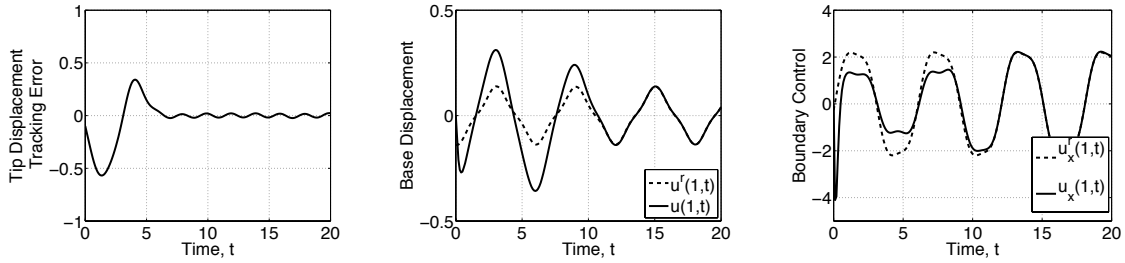

(a) (b) (c)

Figure 3.8: Timoshenko beam simulation results showing (a) the tip displacement tracking error $u(0,t) - u^r(0,t)$, (b) the base displacement $u(1,t)$ and the reference displacement $u^r(1,t)$, and (c) the boundary control $u_x(1,t)$ and the reference control $u_x^r(1,t)$.

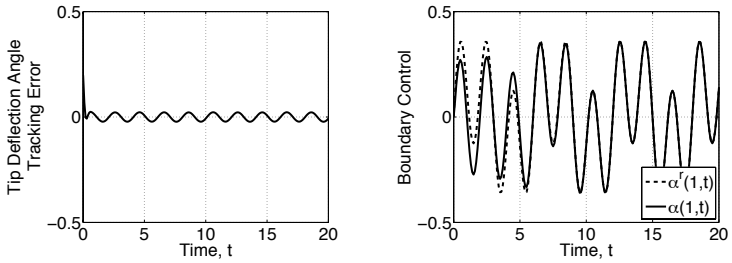

(a) (b)

Figure 3.9: Timoshenko beam simulation results showing (a) the tip deflection angle tracking error $\alpha(0,t) - \alpha^r(0,t)$, and (b) the boundary control $\alpha(1,t)$ and reference control $\alpha^r(1,t)$.

$X(0)$. For example, if the reference output is $u^r(0,t) = te^{-t}\sin t$, the parameters of the exosystem would be chosen as $C = [1\ 0\ 0\ 0]$, $A = \begin{bmatrix} 0 & 1 & 0 & 0 \\ 0 & 0 & 1 & 0 \\ 0 & 0 & 0 & 1 \\ -4 & -8 & -8 & -4 \end{bmatrix}$, $X(0) = [2\ 2\ 0\ 0]^{\mathrm{T}}$, and finding the motion planning solution would proceed using the matrix exponentials of A.

This chapter is in full an adaptation of material as it appears in: A. A. Siranosian, M. Krstic, A. Smyshlyaev, and M. Bement "Motion Planning and Tracking for Tip Displacement and Deflection Angle for Flexible Beams," *ASME Journal of Dynamic*

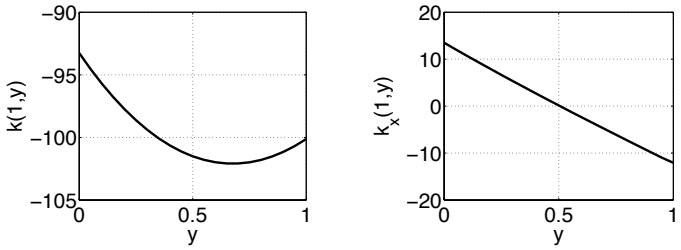

(a) (b)

Figure 3.10: Timoshenko beam gains (a) $k(1, y)$, and (b) $k_x(1, y)$.

Systems, Measurement and Control, to appear.

The dissertation author was the primary investigator and author of this paper.

4

Gain Scheduling-Inspired Control for Nonlinear PDE Systems

This chapter presents a control design method for nonlinear partial differential equations (PDEs) based on a combination of gain scheduling and backstepping theory for linear PDEs. A benchmark first-order hyperbolic system with an in-domain nonlinearity is considered first. For this system a nonlinear feedback law, based on gain scheduling, is derived explicitly, and a proof of local exponential stability, with an estimate of the region of attraction, is presented for the closed-loop system. Control designs (without proofs) are then presented for a string PDE and a shear beam PDE, both with Kelvin-Voigt damping and free-end nonlinearities of a potentially destabilizing kind. String and beam simulation results illustrate the merits of the gain scheduling approach over the linearization-based design.

4.1 Introduction

The stabilization of nonlinear partial differential equations (PDEs) is an important area in control design motivated by real-world applications in the areas of thermal, reaction, fluid, structural and plasma systems. Several control design methods for PDEs have been reported in the literature. The following is an overview of only those that are relatively broadly applicable, rather than being for a single

specific PDE. Finite dimensional backstepping methods were used for the design of stabilizing boundary controllers for spatially discretized parabolic PDEs in [7, 8, 9]. Nonlinear model reduction and input-output feedback linearization for quasilinear first-order hyperbolic and parabolic systems, were presented in [14]. Passivity based exponentially stabilizing control design and a flatness based approach for trajectory generation for flexible structures were presented in [48]. Feedforward and feedback controllers based on formal power series parameterization and summation methods for stabilization and tracking for nonlinear PDEs were presented in [54]. A gain scheduling approach for nonlinear PDEs in [4] used a linearization based approach, where controllers were designed for the finite-dimensional approximation of the system linearized about a family of operating points. An approach for full-state feedback linearization for a broad class of nonlinear parabolic partial integro-differential equations was presented in [77, 78], where the nonlinear feedback operators are constructed using Volterra series in the spatial variable.

This chapter presents a gain scheduling inspired control design for nonlinear PDEs based on the backstepping approach for linear PDEs. Gain scheduling [15, 16, 17, 35, 63, 64, 65, 66, 67, 68] is a technique that replaces a fully nonlinear control design (such as, for example backstepping or forwarding, which yield global stability) with the design of a family of linear controllers that are implemented according to a scheduling signal. It requires linearizing the plant about a family of operating points (ex. [64, 82, 83]) or the formulation of the model in a quasi-linear parameter varying (LPV) form (ex. [64, 68]), such that linear control tools can be applied. PDE backstepping [46] is an approach for the design of boundary controllers for infinite dimensional PDE models without discretization or model reduction. As a form of model reference control for infinite dimensional systems, state transformations relating a closed-loop system to a target system are used to design stabilizing controllers.

The design of a stabilizing controller begins by writing the PDE model in a form to which gain scheduling techniques apply. Once in the appropriate form, gain scheduled PDE backstepping transformations—similar to standard PDE backstepping transformations in structure, but employing state-dependent transformation

gains—are used to relate the nonlinear PDE model to a target system. Unlike typical gain scheduled controllers, where either the controller or its parameters are scheduled, the resulting controllers in this work are applied as nonlinear controllers (linear controllers with 'continuously scheduled' state-dependent parameters). While not as powerful as the exactly linearizing nonlinear PDE backstepping boundary controllers in [77, 78], gain scheduling controllers are a simpler and much more manageable design alternative for the challenging problem of nonlinear PDE control, with performance advantages over linearization based designs.

This chapter first presents an explicit gain scheduling-based control design for a benchmark first-order hyperbolic PDE with a boundary-value-dependent in-domain nonlinearity, which is an extension of the result in [45]. For this benchmark system a detailed analysis of local exponential stability is presented, with an estimate of the region of attraction. Even for this relatively simple nonlinear PDE system, the analysis is quite complex and highlights the issues that one would face in performing a stability analysis for more complex nonlinear PDEs with gain scheduling controllers. These issues include the construction of Lyapunov functionals using nonlinear backstepping transformations, the bounding of nonlinear terms left uncompensated in the gain scheduling approach, and perhaps most importantly, the choice of system norms and the derivation of stability estimates and regions of attraction in high enough Sobolev norms to capture the effect of nonlinear perturbations in the stability analysis.

The focus of this chapter is then turned to some relevant basic mechanical PDE systems—the string and shear beam PDEs with Kelvin-Voigt damping and boundary-displacement-dependent free-end nonlinearities. These designs are extensions of results for the string [41, 42, 69, 70], and shear beam [39, 40, 69, 70]. The merits of these designs are highlighted by simulation. Motivation for these systems comes from shake table control and from atomic force microscopy. In shake table control the table provides boundary actuation to a structure in order to impart a desired reference trajectory at some point near its free-end, which possibly exhibits nonlinear behavior. In atomic force microscopy the base of a cantilevered beam is actuated to stabilize a probe at its free-end, which interacts nonlinearly with the

sample surface.

The chapter is organized as follows. Section 4.2 presents the gain scheduling based control design for a benchmark first-order hyperbolic PDE with boundary-value-dependent in-domain nonlinearity. Section 4.3 presents the proof of stability for the resulting closed-loop system in Section 4.2. Sections 4.4 and 4.5 present the control design and simulation results for a string with Kelvin-Voigt damping and boundary-displacement-dependent free-end nonlinearity. Section 4.6 presents the control design for the shear beam with Kelvin-Voigt damping and boundary-displacement-dependent free-end nonlinearity. Section 4.7 presents simulation results for the Timoshenko beam with Kelvin-Voigt damping and boundary-displacement-dependent free-end nonlinearity, based on the shear beam designs of Section 4.6.

4.2 Gain Scheduling Design for a Benchmark First-Order Hyperbolic PDE

Consider the first-order hyperbolic PDE with a boundary-value-dependent in-domain nonlinearity

$$u_t(x,t) = u_x(x,t) + g(u(0,t))\mathrm{e}^{b(u(0,t))x}u(0,t) \tag{4.1}$$

where $u(x,t)$ is the state of the system on the domain $0 \leq x \leq 1$ at time $0 \leq t < \infty$, with initial condition $u_0(x) = u(x,0)$. Control is applied at $x = 1$ through the boundary condition $u(1,t)$. The functions $b(\cdot)$ and $g(\cdot)$ are arbitrary piecewise continuous functions. The nonlinearity $g(u(0,t))\mathrm{e}^{b(u(0,t))x}u(0,t)$ destabilizes the origin of the open-loop system (4.1), $u(1,t) = 0$, therefore some form of control is needed to stabilize the equilibrium $u \equiv 0$.

Though the gain scheduling design can be developed (and proved) for a much broader class of PDEs (not only first-order hyperbolic but also parabolic and second-order hyperbolic), and where nonlinearities include dependence on the full state $u(x,t)$, rather than on $u(0,t)$ only, (4.1) is used as a benchmark problem because all the steps of the analysis can be completed by explicit calculations.

The following steps are taken for the gain scheduling based PDE backstepping design. First, the nonlinearity is written in the quasi-linear parameter varying (LPV) form $\bar{f}(\cdot)u(\cdot)$. Following gain scheduling techniques $\bar{f}(\cdot)$ is considered to be a constant $\bar{f}$, then PDE backstepping techniques are used to find transformations relating the plant to a target system. Having found the transformations, $\bar{f}$ is replaced by $\bar{f}(\cdot)$ and a gain scheduling based nonlinear controller is found using PDE backstepping techniques. If work has already been done for a system with constant $\bar{f}$, i.e., a linear force, then $\bar{f}(\cdot)$ is simply substituted for $\bar{f}$ in those results.

For the current problem, the nonlinearity $g(u(0,t))\mathrm{e}^{b(u(0,t))x}u(0,t)$ is already in the LPV form, with $\bar{f}(\cdot) = g(\cdot)\mathrm{e}^{b(\cdot)x}$. Motivated by [45, Example 2.1] where b and g are constant, this work introduces the backstepping transformations

$$w(x,t) = u(x,t) - \int_0^x k\left(x,y,u(0,t)\right) u(y,t)\, dy \tag{4.2}$$

$$u(x,t) = w(x,t) + \int_0^x l\left(x,y,w(0,t)\right) w(y,t)\, dy\,, \tag{4.3}$$

where in the present problem with $b(u(0,t))$ and $g(u(0,t))$ the boundary-value-dependent gains are given by

$$k\left(x,y,u(0,t)\right) = -g(u(0,t))\mathrm{e}^{(g(u(0,t))+b(u(0,t)))(x-y)} \tag{4.4}$$

$$l\left(x,y,w(0,t)\right) = -g(w(0,t))\mathrm{e}^{b(w(0,t))(x-y)} \tag{4.5}$$

where $w(x,t)$ is the state of a first-order hyperbolic target system on the domain $0 \le x \le 1$ at time $0 \le t < \infty$, with initial condition $w_0(x) = w(x,0)$. The gain (4.4) was found by setting $b = b(u(0,t))$ and $g = g(u(0,t))$ in the results of [45, Example 2.1], while (4.5) was found following the general design steps, i.e., assume b, g constant and find $l(x,y)$ using PDE backstepping tools, then substitute $b(\cdot)$, $g(\cdot)$. Similar to [45, Example 2.1], the boundary controller is chosen as

$$u(1,t) = -\int_0^1 g\left(u(0,t)\right) \mathrm{e}^{(g(u(0,t))+b(u(0,t)))(1-y)} u(y,t)\, dy\,. \tag{4.6}$$

When b and g are constants the closed-loop system is equivalent to the exponentially stable target system $w_t(x,t) = w_x(x,t)$, $w(1,t) = 0$, whereas for general $b(\cdot)$ and $g(\cdot)$ the target system is

$$w_t(x,t) = w_x(x,t) - w_x(0,t) \int_0^x l_3\left(x,y,w(0,t)\right) w(y,t)\, dy \tag{4.7}$$

$$w(1,t) = 0\,, \tag{4.8}$$

where $l_3(x, y, w(0,t))$ is used to denote the partial derivative of $l(x, y, w(0,t))$ with respect to $w(0,t)$, and for this particular problem it is given by

$$l_3(x, y, w(0,t)) = -\left[g(w(0,t))\, b'(w(0,t))\,(x-y) + g'(w(0,t))\right] \mathrm{e}^{b(w(0,t))(x-y)}. \quad (4.9)$$

The main result of this section is that the gain scheduling based nonlinear controller is locally exponentially stabilizing with respect to the appropriate norm. In the context of gain scheduling, the 'continuously scheduled' controller is locally exponentially stabilizing independent of the magnitude of the rate of change of the scheduling signal $u(0,t)$.

Definition 4.1 *Let $\Gamma(t)$ denote the norm of the state of a dynamic system at time t. The equilibrium at the origin is said to be* locally exponentially stable *if there exist positive constants M, m, and γ such that for all initial states such that $\Gamma_0 < \gamma$, the following holds:*

$$\Gamma(t) \leq M\Gamma_0 \mathrm{e}^{-mt}, \quad \forall t \geq 0. \quad (4.10)$$

Theorem 4.1 *Consider the closed-loop system consisting of the plant* (4.1) *and the boundary controller* (4.6)*, and let*

$$\Omega(t) = u(0,t)^2 + \|u(t)\|^2 + \|u_x(t)\|^2 \quad (4.11)$$

denote its norm with respect to x at time t. The equilibrium $u \equiv 0$ of the closed-loop system is locally exponentially stable.

4.3 Proof of Theorem 4.1

The proof of Theorem 4.1 requires finding the stability properties of the equilibrium $w \equiv 0$ of the target system (4.7), (4.8), then relating those properties to the closed-loop system (4.1), (4.6) in the u-variable. First, results for the transformations and norms relating the systems are presented. Next a Lyapunov analysis is done to determine the stability of the equilibrium $w \equiv 0$ of the target system. The proof is completed by relating the results of the Lyapunov analysis in the w-variable to the u-variable using the system norms and the transformations. When

possible, spatial (x), temporal (t), and/or boundary displacement ($u(0,t)$, $w(0,t)$) dependence is suppressed.

Lemma 4.1 *The transformations $u \mapsto w$ and $w \mapsto u$ given by* (4.2)–(4.5) *are consistent (one is the inverse of the other).*

Proof: The partial derivative with-respect-to x of (4.2), with gain (4.4) can be written as $u' = b(u(0))u + w' - [b\,(u(0)) + g\,(u(0))]\,w$, which is a linear ODE with solution given by (4.3), (4.5). The partial derivative with-respect-to x of (4.3), with gain (4.5) can be written as $w' = [g\,(w(0)) + b\,(w(0))]\,w + u' - b\,(u(0))\,u$, which is a linear ODE with solution given by (4.2), (4.4). ■

Lemma 4.2 *Let the functions $u(x,t)$ and $w(x,t)$ be related by* (4.2)–(4.5). *The function $u(x,t)$ satisfies the nonlinear system* (4.1) *with boundary control* (4.6) *if and only if the function $w(x,t)$ satisfies the target system* (4.7), (4.8).

Proof: Substituting (4.3) into (4.1) and grouping terms gives

$$\begin{aligned} 0 &= u_t - u_x - g(u(0))\mathrm{e}^{b(u(0))x}u(0) \\ &= w_t - w_x + w_x(0)\int_0^x l_3\,(x,y,w(0))\,w(y)\,dy && \text{(4.12a)} \\ &\quad - \int_0^x \{l_x\,(x,y,w(0)) + l_y\,(x,y,w(0))\}\,w(y)\,dy && \text{(4.12b)} \\ &\quad - \left\{l\,(x,0,w(0)) + g(w(0))\mathrm{e}^{b(w(0))x}\right\}w(0)\,. && \text{(4.12c)} \end{aligned}$$

The expression in (4.12a) is satisfied by (4.7), and the braced expressions in (4.12b), (4.12c) are equal to zero given the inverse gain kernel (4.5). Substituting (4.3) into (4.6) gives

$$\begin{aligned} w(1,t) &= \int_0^1 \{l\,(1,y,w(0)) - k\,(1,y,w(0)) \\ &\quad - \int_y^1 k\,(1,\xi,w(0))\,l\,(\xi,y,w(0))\;d\xi\Big\}\,w(y)\,dy\,, && \text{(4.13)} \end{aligned}$$

where the braced expression in (4.13) is equal to zero given (4.4), (4.5). ■

Lemma 4.3 *Consider the target system* (4.7), (4.8), *with the Lyapunov function candidate*

$$V(t) = \int_0^1 (1+x)w^2(x,t)\,dx + \int_0^1 (1+x)w_x^2(x,t)\,dx\,. \qquad \text{(4.14)}$$

There exists a positive constant $\mathcal{V}$ such that if $V_0 \leq \mathcal{V}$ then

$$\dot{V}(t) \leq -\frac{1}{4}V(t)\,, \quad \forall t \geq 0\,. \tag{4.15}$$

Proof: The derivative of (4.14), with respect to time t, is

$$\dot{V}(t) \;=\; 2\int_0^1 (1+x)ww_t\,dx + 2\int_0^1 (1+x)w_xw_{xt}\,dx\,, \tag{4.16}$$

where w_t is given in (4.7), and the w_x-system is given by

$$\begin{aligned} w_{xt}(x,t) &= w_{xx}(x,t) - w_x(0,t)l_3\left(x,x,w(0,t)\right)w(x,t) \\ &\quad -w_x(0,t)\int_0^x l_{x3}\left(x,y,w(0,t)\right)w(y,t)\,dy \qquad (4.17) \\ w_x(1,t) &= w_x(0,t)\int_0^1 l_3\left(1,y,w(0,t)\right)w(y,t)\,dy \qquad (4.18) \end{aligned}$$

with (4.17) found by taking the partial derivative with-respect-to x of (4.7), and (4.18) found by evaluating (4.7) at $x = 1$ with $w_t(1) = 0$ from (4.8). Using (4.7) and (4.17) to substitute for w_t and w_{xt}, (4.16) can be written as

$$\begin{aligned} \dot{V}(t) &= 2\int_0^1 (1+x)w\left\{w_x - w_x(0)\int_0^x l_3\left(x,y,w(0)\right)w(y)\,dy\right\}dx \\ &\quad +2\int_0^1 (1+x)w_x\left\{w_{xx} - w_x(0)l_3\left(x,x,w(0)\right)w\right. \\ &\quad \left. -w_x(0)\int_0^x l_{x3}\left(x,y,w(0)\right)w(y)\,dy\right\}dx \\ &= w^2(1) - w^2(0) - \|w\|^2 + w_x^2(1) - w_x^2(0) - \|w_x\|^2 \\ &\quad -2w_x(0)\int_0^1 (1+x)w(x)\int_0^x l_3\left(x,y,w(0)\right)w(y)\,dy\,dx \\ &\quad -2w_x(0)\int_0^1 (1+x)w_x(x)l_3\left(x,x,w(0)\right)w(x)\,dx \\ &\quad -2w_x(0)\int_0^1 (1+x)w_x(x)\int_0^x l_{x3}\left(x,y,w(0)\right)w(y)\,dy\,dx\,, \qquad (4.19) \end{aligned}$$

where integration by parts was used to resolve the integrals $\int_0^1 (1+x)ww_x\,dx$ and $\int_0^1 (1+x)w_xw_{xx}\,dx$. Using (4.8) and (4.18) to substitute for $w(1)$ and $w_x(1)$ and taking the absolute value of the sign-indefinite terms, equation (4.19) can be bounded

by

$$\begin{aligned}
\dot{V}(t) \;\leq\; & -w^2(0) - w_x^2(0) - \|w\|^2 - \|w_x\|^2 && \text{(4.20a)}\\
& +2\left(w_x(0)\int_0^1 l_3\left(1,y,w(0)\right)w(y)\,dy\right)^2 && \text{(4.20b)}\\
& +2\left|w_x(0)\int_0^1(1+x)w(x)\int_0^x l_3\left(x,y,w(0)\right)w(y)\,dy\,dx\right| && \text{(4.20c)}\\
& +2\left|w_x(0)\int_0^1(1+x)l_3\left(x,x,w(0)\right)w(x)w_x(x)\,dx\right| && \text{(4.20d)}\\
& +2\left|w_x(0)\int_0^1(1+x)w_x(x)\int_0^x l_{x3}\left(x,y,w(0)\right)w(y)\,dy\,dx\right|. && \text{(4.20e)}
\end{aligned}$$

Given that $b(\cdot)$ and $g(\cdot)$ are piecewise continuous functions, the term in (4.20b) can be bounded in the form

$$2\left(w_x(0)\int_0^1 l_3\left(1,y,w(0)\right)w(y)\,dy\right)^2 \;\leq\; 2w_x^2(0)\left[a_1+\alpha_1\left(|w(0)|\right)\right]^2\|w\|^2, \quad (4.21)$$

the term in (4.20c) can be bounded in the form

$$\begin{aligned}
& 2\left|w_x(0)\int_0^1(1+x)w(x)\int_0^x l_3\left(x,y,w(0)\right)w(y)\,dy\,dx\right|\\
\leq\; & \frac{1}{4}w_x^2(0) + 16\left[a_1+\alpha_1\left(|w(0)|\right)\right]^2\|w\|^4, && \text{(4.22)}
\end{aligned}$$

the term in (4.20d) can be bounded in the form

$$\begin{aligned}
& 2\left|w_x(0)\int_0^1(1+x)l_3\left(x,x,w(0)\right)w(x)w_x(x)\,dx\right|\\
\leq\; & \frac{1}{4}w_x^2(0) + 16\left[a_2+\alpha_2\left(|w(0)|\right)\right]^2\|w_x\|^4, && \text{(4.23)}
\end{aligned}$$

and the term in (4.20e) can be bounded in the form

$$\begin{aligned}
& 2\left|w_x(0)\int_0^1(1+x)w_x(x)\int_0^x l_{x3}\left(x,y,w(0)\right)w(y)\,dy\,dx\right|\\
\leq\; & \frac{1}{4}w_x^2(0) + 16\left[a_3+\alpha_3\left(|w(0)|\right)\right]^2\|w_x\|^4, && \text{(4.24)}
\end{aligned}$$

where a_i, $i=1,2,3$, are constants defined as

$$\begin{aligned}
a_1 &= |g'(0)|\,\mathrm{e}^{|b(0)|} + |g(0)|\,|b'(0)|\,\mathrm{e}^{|b(0)|}\\
a_2 &= |g'(0)|\\
a_3 &= |g'(0)|\,|b(0)|\,\mathrm{e}^{|b(0)|} + |g(0)|\,|b(0)|\,|b'(0)|\,\mathrm{e}^{|b(0)|},
\end{aligned}$$

and $\alpha_i(\cdot)$ are class $\mathcal{K}_\infty$ functions chosen as

$$\begin{aligned}
\alpha_1(|w(0)|) &\geq |g'(w(0))|\, e^{|b(w(0))|} + |g(w(0))|\, |b'(w(0))|\, e^{|b(w(0))|} - a_1 \\
\alpha_2(|w(0)|) &\geq |g'(w(0))| - a_2 \\
\alpha_3(|w(0)|) &\geq |g'(w(0))|\, |b(w(0))|\, e^{|b(w(0))|} \\
&\quad + |g(w(0))|\, |b(w(0))|\, |b'(w(0))|\, e^{|b(w(0))|} - a_3 \,.
\end{aligned}$$

Using the bounds in (4.21)–(4.24), the Agmon inequality bound $|w(0)| \leq \|w_x\| \leq \sqrt{V}$, and defining the class $\mathcal{K}_\infty$ functions

$$\begin{aligned}
\beta_1\left(\sqrt{V}\right) &= \left[a_1 + \alpha_1\left(\sqrt{V}\right)\right]^2 V \\
\beta_2\left(\sqrt{V}\right) &= \left\{\left[a_2 + \alpha_2\left(\sqrt{V}\right)\right]^2 + \left[a_3 + \alpha_3\left(\sqrt{V}\right)\right]^2\right\} V \,,
\end{aligned}$$

the inequality in (4.20) can be bounded by

$$\begin{aligned}
\dot{V}(t) &\leq -w^2(0) - \left\{\frac{1}{4} - 2\beta_1\left(\sqrt{V}\right)\right\} w_x^2(0) \\
&\quad - \left\{1 - 16\beta_1\left(\sqrt{V}\right)\right\} \|w\|^2 - \left\{1 - 16\beta_2\left(\sqrt{V}\right)\right\} \|w_x\|^2 \,. \qquad (4.25)
\end{aligned}$$

Then for

$$V_0 \leq \mathcal{V} = \min\left\{\beta_1^{-1}\left(\frac{1}{8}\right)^2, \beta_1^{-1}\left(\frac{1}{32}\right)^2, \beta_2^{-1}\left(\frac{1}{32}\right)^2\right\}$$

(4.25) can be bounded by

$$\begin{aligned}
\dot{V}(t) &\leq -\frac{1}{2}\left(\|w\|^2 + \|w_x\|^2\right) \\
&\leq -\frac{1}{4} V(t) \,. \qquad (4.26)
\end{aligned}$$

■

Lemmas 4.1 and 4.2 show the existence of transformations relating the closed-loop system (4.1), (4.6) and the target system (4.7), (4.8). The transformations will now be used to relate a Lyapunov function candidate to the norm of the target system denoted by

$$\Psi(t) = \|w(t)\|^2 + \|w_x(t)\|^2 \,, \qquad (4.27)$$

and to the norm of the closed-loop system (4.11).

Lemma 4.4 *The Lyapunov function* (4.14) *is upper and lower bounded by*

$$\Psi(t) \leq V(t) \leq 2\Psi(t)\,. \tag{4.28}$$

Proof: Consider the quantity $(1+x)$ in (4.14). Setting x to zero (lower bound) and one (upper bound) produces the bounds in (4.28). ■

Lemma 4.5 *The equilibrium $w \equiv 0$ of the target system* (4.7), (4.8) *is locally exponentially stable.*

Proof: Equation (4.26) in Lemma 4.3 gives

$$V(t) \;\leq\; V_0 \mathrm{e}^{-t/4}\,, \quad \forall t \geq 0\,. \tag{4.29}$$

From Lemma 4.4 and (4.29), $\Psi(t) \leq V(t) \leq V_0\mathrm{e}^{-t/4} \leq 2\Psi_0\mathrm{e}^{-t/4}$ for $\Psi_0 \leq V_0$, therefore the equilibrium $w \equiv 0$ of the target system (4.7), (4.8) is locally exponentially stable. ■

Lemma 4.6 *There exist class $\mathcal{K}_\infty$ functions $\delta(\cdot)$ and $\rho(\cdot)$ such that*

$$\Psi(t) \;\leq\; \delta\left(\Omega(t)\right)\,, \tag{4.30}$$

and

$$\Omega(t) \;\leq\; \rho\left(\Psi(t)\right)\,. \tag{4.31}$$

Proof: The inequality in (4.30) is established as follows. The terms $\|w\|^2$ and $\|w_x\|^2$ can be bounded by

$$\|w\|^2 \;\leq\; \|u\|^2 + \max_{0\leq y\leq x\leq 1} \left|k\left(x,y,u(0)\right)\right|^2 \|u\|^2\,, \tag{4.32}$$

and

$$\begin{aligned} \|w_x\|^2 \;\leq\; & \|u_x\|^2 + \max_{0\leq x\leq 1]} \left|k\left(x,x,u(0)\right)\right|^2 \|u\|^2 \\ & + \max_{0\leq y\leq x\leq 1} \left|k_x\left(x,y,u(0)\right)\right|^2 \|u\|^2\,. \end{aligned} \tag{4.33}$$

Using (4.32) and (4.33), and given that $b(\cdot)$ and $g(\cdot)$ are piecewise continuous, (4.27) can be bounded by

$$\begin{aligned}
\Psi &= \|w\|^2 + \|w_x\|^2 \\
&\leq \left(1 + \max_{0\leq y\leq x\leq 1} |k(x,y,u(0))|^2 + \max_{0\leq x\leq 1} |k(x,x,u(0))|^2 \right. \\
&\quad \left. + \max_{0\leq y\leq x\leq 1} |k_x(x,y,u(0))|^2 \right) \|u\|^2 + \|u_x\|^2 \\
&\leq \left(1 + g^2 \mathrm{e}^{2(|g|+|b|)} + g^2 + g^2 (|g|+|b|)^2 \mathrm{e}^{2(|g|+|b|)}\right) \|u\|^2 + \|u_x\|^2 \\
&\leq (1 + a_4 + \alpha_4(|u(0)|)) \|u\|^2 + \|u_x\|^2 , \qquad (4.34)
\end{aligned}$$

where the constant a_4 is defined as

$$a_4 = g(0)^2 \mathrm{e}^{2(|g(0)|+|b(0)|)} + g(0)^2 + g(0)^2 (|g(0)|+|b(0)|)^2 \mathrm{e}^{2(|g(0)|+|b(0)|)} , \qquad (4.35)$$

and $\alpha_4(\cdot)$ is a class $\mathcal{K}_\infty$ function chosen as

$$\begin{aligned}
\alpha_4(|u(0)|) &\geq g(u(0))^2 \mathrm{e}^{2(|g(u(0))|+|b(u(0))|)} + g(u(0))^2 \\
&\quad + g(u(0))^2 (|g(u(0))|+|b(u(0))|)^2 \mathrm{e}^{2(|g(u(0))|+|b(u(0))|)} - a_4 . \qquad (4.36)
\end{aligned}$$

Then (4.34) can be bounded by

$$\begin{aligned}
\Psi &\leq (1 + a_4 + \alpha_4(|u(0)|)) \left(\|u\|^2 + \|u_x\|^2\right) \\
&\leq \left(1 + a_4 + \alpha_4\left(\sqrt{\Omega}\right)\right) \Omega \\
&= \delta(\Omega) . \qquad (4.37)
\end{aligned}$$

The inequality in (4.31) is established as follows. The terms $\|u\|^2$ and $\|u_x\|^2$ can be bounded by

$$\|u\|^2 \leq \|w\|^2 + \max_{0\leq y\leq x\leq 1} |l(x,y,w(0))|^2 \|w\|^2 , \qquad (4.38)$$

and

$$\begin{aligned}
\|u_x\|^2 &\leq \|w_x\|^2 + \max_{0\leq x\leq 1} |l(x,x,w(0))|^2 \|w\|^2 \\
&\quad + \max_{0\leq y\leq x\leq 1} |l_x(x,y,w(0))|^2 \|w\|^2 . \qquad (4.39)
\end{aligned}$$

Using (4.38) and (4.39), the bound $u(0) = w(0) \leq \|w_x\|$, and given that $b(\cdot)$ and $g(\cdot)$ are piecewise continuous functions, (4.11) can be bounded by

$$\begin{aligned}
\Omega &= u(0)^2 + \|u\|^2 + \|u_x\|^2 \\
&\leq \|w_x\|^2 + \Big(1 + \max_{0\leq y\leq x\leq 1} |l(x,y,w(0))|^2 + \max_{0\leq x\leq 1} |l(x,x,w(0))|^2 \\
&\quad + \max_{0\leq y\leq x\leq 1} |l_x(x,y,w(0))|^2\Big) \|w\|^2 + \|w_x\|^2 \\
&\leq \left(1 + g^2 \mathrm{e}^{2|b|} + g^2 + g^2 b^2 \mathrm{e}^{2|b|}\right) \|w\|^2 + 2\|w_x\|^2 \\
&\leq (1 + a_5 + \alpha_5(|w(0)|)) \|w\|^2 + 2\|w_x\|^2 , \qquad (4.40)
\end{aligned}$$

where the constant a_5 is defined as

$$a_5 = g(0)^2 \mathrm{e}^{2|b(0)|} + g(0)^2 + g(0)^2 b(0)^2 \mathrm{e}^{2|b(0)|} , \qquad (4.41)$$

and $\alpha_5(\cdot)$ is a class $\mathcal{K}_\infty$ function chosen as

$$\begin{aligned}
\alpha_5(|w(0)|) &\geq g(w(0))^2 \mathrm{e}^{2|b(w(0))|} + g(w(0))^2 \\
&\quad + g(w(0))^2 b(w(0))^2 \mathrm{e}^{2|b(w(0))|} - a_5 . \qquad (4.42)
\end{aligned}$$

Then (4.40) can be bounded by

$$\begin{aligned}
\Omega &\leq (2 + a_5 + \alpha_5(|w(0)|)) \left(\|w\|^2 + \|w_x\|^2\right) \\
&\leq \left(2 + a_5 + \alpha_5\left(\sqrt{\Psi}\right)\right) \Psi \\
&= \rho(\Psi) . \qquad (4.43)
\end{aligned}$$

■

The proof of Theorem 4.1 is completed next. Let

$$\omega = \delta^{-1}\left(\frac{\mathcal{V}}{2}\right) . \qquad (4.44)$$

Restricting the plant initial condition to $\Omega_0 \leq \omega$ implies that $V_0 \leq 2\Psi_0 \leq 2\delta(\Omega_0) \leq \mathcal{V}$, and from Lemmas 4.3–4.6 the norm $\Omega(t)$ of the closed-loop system can be bounded

as

$$\begin{aligned}\Omega(t) &\leq \rho\left(\Psi(t)\right)\\ &\leq \rho(V(t))\\ &\leq \rho\left(V_0 \mathrm{e}^{-t/4}\right)\\ &\leq \rho\left(2\Psi_0 \mathrm{e}^{-t/4}\right)\\ &\leq \rho\left(2\delta\left(\Omega_0\right)\mathrm{e}^{-t/4}\right). \end{aligned} \tag{4.45}$$

Given that ρ and δ are continuous and have a linear growth at the origin, an exponential stability estimate in the form (4.10) for $\Omega(t)$ is achieved.

4.4 Application to a String PDE

This section presents only the application of the gain scheduling based PDE backstepping techniques of Section 4.2 to the control design for a string with Kelvin-Voigt damping and boundary-displacement-dependent free-end nonlinearity. No theoretical results or stability analysis for a closed-loop system are presented here, but they can be pursued using the tools developed in Section 4.3. Conditions under which the results of this section would hold locally, proposed based on the results of Theorem 4.1, are summarized at the end of this section. The merits of the designs in this section are illustrated by simulation in Section 4.5.

Consider the string model given by (3.1) with the boundary condition

$$u_x(0,t) = f\left(u\left(0,t\right)\right). \tag{4.46}$$

The string is actuated at $x = 1$ through the force boundary input $u_x(1,t)$. The boundary-displacement-dependent function $f(\cdot)$, representing a free-end nonlinearity, is an arbitrary continuously differentiable function with $f(0) = 0$. Depending on the sign of $f'\left(u\left(0,t\right)\right) = \frac{df(u(0,t))}{du(0,t)}$ the nonlinear force can have either positive stiffness ($f' > 0$), or negative stiffness ($f' < 0$), i.e., "anti-stiffness," which is destabilizing. This work will consider systems with $f' < 0$ (at least locally), where control is required to stabilize the equilibrium $u \equiv 0$ of the closed-loop system. A gain scheduling based PDE backstepping design is chosen in hopes of improving

on linearization based results, both in the transient response and in the range of stability with respect to initial conditions.

Given that $f(u(0,t))$ is continuously differentiable and $f(0) = 0$, $f(\cdot)$ can be written in the necessary LPV form $\bar{f}(u(0,t))\,u(0,t)$, where the nonlinearity can be given explicitly, modeled, or approximated such that $u(0,t)$ can be factored out. The results in [41, Section 3] are for an undamped string ($d = 0$) with $\varepsilon = 1$, and linear destabilizing force, i.e., constant $\bar{f}$. The presence of KV damping and non-unity ε in this problem do not change the design compared to [41, Section 3]. The gain scheduling based backstepping transformations are then (4.2), (4.3), where in the present problem with $\bar{f}(u(0,t))$ the boundary-displacement-dependent gains are given by

$$k(x,y,u(0,t)) = \left[\bar{f}(u(0,t)) - c_0\right] \mathrm{e}^{-\bar{f}(u(0,t))(x-y)} \tag{4.47}$$

$$l(x,y,w(0,t)) = \left[\bar{f}(w(0,t)) - c_0\right] \mathrm{e}^{-c_0(x-y)} \tag{4.48}$$

where $w(x,t)$ is the state of the target system (3.3)–(3.5). Similar to [41] the boundary controller is chosen as

$$\begin{aligned} u_x(1,t) = {} & \left[\bar{f}(u(0,t)) - c_0\right] u(1,t) - c_1 u_t(1,t) \\ & - \bar{f}(u(0,t)) \left[\bar{f}(u(0,t)) - c_0\right] \int_0^1 \mathrm{e}^{-\bar{f}(u(0,t))(1-y)} u(y,t)\,dy \\ & + c_1 \left[\bar{f}(u(0,t)) - c_0\right] \int_0^1 \mathrm{e}^{-\bar{f}(u(0,t))(1-y)} u_t(y,t)\,dy\,. \end{aligned} \tag{4.49}$$

Here (4.47)–(4.49) were found by substituting $\bar{f} = \bar{f}(u(0,t))$ into [41, Equations (6), (7), (4)] $\Big($to be exact, $-q \equiv \bar{f}(u(0,t)$, $c_1 \equiv c_0$ and $c_2 \equiv c_1\Big)$. When $\bar{f}$ is constant, the closed-loop system (3.1), (4.46), (4.49) is equivalent to the exponentially stable target system (3.3)–(3.5). For general $\bar{f}(\cdot)$ the target system is

$$\begin{aligned} \varepsilon w_{tt}(x,t) = {} & (1 + d\partial_t)\, w_{xx}(x,t) - 2\varepsilon w_t(0,t) \int_0^x l_3(x,y,w(0,t))\, w_t(y,t)\,dy \\ & - \varepsilon \int_0^x \left[w_t(0,t)^2 l_{33}(x,y,w(0,t)) \right. \\ & \left. + w_{tt}(0,t) l_3(x,y,w(0,t)) \right] w(y,t)\,dy \end{aligned} \tag{4.50}$$

with boundary conditions (3.4), (3.5), where $l_3(x,y,w(0,t))$ denotes the partial derivative of $l(x,y,w(0,t))$ with respect to $w(0,t)$ and $l_{33}(x,y,w(0,t))$ denotes the

second partial derivative of $l(x, y, w(0,t))$ with respect to $w(0,t)$, which for this particular problem are given by

$$l_3\left(x, y, w(0,t)\right) = \left[\bar{f}'\left(w(0,t)\right) - c_0\right] \mathrm{e}^{-c_0(x-y)} \tag{4.51}$$

$$l_{33}\left(x, y, w(0,t)\right) = \left[\bar{f}''\left(w(0,t)\right) - c_0\right] \mathrm{e}^{-c_0(x-y)}\,. \tag{4.52}$$

The motion planning and tracking results of Chapter 3, which were developed only for $\bar{f} \equiv 0$, can also be extended to (3.1), (4.46) using gain scheduling techniques. The results for general $\bar{f}(\cdot)$ are found following the design techniques in Chapter 3 but with transformations (4.2), (4.3), (4.47), (4.48). The motion planning reference solution is

$$u^r(x,t) = w^r(x,t) + \left[\bar{f}\left(w^r(0,t)\right) - c_0\right] \int_0^x \mathrm{e}^{-c_0(x-y)} w^r(y,t)\, dy\,, \tag{4.53}$$

where $w^r(x,t)$ is the reference solution for the target system (3.3), (3.4), which for the sinusoidal tip displacement reference trajectory (3.14) is given by (3.16). The slope/force boundary input for motion planning is

$$\begin{aligned} u_x^r(1,t) &= w_x^r(1,t) + \left[\bar{f}\left(w^r(0,t)\right) - c_0\right] w^r(1,t) \\ &\quad -c_0 \left[\bar{f}\left(w^r(0,t)\right) - c_0\right] \int_0^1 \mathrm{e}^{-c_0(1-y)} w^r(y,t)\, dy\,, \end{aligned} \tag{4.54}$$

and the tracking boundary controller is

$$\begin{aligned} u_x(1,t) &= \left[\bar{f}\left(u(0,t)\right) - c_0\right] u(1,t) - c_1 u_t(1,t) \\ &\quad -\bar{f}\left(u(0,t)\right) \left[\bar{f}\left(u(0,t)\right) - c_0\right] \int_0^1 \mathrm{e}^{-\bar{f}(u(0,t))(1-y)} u(y,t)\, dy \\ &\quad +c_1 \left[\bar{f}\left(u(0,t)\right) - c_0\right] \int_0^1 \mathrm{e}^{-\bar{f}(u(0,t))(1-y)} u_t(y,t)\, dy \\ &\quad +w_x^r(1,t) + c_1 w_t^r(1,t)\,. \end{aligned} \tag{4.55}$$

The string boundary controllers (4.49) and (4.55) require slope/force actuation at the base, but can also be written in a form that requires displacement actuation. When combined with full state observers in [41, 42], the output-feedback controllers require sensing of the free-end displacement and velocity.

Following the results of Theorem 4.1, the initial conditions $u_0(x)$, $\dot{u}_0(x)$, $u_0(x) - u_0^r(x)$, and $\dot{u}_0(x) - \dot{u}_0^r(x)$, along with the reference trajectory $u^r(0,t)$ should be

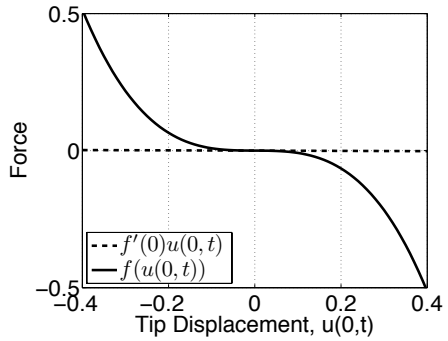

Figure 4.1: Comparison of the nonlinearity $f\left(u(0,t)\right)$ used in the string simulations, and its linear approximation $f'(0)u(0,t)$.

sufficiently small in the appropriate norms for the nonlinear controllers (4.49), and (4.55) to be exponentially stabilizing and for the reference solution (4.53) to hold. Such restrictions would seem to confine the operation to a linear region of $f(\cdot)$. Indeed, the advantage of using the nonlinear gain scheduled controls is impossible to quantify using the conservative analysis tools of Section 4.3. The advantage of gain scheduling based control over linearization based control is illustrated by simulations.

4.5 Simulations for the String

Simulations are done for the string (3.1), (4.46) with the stabilizing boundary controller (4.49) and tracking controller (4.55). The spatial and temporal step sizes are $\Delta x = \frac{1}{100}$ and $\Delta t = \frac{1}{100}$ respectively, the string parameters are $d = 0.08$ and $\varepsilon = 5$, and the controller parameters are $c_0 = 10$ and $c_1 = 0.99\sqrt{5}$. Figure 4.1 compares the softening nonlinearity $f\left(u(0,t)\right) = -\left[\frac{1}{200}u(0,t) + \left(2u(0,t)\right)^3\right]$ used in simulations and its linear approximation $f'(0)u(0,t)$. The boundary-displacement-dependent interaction force has a weak linear region near the origin, which is then dominated by the cubic nonlinearity. The linear approximation about the origin underestimates the interaction force, i.e., $|f'(0)u(0,t)| \leq |f\left(u(0,t)\right)|$ for all $u(0,t)$. In fact, any linear approximation would eventually underestimate a superlinear nonlinearity, which tend to be the most difficult to compensate for.

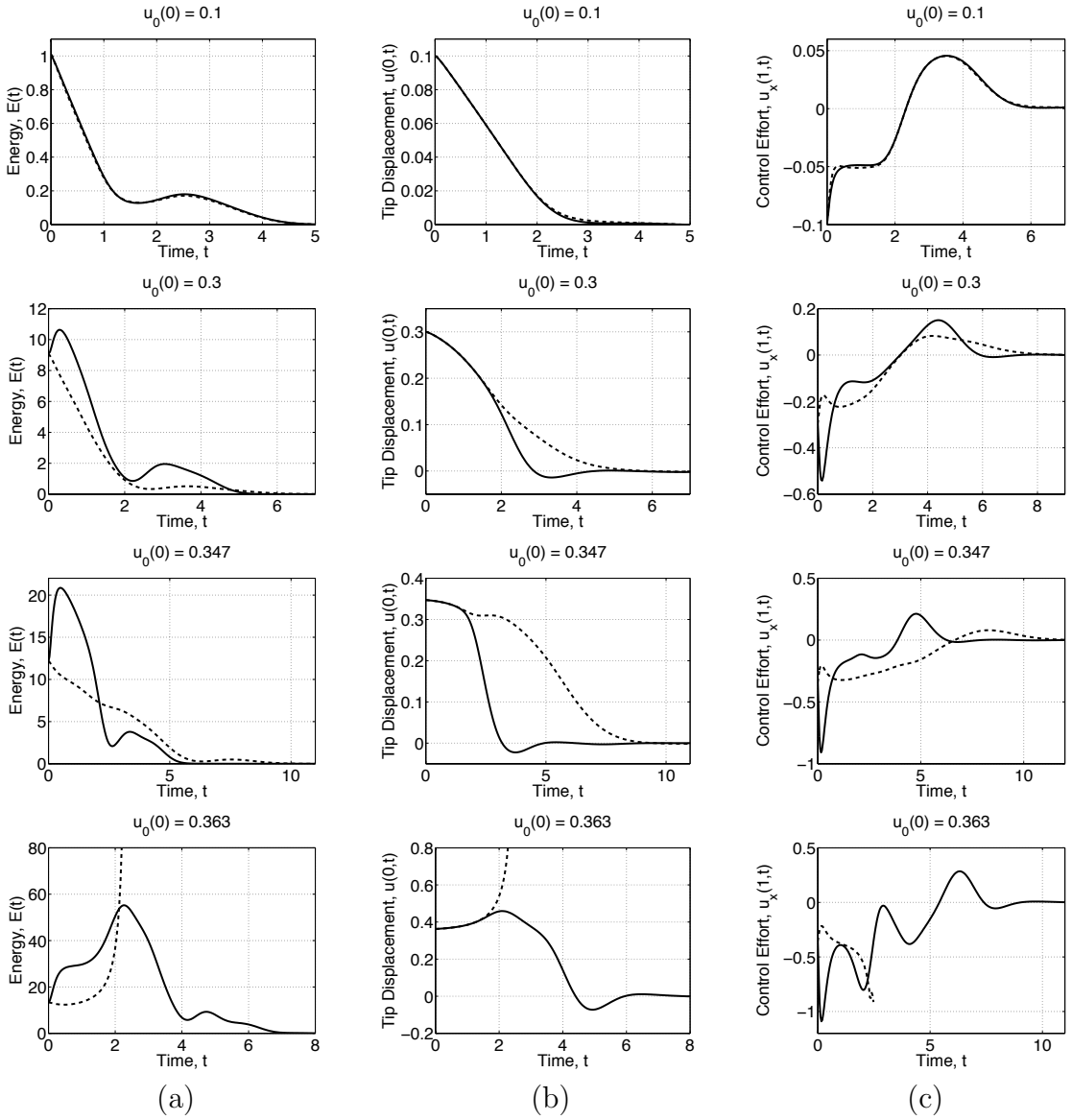

Figure 4.2: String simulation results for linearization based (dashed) and gain scheduling based nonlinear (solid) boundary control, for varying initial tip displacements. The plots compare (a) the energy, (b) the tip displacement, and (c) the boundary control effort.

Figure 4.2 compares the 'energy' $E(t) = \|u_t(x,t)\|^2 + \|u_x(x,t)\|^2$, tip displacement $u(0,t)$, and boundary control effort $u_x(1,t)$ of the closed loop system for the linearization based controller and the gain scheduling based nonlinear controller. The string is initialized with zero initial velocity and the initial displacement profile

$u_0(x) = u_0(0)\,(1-x)$ for the initial tip displacements $u_0(0) = \{0.1,\ 0.3,\ 0.347,\ 0.363\}$. For sufficiently small initial conditions ($u_0(0) = 0.1$), which lie in the linear region of the interaction force, both cases perform equally well. For intermediate initial conditions ($u_0(0) = 0.3$) (not shown) both cases stabilize the string with the gain scheduling based nonlinear controller achieving an improved transient response and slightly quicker settling time. When $u_0(0) = 0.347$, which is the largest initial condition for which the linearization based controller stabilizes the origin, the gain scheduling based nonlinear controller clearly outperforms the linearization based controller in both transient response and settling time. When $u_0(0) = 0.363$, which is the largest initial condition for which the gain scheduling based nonlinear controller stabilizes the origin, the linearization based controller can no longer stabilize the origin while the gain scheduling based nonlinear controller must work hard to keep the nonlinearity from pulling the tip away from the origin. The simulations show that—for a nonlinearity where the linearization underestimates the force—the gain scheduled based nonlinear controller outperforms the linearization based controller when the tip begins to operate in a sufficiently strong region of the nonlinear interaction force. The transient energy of the closed-loop system with gain scheduling based nonlinear control tends to be higher because of the increased control effort required for improved performance.

Figure 4.3 compares the performance of the linearization based controller and gain scheduling based nonlinear controller, when the goal is to generate and track the reference trajectory $u^r(0,t) = 0.3\sin\pi t$. The string is initialized with zero initial conditions. The gain scheduling based nonlinear controller is able to generate and track the sinusoid, with a small negative error in the mean. The negative error in the mean is caused by $u(0,t)$ interacting most with the nonlinearity through a negative peak of the sinusoid first. This is confirmed by simulations with $u^r(0,t) = -0.3\sin\pi t$ where the tip displacement interacts most with the nonlinearity through a positive peak of the sinusoid first, and the resulting error in the mean is positive. The negative mean causes a stronger interaction force for the negative peaks, which in turn causes phase tracking errors between them and the positive peaks. Conversely, the negative mean causes a weaker interaction force for the positive peaks, which

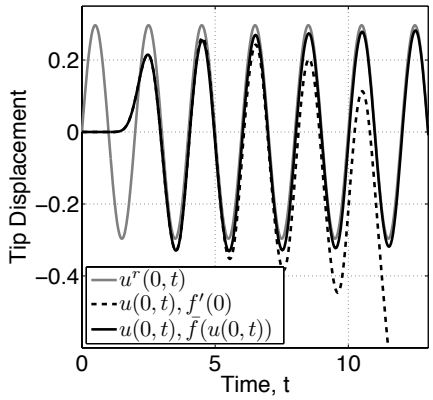

Figure 4.3: String simulation results comparing the tip displacement $u(0,t)$ and reference trajectory $u^r(0,t)$ when boundary control is applied with linearization based control and gain scheduling based nonlinear control.

allows for better tracking from positive to negative peaks. The plot also shows how the linearization based controller begins to generate and track the reference trajectory with the same error in the mean, but ultimately cannot compensate for the destabilizing force caused by increased interaction with the negative peaks. As with the stabilization simulations, the controllers have comparable performance for small reference amplitudes and the gain scheduled controller outperforms the linearization based controller when the amplitude increases, and neither controller can stabilize the reference trajectory when the reference amplitude is too large.

4.6 Application to the Shear Beam PDE

This section presents only the application of the gain scheduling based PDE backstepping techniques of Section 4.2 to the control design for the shear beam with Kelvin-Voigt damping and boundary-displacement-dependent free-end nonlinearity. No theoretical results or stability analysis for a closed-loop system are presented here, but they can be pursued using the tools developed in Section 4.3. Conditions under which the results of this section would hold locally, proposed based on the results of Theorem 4.1, are summarized at the end of the section. The merits of the results of this section are illustrated by simulation in Section 4.7.

Consider the Timoshenko beam model with Kelvin-Voigt damping and boundary-displacement-dependent free-end nonlinearity given as the coupled wave equations (2.21), (2.22) with free-end boundary conditions

$$u_x(0,t) = \alpha(0,t) + f\left(u\left(0,t\right)\right) \tag{4.56}$$

and (2.24). The $x = 0$ boundary conditions (4.56), (2.24) represent a free-end with nonlinear interaction force, and the beam is actuated at the end $x = 1$ through the boundary inputs $u_x(1,t)$ and $\alpha(1,t)$.

The shear beam model is written as a singular perturbation ($\mu = 0$) of the Timoshenko beam model, and is given by (2.21), (3.6) with boundary conditions (4.56), (2.24), and boundary inputs $u_x(1,t)$, $\alpha(1,t)$. As with the string, $f(\cdot)$ is considered to be destabilizing, and a gain scheduling based PDE backstepping design is chosen to stabilize $u \equiv 0$, $\alpha \equiv 0$.

The results in [40, Section 3] are for an undamped ($d = 0$) shear beam with linear destabilizing force, i.e., constant $\bar{f}$. The presence of KV damping in this problem does not change the design, and the gain scheduling based backstepping transformations are (4.2), (4.3), where for the present problem with $\bar{f}(u(0,t))$ the boundary-displacement-dependent gains satisfy the partial integro-differential equations (PIDEs)

$$\begin{aligned} k_{xx}\left(x,y,u(0,t)\right) &= k_{yy}\left(x,y,u(0,t)\right) + b^2 k\left(x,y,u(0,t)\right) - b^3 \sinh\left(b\left(x-y\right)\right) \\ &\quad + b^3 \int_y^x k\left(x,\xi,u(0,t)\right) \sinh\left(b\left(\xi-y\right)\right)\, d\xi \end{aligned} \tag{4.57}$$

$$k\left(x,x,u(0,t)\right) = -\frac{b^2}{2}x + \bar{f}\left(u(0,t)\right) - c_0 \tag{4.58}$$

$$\begin{aligned} k_y\left(x,0,u(0,t)\right) &= -b^2 \cosh\left(bx\right) + b^2 \int_0^x k\left(x,y,u(0,t)\right) \cosh\left(by\right)\, dy \\ &\quad + \bar{f}\left(u(0,t)\right) k\left(x,0,u(0,t)\right)\ , \end{aligned} \tag{4.59}$$

and

$$\begin{aligned} l_{xx}\left(x,y,w(0,t)\right) &= l_{yy}\left(x,y,w(0,t)\right) - b^2 l\left(x,y,w(0,t)\right) - b^3 \sinh\left(b\left(x-y\right)\right) \\ &\quad - b^3 \int_y^x l\left(x,\xi,w(0,t)\right) \sinh\left(b\left(\xi-y\right)\right)\, d\xi \end{aligned} \tag{4.60}$$

$$l\left(x,x,w(0,t)\right) = -\frac{b^2}{2}x + \bar{f}\left(w(0,t)\right) - c_0 \tag{4.61}$$

$$l_y\left(x,0,w(0,t)\right) = -b^2 \cosh\left(bx\right) + c_0 l\left(x,0,w(0,t)\right)\ . \tag{4.62}$$

Here (4.57)–(4.59) were found by substituting $-q \equiv \bar{f}(\cdot)$ in [40, Equation (3.9)], while (4.60)–(4.62) were found using gain scheduling based PDE backstepping techniques. Note that (4.57)–(4.59), (4.60)–(4.62) are families of PIDEs in independent variables (x, y), and parameterized by $u(0,t)$, $w(0,t)$. For each measured $u(0,t)$, $w(0,t)$ the PIDEs are solved and their solutions substituted appropriately. Given that $k(x,y,u(0,t))$ and $l(x,y,w(0,t))$ are implemented 'continuously,' then an alternative to numerically solving their respective PIDEs is to approximate the functions by the explicit first step of a symbolic recursion [40]. The first step of the recursion for the shear beam gains gives $k^0(x,y,u(0,t)) = \Pi(x,y,u(0,t))$ and $l^0(x,y,w(0,t)) = \Pi(x,y,w(0,t))$, where

$$\Pi(x,y,n) = -\frac{b}{2}\left[-\sinh\left(b(x-y)\right) + by\cosh\left(b(x-y)\right)\right] + \bar{f}(n) - c_0\,.$$

Similar to [40, Section 3] the locally stabilizing boundary controllers are chosen as

$$\begin{aligned} u_x(1,t) &= k(1,1,u(0,t))\,u(1,t) + \int_0^1 k_x(1,y,u(0,t))\,u(y,t)\,dy \\ &\quad -c_1 u_t(1,t) + c_1\int_0^1 k(1,y,u(0,t))\,u_t(y,t)\,dy \qquad (4.63) \\ \alpha(1,t) &= b\sinh(b)u(0,t) - b^2\int_0^1 \cosh\left(b(1-y)\right)u(y,t)\,dy\,. \qquad (4.64) \end{aligned}$$

The boundary controller (4.63) was found by making substitutions, similar to those made for the string, into [40, Equation 3.7], while (4.64) is carried over from [40, 39, 43, 44]. Numerical results in [44] show comparable performance of the boundary controllers when applied with the first step approximation $k^0(x,y,u(0,t))$ or with the numerical solution of (4.57)–(4.59). Similar to the string, when $\bar{f}$ is constant the closed-loop system (2.21), (3.6), (4.56), (2.24), (4.63), (4.64) is equivalent to the exponentially stable target system (3.3)–(3.5), and for general $\bar{f}(\cdot)$ the target system is (4.50), (3.4), (3.5) with $l(x,y,w(0,t))$ given by the numerical solution of (4.60)–(4.62), or approximated by $l^0(x,y,w(0,t))$.

The motion planning and tracking results of Chapter 3 can also be extended to (2.21), (3.6), (4.56), (2.24) using gain scheduling techniques. As with the string, motion planning and tracking results in Chapter 3 were developed only for $\bar{f} \equiv 0$. Results for general $\bar{f}(\cdot)$ are found following the techniques in Chapter 3 but with

the transformations (4.2), (4.3), (4.57)–(4.59), (4.60)–(4.62). The gain scheduling based backstepping transformations for motion planning and tracking are

$$w(x,t) = u(x,t) + r(x,t) - \int_0^x k(x,y,u(0,t))u(y,t)\,dy \tag{4.65}$$

$$u(x,t) = w(x,t) - r(x,t) + \int_0^x l(x,y,w(0,t))\left[w(y,t) - r(y,t)\right]\,dy \tag{4.66}$$

where $k(x,y,u(0,t))$ and $l(x,y,w(0,t))$ are given by (4.57)–(4.59), (4.60)–(4.62), and $r(x,t)$ is the state of the auxiliary system (3.39)–(3.41). The motion planning reference solutions are

$$u^r(x,t) = w^r(x,t) - r(x,t) + \int_0^x l\left(x,y,w^r(0,t)\right)\left[w^r(y,t) - r(y,t)\right]\,dy \tag{4.67}$$

and (3.36), where for the sinusoidal tip displacement and deflection angle reference trajectories (3.7) and (3.45) $w^r(x,t)$ is given by (3.16), and $r(x,t)$ is given by (3.55). The boundary inputs for motion planning are

$$\begin{aligned} u_x^r(1,t) &= w_x^r(1,t) - r_x(1,t) + l\left(1,1,w^r(0,t)\right)\left[w^r(1,t) - r(1,t)\right] \\ &\quad + \int_0^1 l_x\left(1,y,w^r(0,t)\right)\left[w^r(y,t) - r(y,t)\right]\,dy \end{aligned} \tag{4.68}$$

$$\begin{aligned} \alpha^r(1,t) &= \cosh(b)\alpha^r(0,t) + b\sinh(b)u^r(0,t) \\ &\quad - b^2\int_0^1 \cosh\left(b(1-y)\right)u^r(y,t)\,dy\,, \end{aligned} \tag{4.69}$$

and the tracking boundary controllers are

$$\begin{aligned} u_x(1,t) &= k\left(1,1,u(0,t)\right)u(1,t) + \int_0^1 k_x\left(1,y,u(0,t)\right)u(y,t)\,dy \\ &\quad - c_1 u_t(1,t) + c_1\int_0^1 k\left(1,y,u(0,t)\right)u_t(y,t)\,dy \\ &\quad + w_x^r(1,t) + c_1 w_t^r(1,t) - r_x(1,t) - c_1 r_t(1,t) \end{aligned} \tag{4.70}$$

$$\begin{aligned} \alpha(1,t) &= \cosh(b)\alpha^r(0,t) + b\sinh(b)u(0,t) \\ &\quad - b^2\int_0^1 \cosh\left(b(1-y)\right)u(y,t)\,dy\,. \end{aligned} \tag{4.71}$$

The beam boundary controllers (4.63), (4.64) and (4.70), (4.71) require actuation of the slope (or displacement) and bending moment at the base. When combined with full state observers in [39, 40, 43, 44], the output-feedback controllers require sensing of the free-end displacement and velocity.

Based on the results of Theorem 4.1, the initial conditions $u_0(x)$, $\dot{u}_0(x)$, $u_0(x) - u_0^r(x)$, and $\dot{u}_0(x) - \dot{u}_0^r(x)$, along with the reference trajectory $u^r(0,t)$ should be sufficiently small in the appropriate norms for the nonlinear controllers (4.63), (4.64) and (4.70), (4.71) to be exponentially stabilizing and for the reference solutions (4.67), (3.36) to hold. Such restrictions would seem to confine the operation to a linear region of $f(\cdot)$. Since the advantage of using the nonlinear gain scheduled controls is impossible to quantify using the conservative analysis tools of Section 4.3, then the advantage of gain scheduling based control over linearization based control is illustrated by simulations in Section 4.7.

4.7 Simulations for the Timoshenko Beam

The Timoshenko beam control design in [43, 44] is done using a singular perturbation approach to reduce it to the shear beam model, with the rest of the design being analogous to the shear beam results in [39, 40]. All results for the shear beam apply *approximately* to the Timoshenko beam, therefore the gain scheduling based designs for the shear beam also apply approximately to the Timoshenko beam.

Simulations are done for the Timoshenko beam (2.21), (2.22), (4.56), (2.24) with the stabilizing boundary controllers (4.63), (4.64) and tracking controllers (4.70), (4.71) using the numerical solution to the gain PIDE (4.57)–(4.59). The spatial and temporal step sizes are $\Delta x = \frac{1}{100}$ and $\Delta t = \frac{1}{50}$ respectively, the beam parameters are $a = 5$, $d = 0.1$, $\varepsilon = 10$, and $\mu = 0.02$, and the controller parameters are $c_0 = 10$ and $c_1 = 0.99\sqrt{10}$. String simulations were done with a superlinear nonlinearity which required a more aggressive control action. Beam simulations are done with a sublinear nonlinearity which requires a less aggressive control action. Figure 4.4 compares the nonlinearity $f\left(u(0,t)\right) = \frac{-Fu(0,t)}{1+(3u(0,t))^2}$ for $F = 1$, where F is the linear strength of the force, and its linear approximation about the origin. The boundary-displacement-dependent interaction force has a linear region about the origin, which is then dominated by the quadratic nonlinearity in the denominator. The linear approximation overestimates the interaction force, i.e. $|f'(0)u(0,t)| \geq |f\left(u(0,t)\right)|$ for all $u(0,t)$. This sublinear nonlinearity is easier to compensate for compared

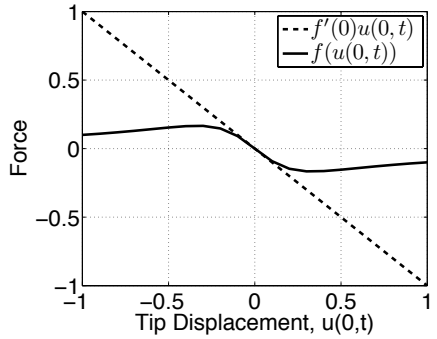

Figure 4.4: Comparison of the nonlinearity $f\left(u(0,t)\right)$ used for the beam simulations, and its linear approximation $f'(0)u(0,t)$, for $F = 1$.

to superlinear nonlinearity used for the string since, though it may destabilize the origin, its strength decreases far from the origin and it can add two new stable equilibria at $|u(0,t)| > 0$.

Figure 4.5 compares the energy $E(t)$, tip displacement $u(0,t)$, and boundary control effort $u_x(1,t)$ of the closed loop system for the linearization based controller and the gain scheduling based nonlinear controller. The beam is initialized with zero initial velocity and the initial displacement and deflection angle profiles $u_0(x) = \frac{3}{10}\left(1-x\right)^2$ and $\alpha_0(x) = -\frac{3}{5}\left(1-x\right)$, and the nonlinearity strength is varied as $F = \{0.1,\, 0.3,\, 0.53,\, 2,\, 2.8\}$. The goal of these simulations is to compare the two control implementations, as opposed to finding the best control parameters c_0 and c_1 for a particular F, therefore the same c_0 and c_1 were used for all values of F. For a very weak force ($F = 0.1$, not shown), the controllers have similar performance. As the strength of the force increases ($F = 0.3$ to $F = 0.53$) the nonlinear controller consistently performs well. Conversely, performance of the linearization based controller begins to degrade as the overestimating nature of the gain induces oscillation and the origin transitions from stable, to marginally stable, to unstable. For a strong force ($F = 2$) the nonlinear controller is still able to stabilize the origin. The gain scheduled controller extends the range of stability to $F = 2.8$ (not shown), which is the largest value for which the nonlinear controller (with $c_0 = 10$) preserves stability of the origin. Simulations with $F = 2.8$ show that increasing the value of c_0 improves performance, suggesting that c_0 should be increased proportional to

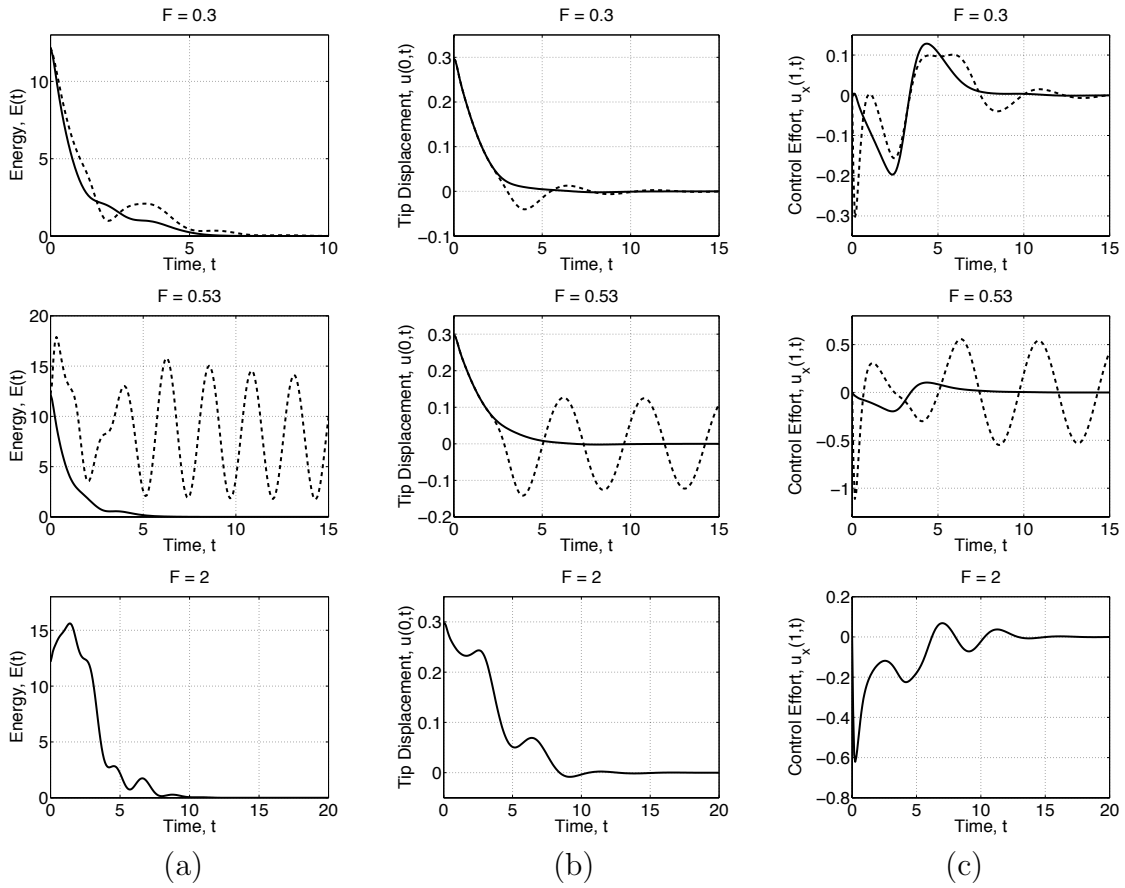

Figure 4.5: Beam simulation results for linearization based (dashed) and gain scheduling based nonlinear (solid) boundary control for various nonlinearity strengths. The plots compare the (a) energy, (b) tip displacement, and (c) boundary control effort.

F, though ultimately the gain scheduling based nonlinear controller cannot stabilize the origin for very large F. The simulations show that—for a nonlinearity where the linearization overestimates the force—the nonlinear controller outperforms the linearization based controller when the nonlinear interaction force becomes sufficiently strong, and it extends the range of stability.

Figure 4.6 compares the performance of the linearization based controller and gain scheduling based nonlinear controller when the goal is to generate and track the reference trajectory $u^r(0,t) = 0.5\sin(\pi t/3)$, $\alpha^r(0,t) = 0$. The beam is initialized with zero initial conditions. The plot shows how the linearization based controller

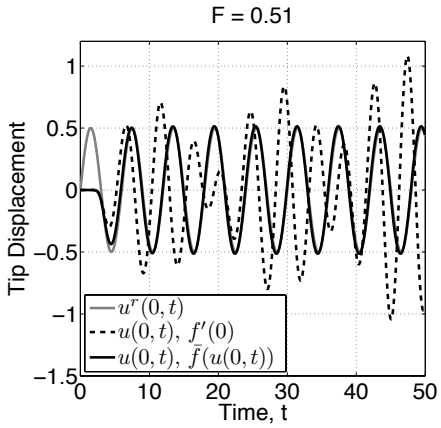

Figure 4.6: Beam simulation results comparing the tip displacement and reference trajectory when boundary control is applied with linearization based control and gain scheduling based nonlinear control.

begins to generate the reference trajectory, but in overestimating the nonlinearity it applies an excess of control effort producing large amplitude and phase errors, and cannot compensate for the harmonics caused by interaction with the nonlinearity. The linearization based controller eventually destabilizes the system for larger time. The gain scheduling based nonlinear controller is able to generate and track the sinusoid with very small errors in amplitude and phase, part of which can be attributed to the approximate nature of the shear beam results applied to the Timoshenko beam [69, 70]. The controllers have comparable performance for small reference amplitudes and force strengths, the gain scheduled controller outperforms the linearization based controller when the reference amplitude or force strength increases, and neither controller can stabilize the reference trajectory when the strength of the force is too large.

4.8 Conclusions

A control design for nonlinear PDEs inspired by gain scheduling and based on the backstepping theory for linear PDEs has been introduced. Control designs were presented for a benchmark first-order hyperbolic PDE with boundary-value-dependent in-domain nonlinearity, and for the string and shear beam with Kelvin-

Voigt damping and boundary-displacement-dependent free-end nonlinearities. The benchmark system was used to illustrate how one can perform a stability analysis of a nonlinear PDE system with gain scheduling based nonlinear control. Stability analysis showed that the equilibrium $u \equiv 0$ of the closed-loop system was locally exponentially stable. String and Timoshenko beam simulations were presented to show the performance of the gain scheduling based nonlinear controllers, which outperformed simple linearization based controllers.

Gain scheduling based PDE boundary backstepping methods provide a simple and effective solution to the difficult problem of nonlinear control design for infinite dimensional nonlinear systems. While not as powerful as a full nonlinear design, gain scheduling based PDE backstepping theory produces tractable results that outperform simple linearization based design.

This chapter is in full an adaptation of material as it appears in: A. A. Siranosian, M. Krstic, A. Smyshlyaev, and M. Bement "Gain Scheduling-Inspired Control for Nonlinear PDEs," submitted to the *ASME Journal of Dynamic Systems, Measurement and Control*.

The dissertation author was the primary investigator and author of this paper.

5

Extremum Seeking Tuned Positive-Position-Feedback Compensators

This chapter presents work done to design an extremum seeking based tuning algorithm for optimizing the performance of a positive position feedback (PPF) compensator. An analysis of a closed-loop system consisting of a second order plant (spring-mass-damper) and the PPF compensator is done to find conditions under which the compensator preserves stability of the origin. The compensator parameters are redefined in order to satisfy the necessary condition for stability and to simplify the problem from tuning three compensator parameters to tuning only one. The ES based tuning algorithm is then presented for a PPF compensator applied to the linear second-order system.

5.1 Introduction

The positive position feedback (PPF) compensator [25, 30, 31, 84], first reported in [31] as a more appealing alternative to velocity feedback, has been studied as a viable option for non-model based collocated control of flexible structures since it is insensitive to the uncertain internal damping of a structure [31], and to spillover

caused by unmodeled higher modes [30, 84]. Also, the closed-loop system is not destabilized by finite actuator dynamics, and its stability properties depend only on the structures natural frequency [30]. Assuming a PPF compensator is used to attenuate vibrations at a structure's natural frequency, then the compensator is usually tuned to resonate at that same frequency to add damping [84].

In cases where the plant dynamics are uncertain or possibly time varying, or there exists a disturbance of varying frequency, then it would be advantageous for a compensator such as PPF, which relies on focusing its energy around a particular frequency, to adjust accordingly. There can also be cases where a PPF compensator is not applied as collocated control, where the compensator suppresses vibrations at the same location it is sensing them, in which case it would be advantageous to tune the PPF compensator of optimal performance. One such method for achieving this is extremum seeking (ES), which continuously probes a system and tunes parameters such that optimal performance achieved.

This work considers the application of a PPF compensator to suppress a single sinusoidal disturbance to a plant. The plant model is chosen as a second order system, as opposed to an infinite dimensional system, for simplicity. A stability analysis of the closed-loop system is first done to ensure that the PPF will not destabilize the origin. The compensator gain is then redefined, in terms of the compensator natural frequency, in order to satisfy the necessary condition for stability, which requires only knowledge of the plant gain and natural frequency. The compensator damping is also redefined in terms of natural frequency of the compensator in order to simplify the problem from tuning three parameters, to tuning one. Then an ES based tuning algorithm is designed to tune the PPF compensator natural frequency to optimize the performance of the compensator applied to the linear plant.

The chapter is organized as follows. Section 5.2 presents a general single parameter extremum seeking scheme, which will be used for the tuned PPF compensators. Section 5.3 presents the PPF compensator with stability analysis of a second order system in feedback with the compensator, and the extremum seeking based tuning design. Section 5.4 presents simulation results.

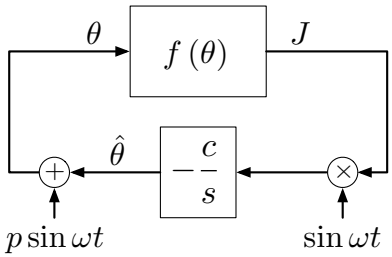

Figure 5.1: Block diagram of general single parameter extremum seeking scheme.

5.2 General Single Parameter Extremum Seeking

Figure 5.1 shows the block diagram of a general single parameter extremum seeking (ES) scheme [2]. ES tunes the signal $\hat{\theta}$ such that it approaches the optimal value θ^*, which corresponds to a local extrema f^* of the unknown nonlinear map $f(\theta)$. The method does so by employing a sinusoidal perturbation ($p \sin \omega t$) to continuously probe the map. It extracts the map's local gradient information using the demodulated signal $J \sin \omega t$, and then tunes $\hat{\theta}$ using the integrator with adaptation gain c.

Some general comments can be made about the performance and stability of the scheme shown in Figure 5.1. Consider a nonlinear map of the form

$$f(\theta) \;=\; f^* + \frac{f''}{2}\left(\theta - \theta^*\right)^2 , \tag{5.1}$$

which locally approximates any twice-continuously-differentiable (C^2) function. The constant $f'' > 0$ corresponds to θ^* being the location of a minimum, while $f'' < 0$ corresponds to θ^* being the location of a maximum. For $cf'' > 0$, this scheme is locally exponentially stable to an $O\left(p^2 + 1/\omega^2\right)$ neighborhood of θ^*. This suggests that the sign of c must be chosen based on some knowledge of the map (whether it is to be minimized or maximized), and the perturbation frequency ω should be sufficiently large and the perturbation amplitude p should be sufficiently small, in order for the ES tuning to perform well. Note that the location of the maximum θ^* can be a function of time, in which case the perturbation frequency should be sufficiently fast compared to $\dot{\theta}^*$.

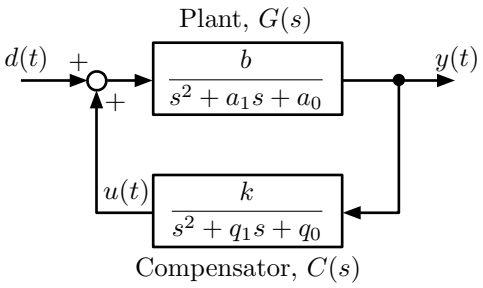

Figure 5.2: Positive feedback interconnection of plant $G(s)$ and compensator $C(s)$.

5.3 Tuned PPF Compensator

Consider the spring-mass-damper system given by a transfer function $G(s)$ of the form

$$G(s) = \frac{Y(s)}{D(s)} = \frac{b}{s^2 + a_1 s + a_0} \tag{5.2}$$

in feedback with the positive-position-feedback (PPF) [31] compensator given by a transfer function $C(s)$ of the form

$$C(s) = \frac{U(s)}{Y(s)} = \frac{k}{s^2 + q_1 s + q_0}\,, \tag{5.3}$$

where $D(s)$ is a disturbance entering the plant, $U(s)$ is the control effort, and $Y(s)$ is the position output of the plant. The strictly positive constants a_0, a_1, and b are plant parameters and k, q_0, and q_1 are the compensator parameters to be tuned.

Figure 5.2 shows the feedback interconnection of the plant and compensator. The characteristic equation for the closed loop system, which for positive feedback is given by $1 - G(s)C(s) = 0$, is

$$s^4 + (a_1 + q_1)\, s^3 + (a_0 + q_0 + a_1 q_1)\, s^2 + (a_1 q_0 + a_0 q_1)\, s + (a_0 q_0 - bk) = 0\,. \tag{5.4}$$

The necessary condition for stability, which states that all coefficients of (5.4) be strictly positive, is satisfied by all the coefficients except $a_0 q_0 - bk$. Assuming the plant gain, b, and natural frequency, $\sqrt{a_0}$, are known, or can be found, then k can be parameterized as

$$k = (1 - c_0)\,\frac{a_0 q_0}{b}\,, \tag{5.5}$$

which reduces the s^0 coefficient to $a_0q_0 - bk = c_0a_0q_0 > 0$ and satisfies the necessary condition for stability for any $c_0 > 0$. Since $c_0 = 1$ makes $k = 0$, which is equivalent to having no control, and values of $c_0 > 1$ change the compensator from positive to negative feedback, c_0 is bounded between zero and one ($0 < c_0 < 1$). A further simplification is made by parameterizing q_1 as

$$q_1 = c_1 q_0 \,, \;\; c_1 > 0 \,. \tag{5.6}$$

Using the parameterizations in (5.5) and (5.6), the characteristic equation simplifies to

$$s^4 + (a_1 + c_1 q_0)\, s^3 + (a_0 + q_0 + c_1 a_1 q_0)\, s^2 + (a_1 q_0 + c_1 a_0 q_0)\, s + c_0 a_0 q_0 = 0 \,, \tag{5.7}$$

which can be written as

$$1 + q_0 \frac{c_1 s^3 + (1 + c_1 a_1)\, s^2 + (a_1 + c_1 a_0)\, s + c_0 a_0}{s^2\,(s^2 + a_1 s + a_0)} \;\; = \;\; 0 \,, \tag{5.8}$$

or in the root locus form $1 + K\frac{b(s)}{a(s)} = 0$ as

$$1 + c_1 q_0 \frac{s^3 + \left(\frac{1}{c_1} + a_1\right) s^2 + \left(\frac{a_1}{c_1} + a_0\right) s + \frac{c_0 a_0}{c_1}}{s^2\,(s^2 + a_1 s + a_0)} \;\; = \;\; 0 \,, \tag{5.9}$$

where $a(s)$ and $b(s)$ are monic polynomials, and q_0 is the parameter to be tuned by extremum seeking. Equations (5.8) and (5.9) show that there are two real poles that begin at the origin, and two complex conjugate poles that begin at the poles of the plant. For very small c_1 the polynomial $b(s)$ reduces to $s^2 + a_1 s + c_0 a_0$, therefore two of the poles move toward a pair of zeros that resemble the plant poles but with slightly lower natural frequency and slightly higher damping ratio, while the other two poles move to asymptotes with angles $\pm\frac{\pi}{2}$ centered near the imaginary axis. For very large c_1 the polynomial $b(s)$ reduces to $s\,(s^2 + a_1 s + a_0)$, causing an approximate pole-zero cancelation and leaving $\frac{b(s)}{a(s)}$ as an integrator.

Figure 5.3 shows the block diagram of the plant in closed-loop with the PPF compensator (with simplifications (5.5) and (5.6)) along with the extremum seeking algorithm. The plant is excited by the disturbance $d(t) = a_d \sin \omega_d t$, and ES tunes $f_0(t)$, where $q_0 = (2\pi f_0)^2$, in order to minimize the nonlinear map $J(y) = \int_{t-T}^{t} y^2(\tau)\, d\tau$,

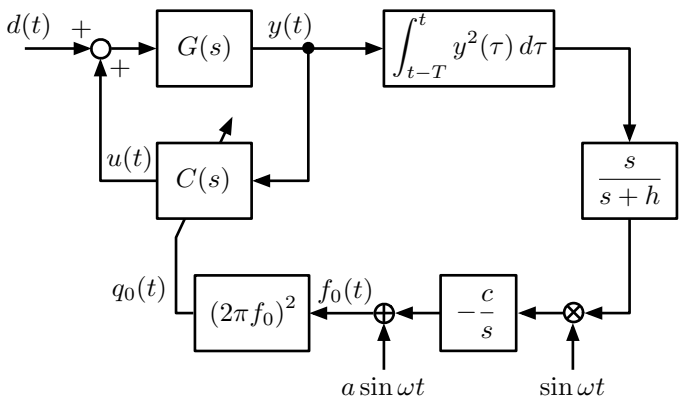

Figure 5.3: Block diagram of closed-loop system with extremum seeking tuning of the compensator parameter.

where T is size of the window used for integration. Extremum seeking perturbs $f_0(t)$ with $a\sin\omega t$. The perturbed map output is passed through a washout filter with cut-off frequency h, and then demodulated with $\sin\omega t$. Tuning is achieved by integrating the demodulated signal. The parameter c is the tuning gain. The window size T must be chosen large enough to capture a sufficient number of periods of the output, which depends on the frequency of the disturbance. The perturbation frequency ω should then be chosen slower then the period of the window, in order for the cost function not to attenuate its effects.

5.4 Simulation Results

Figure 5.4 shows simulation results. Tuning was kept off until $t = 50$. The plant parameters are $a_0 = (8\pi)^2$, $a_1 = \frac{2\sqrt{a_0}}{10}$, and $b = a_0$. The compensator constants are $c_0 = \frac{4}{5}$ and $c_1 = \frac{1}{100}$, and the compensator is initialized with $f_{0_o} = 1.5$ ($q_{0_o} = (3\pi)^2$). The closed loop system is forced by a sinusoid of amplitude $a_d = 1$, and frequency $\omega_d = \sqrt{a_0}$. The ES parameters are $T = \frac{1}{2}$, $a = 0.1$, $\omega = \pi$, $c = \frac{4}{5}$, and $h = \pi$. Figure 5.4(a) shows the cost function $J(y)$ as a function of time. Figure 5.4(b) shows the cost function as ES tunes $f_0(t)$, compared to the the dashed curve that was pre-generated by selecting values of f_0 and evaluating the corresponding $J(y)$ at steady state. Figure 5.4(c) shows the normalized plant output, and highlights

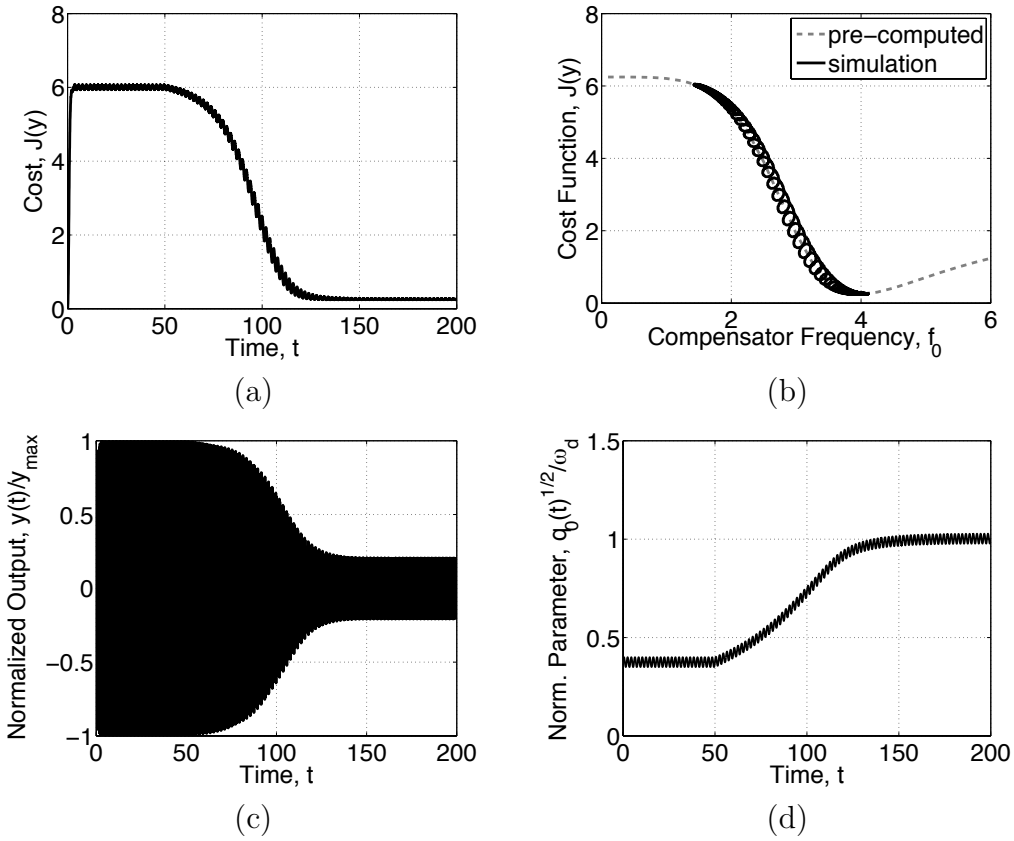

Figure 5.4: Simulation results showing the (a) evolution of the cost as a function of time, (b) evolution of the cost as a function of the compensator frequency, (c) normalized plant output, and (d) normalized compensator natural frequency.

the performance of the tuning scheme. Figure 5.4(d) plots the normalized natural frequency $\frac{\sqrt{q_0(t)}}{\omega_d}$, and shows how ES tunes the compensator natural frequency to be near that of disturbance.

5.5 Conclusions

This chapter has presented an extremum seeking based design for tuning the natural frequency of a positive position feedback (PPF) compensator to improve vibration suppression in the presence of a persistent sinusoidal disturbance. A brief discussion of positive position feedback compensators was presented, with a stability analysis of the PPF compensator applied to a second-order system. The analysis

was used to parameterize the compensator gain and damping in terms of the natural frequency of a system. Then an extremum seeking based tuning algorithm was designed to optimize the performance of the PPF compensator for a linear second-order system. The extremum seeking scheme was able to tune the compensator to suppress vibrations at the frequency of the disturbance.

6

Extremum Seeking Tuned Controllers for Generating and Tracking Sinusoids for Shake Table Control

This chapter presents the design and implementation of an extremum seeking (ES) based shake table controller when the goal is to generate and track a sinusoid of given amplitude, frequency, and phase at the output of the shake table, or at some point on a specimen mounted to the table. Assuming a stable linear plant, given a sinusoidal input its output, ignoring transients, will also be sinusoidal but possibly of different amplitude and phase. The design of the extremum seeking based motion planning and tracking controller begins by using the sinusoidal plant output to generate amplitude and relative phase (with respect to the input) estimates. Two independent ES tuning loops are then designed to adjust the amplitude and phase of the sinusoidal shake table input, based on those estimates. Simulations and experimental results are used to demonstrate the effectiveness of the controller.

6.1 Introduction

The basic principle of a shake table is to generate a desired table motion in order to study the response of a specimen mounted to it. Its fidelity is highly dependent on characteristics of the table and its actuators, the specimen, and their overall interaction. Fidelity will also depend on the amplitude and frequency content of the desired motion. A good controller must account for the overall dynamics of the shaker-specimen system, while being able to operate with a variety of specimens whose dynamics might exhibit nonlinear or time varying behavior.

Traditional shake table control strategies are based on the implementation of an inverse kinematic solver to convert desired table displacement into control signals, and a linear feedback composed of the weighted sum of the position, velocity and acceleration [86]. Transfer function based control methods [12] use an experimentally identified plant model, then pre-filter the desired table motion with the inverse transfer function and apply the resulting control signal in open-loop. A proportional-integral-derivative (PID) controller can also be used to close the loop for improved performance [12, 85]. More advanced tools, such as linear optimal control [47], employ off-line computations of an optimal control signal to compensate for shaker-specimen interactions and actuator dynamics, then use an optimal controller to match the desired table trajectory in the presence of unmodeled dynamics and noise.

In all the aforementioned cases, the controller performance is highly dependent on the availability of a good plant model, found by system identification, and performance tends to degrade when modeling errors exist. In general, the system identification process requires many off-line iterations to find a satisfactory model before testing can even begin. Even so, in some cases the controllers will not be able to compensate for strong nonlinearities or changes in the dynamics [18].

Nonlinear optimal control strategies proposed in [19] implement non-quadratic cost functions and tensor based techniques to find an optimal control signal. The Kalman filter based control technique [57] produces an open-loop optimal control signal for a nonlinear system. The nonlinear system is linearized about the open-loop trajectory, and then a compensator is designed based on linear control theory. This

method requires on-line computation of a state-dependent Riccati equation. Once again, these methods are sensitive to the quality of the plant model found by system identification. Adaptive filter compensation [23] employs iterative identification of the transfer function governing the error between a desired and actual system system output, and adaptively tunes the error transfer function to pre-filter the shake table input with the inverse of the error transfer function. The method is effective in compensating for reaction forces caused by a mildly nonlinear specimen, but its performance is sensitive to sensor noise. The minimal control synthesis [72], based on model reference adaptive control, is yet another adaptive control tool implemented on shake tables. The method treats the plant and reference model as linear systems, where the reference model is chosen to have some ideal closed-loop performance characteristics. A PID-like controller, with adaptive gains, is then applied so that the error between the plant and the reference model is minimized.

Motivation for this work comes from the experimental shake table-testbed introduced in Chapter 2. The sinusoid generating and tracking controller is based on single parameter extremum seeking, as presented in Section 5.2, used to tune the amplitude and phase of a sinusoidal input to the shaker in order to generate and track a sinusoidal reference trajectory at the output. ES is chosen because it is a non-model based approach, has low computational complexity, and is robust with respect to possible plant nonlinearities and time varying dynamics. This implementation uses one physical measurement, the testbed output chosen as the acceleration at some point along the beam, to generate amplitude and relative phase estimates. Then ES techniques are used to tune the amplitude and phase of the control signal based on those estimates. Results are investigated numerically, and experimentally.

This chapter is organized as follows. Section 6.2 presents the methods used for generating output amplitude and relative phase estimates, and the extremum seeking based controller design. Section 6.3 presents numerical and experimental results. Section 6.4 discusses attempted extensions of the designs in Section 6.2.

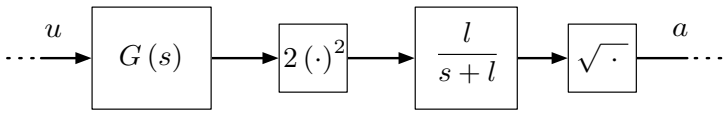

Figure 6.1: Block diagram of the method used to generate amplitude estimates.

6.2 Design

6.2.1 Generating Amplitude and Relative Phase Estimates

Figure 6.1 shows the block diagram of the method used to generate the amplitude estimate. A similar method for generating amplitude measurements is used in Chapter 6 of [2]. Consider a stable, linear plant $G(s)$ whose input u is of the form $a_i \sin(\omega t)$. The plant dynamics are unknown, but when forced by a sinusoidal input its output, ignoring transients, will also be a sinusoid $a \sin(\omega t + \phi)$ at the same frequency with some modulated amplitude a, and phase shift ϕ. The trigonometric identity

$$2(a \sin x)^2 = a^2 (1 - \cos(2x)) , \tag{6.1}$$

applied to the plant output generates a signal of the form $a^2 - a^2 \cos(2\omega t + 2\phi)$, where the non-zero-mean term a^2 contains an estimate of the output amplitude. The sinusoidal term $a^2 \cos(2\omega t + 2\phi)$ can be attenuated using a low-pass filter with roll-off frequency is $l \ll 2\omega$. Taking a square-root of the filtered signal produces the amplitude estimate a. The roll-off frequency of the low-pass filter used in estimating the output amplitude must be sufficiently small to adequately attenuate the term $a^2 \cos(2\omega t + 2\phi)$.

Figure 6.2 shows a diagram of the concept used to estimate the relative phase $\Delta\phi$ between a reference signal $\sin(\omega t + \phi_r)$ of desired phase ϕ_r, and the plant output $a \sin(\omega t + \phi)$. The relative phase between the two signals is directly proportional to the elapsed time between zero-crossings of the reference signal and plant output. A zero-crossing, in general, refers to whenever a signal changes signs whether it be increasing or decreasing. This work only considers zero-crossings in one direction, in order to estimate relative phase up to π radians. The 'start' and 'stop' signals

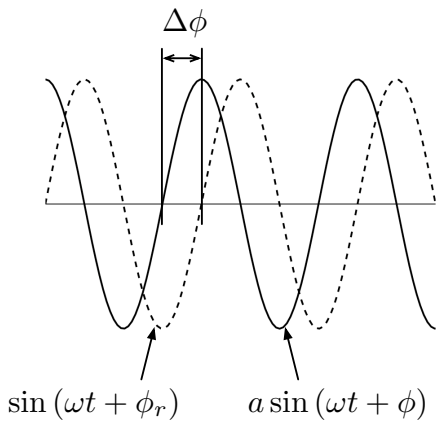

Figure 6.2: Diagram showing the concept used to generate relative phase estimates.

used to estimate the relative phase are implemented two ways. One way uses the reference signal to start, and the plant output to stop the count. The second uses the plant output to start, and the reference signal to stop the count. This generates two relative phase estimates, which can be thought of as lead and lag respectively. The smaller, in magnitude, of the two estimates is then used in the ES tuning loop. It would be sufficient to measure and tune based on one relative phase measurement, however choosing the smaller of the two forces ES to tune in the direction of least relative phase. Calibration would be necessary to relate the elapsed time measurement, given in seconds or running count, to the actual relative phase in radians, but that is not necessary for this design.

6.2.2 Extremum Seeking for Tuning Amplitude and Phase

Tuning of the amplitude and phase of a sinusoidal input, in order to track a desired sinusoid at the output, requires combining the previously discussed techniques for generating amplitude and relative phase estimates with the basic building blocks of ES—perturbation, demodulation, nonlinear map and integrator—as discussed in Section 5.2. Since only one plant output is measured and used to generate estimates for the amplitude and relative phase, then ES tuning can be done separately for the input amplitude and phase. This reduces the problem from tracking a time varying nonlinear map as a function of the desired reference trajectory, to set-point

regulation of the amplitude and relative phase using static maps.

The desired reference trajectory to be generated and tracked at the output of a stable linear plant $G(s)$ is

$$y_r = a_r \sin(\omega_r t + \phi_r) \ , \tag{6.2}$$

where a_r, ω_r and ϕ_r are the desired amplitude, frequency and phase of the reference signal. Ignoring transients, the motion planning reference solution must have the form

$$u = (a_0 + u_a) \sin(\omega_r t + u_\phi + \phi_0) \ , \tag{6.3}$$

where a_0 and ϕ_0 are constants, which could be chosen to exactly satisfy motion planning assuming perfect knowledge of the plant. The parameters u_a and u_ϕ are tuned in order to compensate for errors between the desired reference trajectory 6.2 and the actual steady state plant output

$$y = A \sin(\omega_r t + \phi) \ , \tag{6.4}$$

where A, and ϕ are the amplitude and phase of the output.

Figure 6.3 shows the block diagram of the ES based amplitude and phase tuning design. The scalar plant output (6.4) is used to generate the amplitude and relative phase estimates a and $\Delta\phi$ using the methods discussed in Section 6.2.1. These signals are perturbed with sinusoids of amplitude p_a and p_ϕ and frequencies ω_a and ω_ϕ respectively. This system does not have an implicit nonlinear map to be optimized, which allows for the choice of nonlinear maps for each tuning loop. Unlike typical applications of ES, and the general scheme discussed in Section 5.2, the maps are directly perturbed as opposed to the tuned parameters u_a and u_ϕ being perturbed. The advantage of such an implementation is that the plant will not exhibit perturbed steady-state behavior. The nonlinear maps, which take the perturbed signals a_p and ϕ_p, are chosen such that they are convex, with unique global minima. The map used in the amplitude tuning loop is shifted by the desired amplitude a_r in order to have ES tune u_a such that $a \to a_r$. The map used in the the phase tuning loop is minimized at $\Delta\phi = \phi - \phi_r \to 0$. The map outputs, J_a and J_ϕ, are demodulated by sinusoids of frequencies ω_a and ω_ϕ respectively. Those

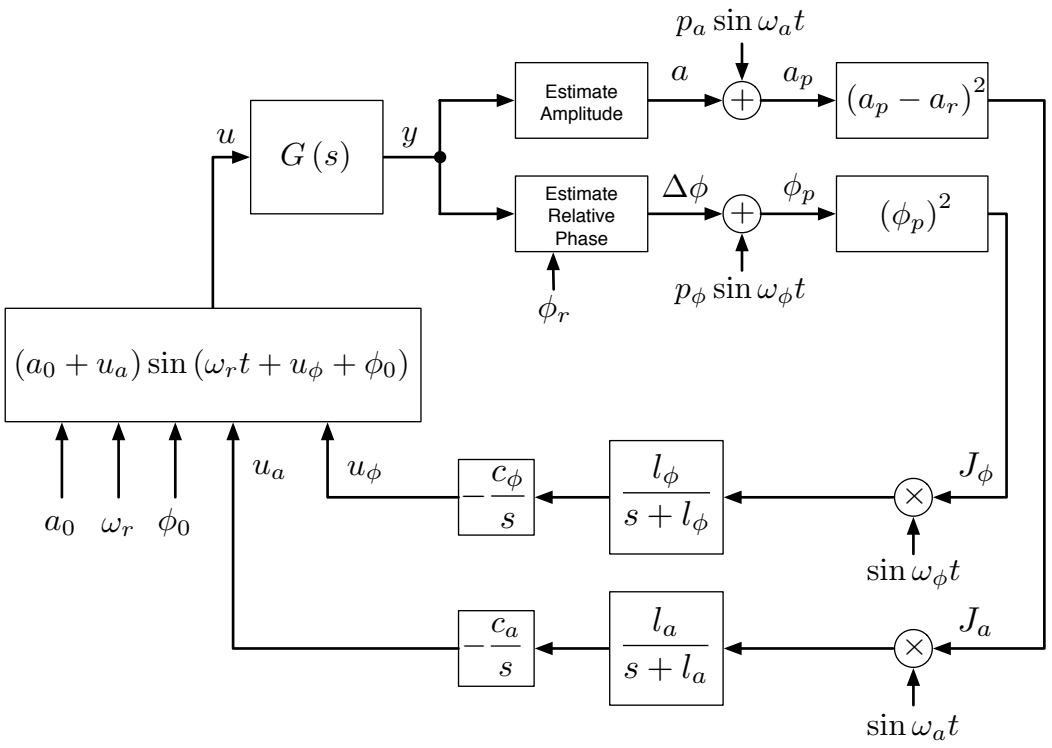

Figure 6.3: Block diagram of ES applied to tune the amplitude and phase of the input u, to track a reference trajectory at y.

signals are low-pass filtered at frequencies $l_a << \omega_a$ and $l_\phi << \omega_\phi$ to remove harmonics introduced by the perturbations, nonlinear maps and demodulation. The tuned signals, u_a and u_ϕ, are generated by passing the filtered demodulated signals through integrators with gains $c_a > 0$ and $c_\phi > 0$.

The expressions for the tuned signals, u_a and u_ϕ, are

$$u_a = -\frac{c_a}{s}\frac{l_a}{s + l_a}\left[J_a \sin \omega_a t\right] \tag{6.5}$$

$$u_\phi = -\frac{c_\phi}{s}\frac{l_\phi}{s + l_\phi}\left[J_\phi \sin \omega_\phi t\right] . \tag{6.6}$$

The control input to the plant is then (6.3), with (6.5) and (6.6). Note that the perturbations $p_a \sin \omega_a t$ and $p_\phi \sin \omega_\phi t$ do not appear additively in either of the tuned signals, and therefore do not appear in the control signal u.

6.3 Results

The ES based amplitude and phase tuning design has been applied in simulation, and experimentally on the testbed. Section 6.3.1 presents simulation results for the controller applied to a static plant. Section 6.3.2 presents experimental results for the controller applied to the testbed.

Note that while Figures 6.1 and 6.3 use first-order low-pass filters, second-order filters with damping ratios of 0.5 are used in simulation and experimentation for better attenuation. Also, while not shown in Figure 6.3, a high-pass filter is employed before demodulation in the amplitude tuning loop.

6.3.1 Simulations

Simulation results are presented for the case where no plant knowledge is assumed, hence $a_0 = \phi_0 = 0$. Without loss of complexity, a static plant $G(s) = g > 0$ is chosen, along with $a_r > 0$, $\phi_r = \pi$, and ES will have to tune u_a and u_ϕ to overcome the maximum possible amplitude and phase errors of a_r and π respectively. The parameters used in simulation are $a_r = 1$, $c_a = 2$, $c_\phi = 1.5$, $p_a = 1/7$, $p_\phi = 1/5$, $l = 0.2\pi$, $l_a = l_\phi = \pi$, $g = 1/2$, $\phi_r = \pi$ rad, $\omega_r = \pi$ rad/s, and $\omega_a = \omega_\phi = 10\pi$ rad/s.

Figure 6.4(a) compares the plant output and the desired reference trajectory. The time scale has been truncated to highlight transient performance. The plot shows how ES simultaneously tunes u_a and u_ϕ to force the plant output to grow in amplitude and shift in phase. In an implementation of traditional ES the plant output would on average look similar to that shown in Figure 6.4(a), but it would also have higher frequency content in the amplitude and phase due to the perturbations. Figure 6.4(d) shows the amplitude and phase tuning signals, u_a and u_ϕ respectively, generated by ES. Figure 6.4(c) shows the amplitude estimate a of the plant output with respect to the reference amplitude a_r. The small amplitude oscillation visible in the steady-state of a is a byproduct of the amplitude estimating scheme. A better choice of the low-pass filter pole l would help to remove those oscillations, but it would also slow the amplitude generation scheme. Figure 6.4(d) shows the relative phase estimate $\Delta\phi$. The signal is initially held at zero, since there

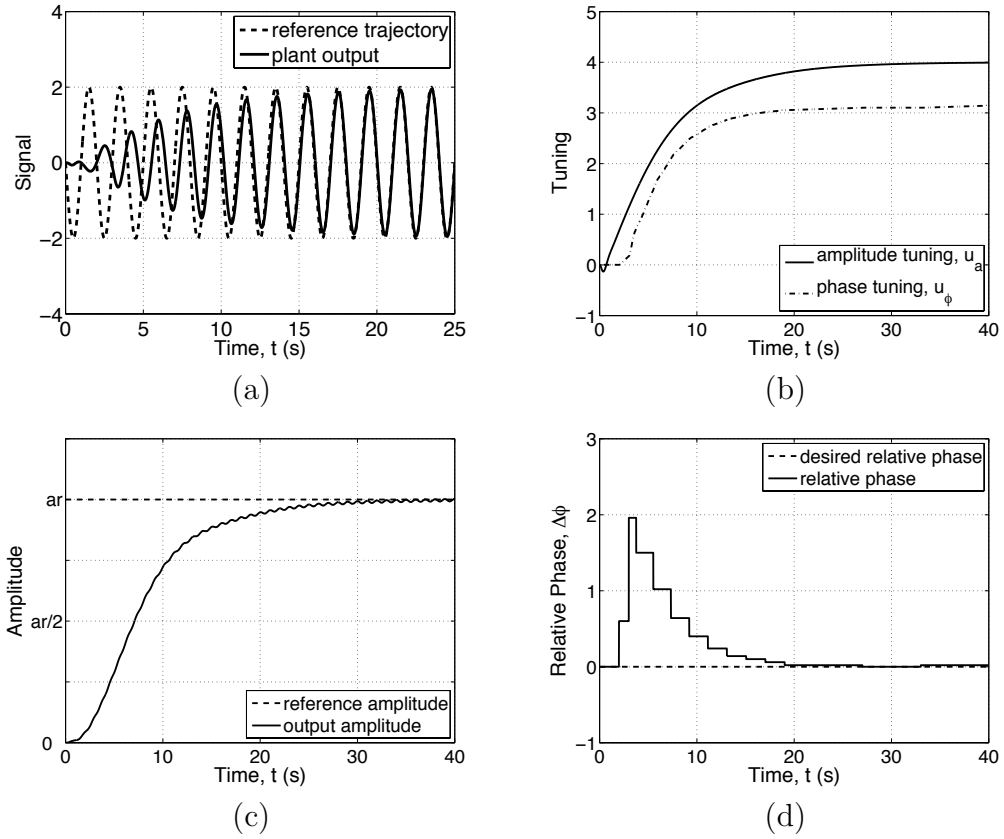

Figure 6.4: Simulation results comparing the (a) plant output and desired reference trajectory, (b) the tuned signals, (c) plant output amplitude with respect to the desired amplitude, and (d) plant output relative phase with respect to the desired relative phase.

exits a restriction that relative phase estimates cannot be generated until the plant output amplitude has grown sufficiently large. Once the measurement is generated ES tunes u_ϕ to force the relative phase to zero. The relative phase estimates have a zero-hold nature since an estimate can only be produced at the end of each timing window, which occurs once every period $T = \frac{2\pi}{\omega_r}$.

Figure 6.5 shows the map outputs J_a and J_ϕ. The time scale has been truncated to highlight their transient behavior. The effects of the perturbations can be clearly seen in the outputs of the nonlinear maps. The effects of the perturbations on the tuned signals are negated by the low-pass filters used after demodulation.

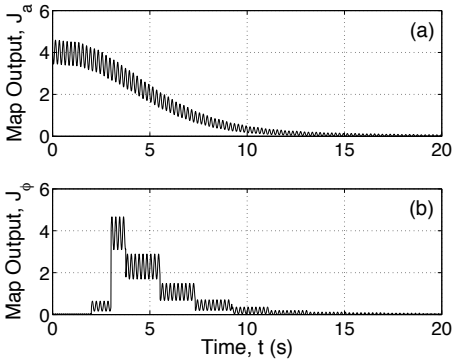

Figure 6.5: Plots showing the outputs of (a) the amplitude tuning map J_a, and (b) the phase tuning map J_ϕ.

6.3.2 Experiments

The experimental set-up is composed of the cantilevered beam testbed presented in Chapter 2. The accelerometer is mounted at the beam's free end.

Using Knowledge of the Plant

Results are presented for the case in which limited knowledge of the plant is used to initialize the input with some $a_0 > 0$ and $|\phi_0| > 0$. The parameters used in experimentation are $a_r = 0.02$ V, $c_a = 25$, $c_\phi = 15$, $p_a = 1/4$, $p_\phi = 1/5$, $l = 2\pi$, $l_a = l_\phi = 10\pi$, $\phi_r = 0$, $\omega_r = 30\pi$ rad/s, and $\omega_a = \omega_\phi = 300\pi$ rad/s.

The reference trajectory parameters are $a_r = 0.02$ V, $\omega_r = 30\pi$ rad/s, and $\phi_r = 0°$. To illustrate how some plant knowledge helps in choosing values for a_0 and ϕ_0, an experiment was first run to identify the plant's characteristics—amplitude and phase modulation—at the desired frequency. In this case, a sinusoid of unit amplitude and desired frequency was used as the input, and the corresponding output was measured for comparison. Other methods, such as experimental or analytical Bode plots or simulations, could also be used to gain some insight of the plant's amplitude and phase modulation characteristics. Figure 6.6 compares the testbed input and output (magnified ten times), for an input $u = \sin(30\pi t)$ V. The plot shows that the plant's output is attenuated about thirty times, with a relative phase modulation of approximately π rad. Based on this limited knowledge, the

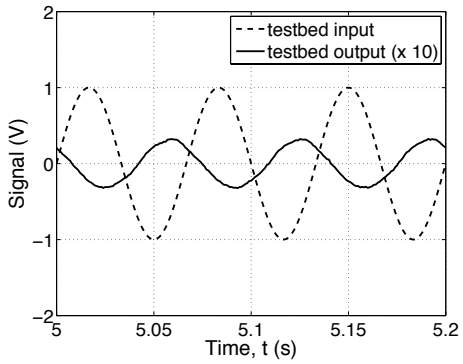

Figure 6.6: Plot comparing the testbed input, and output magnified ten times.

plant input is initialized with $a_0 = 30a_r$ V and $\phi_0 = -\pi$ rad.

Figure 6.7(a) compares the reference trajectory to the plant output, when the input is $u = a_0 \sin(\omega_r t + \phi_0)$. The comparison is being made with the amplitude and phase tuning turned off. The plot shows that the choices of a_0 and ϕ_0 help the controller begin closer to the desired trajectory. Figure 6.7(b) shows a snap-shot of the experiment after the controller has reached steady state. The plot compares the reference signal with the testbed output, and shows how ES has tuned u_a and u_ϕ such that the testbed output matches the reference signal to within the order of the sensor noise.

Modularity to Different Plants

Modularity to different plants was quantified by attaching a mass of 0.10 lb (46 g) at various locations on the cantilevered beam. Figures 6.8(a) and (b) show the output amplitude and relative phase for the comparing the nominal case of no mass, and mass placed at the tip, half-way between the tip and the shaker, and near the shaker. The figure shows how changing the plant effects the performance of the amplitude tuning controller. Performance in the "half-way" and "shaker" cases is still acceptable, while performance in the "tip" case is greatly degraded. This would be addressed by increasing the tuning gain c_a. Adding mass does not degrade performance of the phase tuning as much as it does the amplitude tuning.

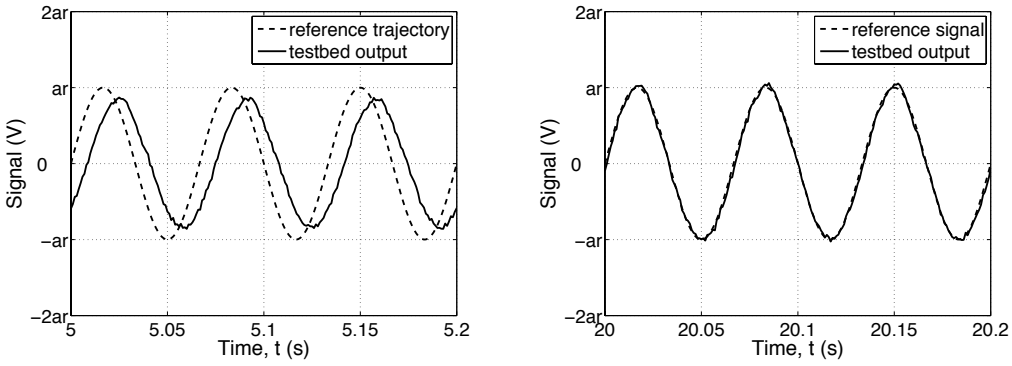

(a) (b)

Figure 6.7: Experimental results comparing the reference trajectory and testbed output, when (a) $a_0 = 0.06$ V and $\phi_0 = -\pi$ rad and tuning is turned off, and (b) when tuning is turned on.

6.4 Extending Applicability of the Scheme

Work was done to extend the motion planning and tracking results for sinusoidal reference trajectories to reference trajectories composed of a small number sinusoids with well spaced frequencies, sinusoidal reference trajectory with slowly varying frequency, for a single sinusoid when the beam tip interacts with nonlinearities, and for general reference trajectories.

Small Number of Sinusoids with Well Spaced Frequencies

This was attempted by using band-pass filters to pick-off each frequency in the plant output, then use a amplitude and relative phase estimate and tuning loop for each sinusoid. The use of the filters dictated the need for the frequency of each sinusoid to be well spaced, otherwise the signals would contaminate each other's tuning loops. The scheme worked for generating the desired amplitudes, but the relative phase estimation scheme was unable to operate properly with even the slightest cross-contamination and phase tuning could not be done.

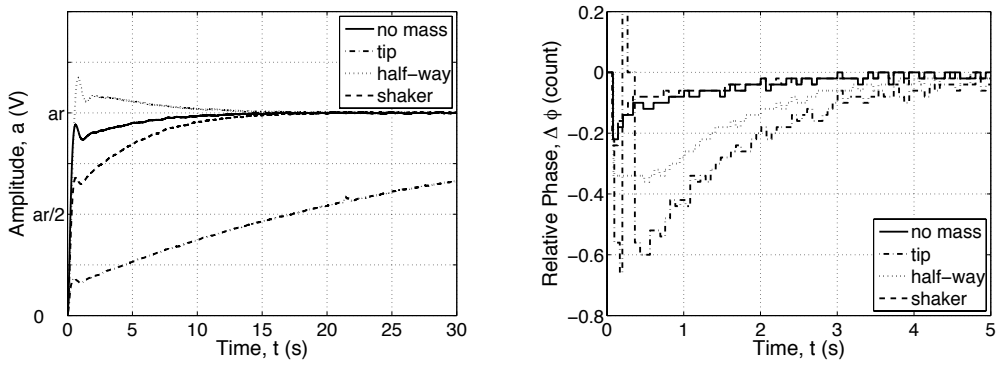

Figure 6.8: Experimental results showing (a) the plant output amplitude, and (b) the plant output relative phase, when a 0.10 lb (46 g) mass is placed at various locations along the beam.

Time Varying Frequency

Experiments were conducted for reference trajectories where the frequency ω_r is a slowly varying linear function of time. Figure 6.9 shows experimental results for frequency sweeps up and down through the first natural frequency of the testbed. Figure 6.9(a) shows how extremum seeking is able to tune the input amplitude such that the amplitude of the output stays near the reference amplitude. Figure 6.9(b) shows how extremum seeking is able to tune the input phase such that the relative phase at the output stays near zero. The amplitude and phase tuning signals essentially produce 'inverse' Bode plots.

Testbed with Nonlinearities

Experiments with a sinusoid with slowly varying frequency were also used to test the ES tuning scheme on the testbed with nonlinear interaction forces at the tip of the beam. The extremum seeking based tracking portion of the scheme performed as expected. It was able to tune the input amplitude and phase to track the desired amplitude and phase. Where the method failed was in the motion planning solution, which was chosen as a sinusoid. Strong enough interactions with the nonlinearity produced harmonics, which this scheme could not account for.

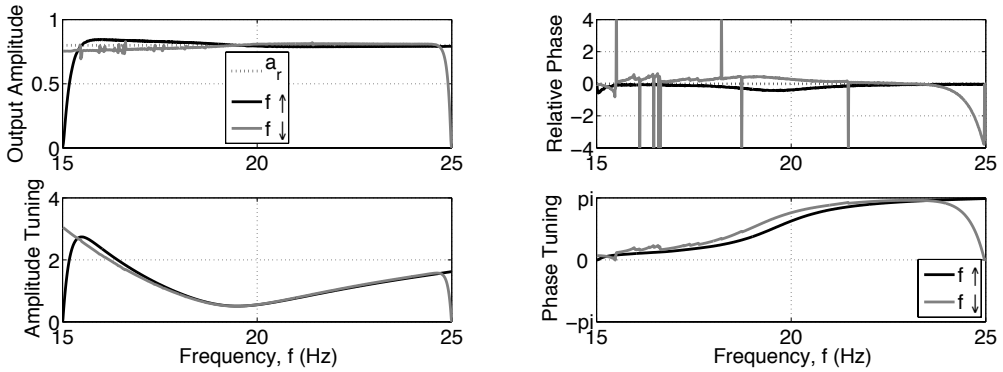

(a) (b)

Figure 6.9: Experimental results showing (a) the output amplitude estimates and amplitude tuning signals, and (b) the relative phase estimates and phase tuning signals for generating and tracking a sinusoid when the frequency is slowly swept up and down through resonance.

6.5 Conclusions

The design and implementation of an adaptive shake table controller for the generation and tracking of single sinusoids has been presented. The assumed form of a motion planning reference solution was first found. The sinusoidal plant output was used to generate amplitude and relative phase estimates. Then ES was applied to separately tune the amplitude and phase of the reference solution.

Simulation results showed good performance of the controller when applied with zero knowledge of the plant. The worst-case-scenario simulations, where the controller was initialized with zero amplitude and completely out of phase, showed how the method adaptively tuned the control input to match the reference trajectory. Experimental results showed good performance of the controller when applied with limited knowledge of the plant, and when the plant dynamics changed.

This chapter is in full an adaptation of material as it appears in: A. A. Siranosian, M. Krstic and M. Bement, "Generation and Tracking of Sinusoids for Shake Table Control via Extremum Seeking," *Proc. of the ASME International Mechanical Engineering Congress and Exposition*, 2007.

The dissertation author was the primary investigator and author of this paper.

7

Conclusions

Vibration suppression, stabilization, motion planning and tracking for flexible beams are important control problems for many practical mechanical systems. This work has approached those problems using two control design methods, backstepping for partial differential equations (PDEs), and extremum seeking.

PDE backstepping theory provides a means for finding boundary controllers for infinite dimensional systems, without discretization or truncation of the system models. Key to the success of PDE backstepping are the infinite dimensional state transformations, relating plants and their target systems. Explicit motion planning reference solutions for the string, target system and shear beam models with Kelvin-Voigt damping were found by leveraging those transformations. The displacement reference solution for the string was found using established motion planning techniques. The displacement reference solution for the target system was found using a PDE backstepping transformation relating the target system to the the string. Motion planning for the deflection angle for the shear beam was done by modifying standard PDE backstepping techniques to satisfy the deflection angle reference trajectory. Then the displacement reference solution for the shear beam was found using a PDE backstepping transformation relating the beam to the target system. PDE backstepping techniques provided a means for finding motion planning reference solutions for the shear beam, described by a PDE coupled with an ODE, using the reference solution for the much simpler string system.

A combination of PDE backstepping and gain scheduling was then used to

find nonlinear controllers to stabilize a benchmark first-order hyperbolic PDE with boundary-value-dependent in-domain nonlinearity, and the string and shear beam with Kelvin-Voigt damping and boundary-displacement dependent free-end nonlinearity. Gain scheduling combined with PDE backstepping for linear systems provides a means of nonlinear control design for infinite dimensional systems that is more simple and manageable than a full nonlinear design. The benchmark problem was used to present the design methods, and a stability analysis of the origin of the closed-loop system. String and beam simulations were used to highlight the performance of their designs, which outperformed simple linearization based controllers.

Extremum seeking based designs were presented for the tuning of compensator parameters to improve the vibration suppression characteristics of positive position feedback compensators, and for the generation and tracking of sinusoids. The tuning of positive position feedback compensators was done based on traditional single parameter extremum seeking concepts. The design was able to tune the natural frequency of the compensator to suppress vibrations of a second order system forced by a sinusoidal disturbance.

The extremum seeking based sinusoid generating and tracking controller also used single parameter extremum seeking techniques. This design relied on amplitude and relative phase estimates of the output of a stable linear system, which were used by ES to tune the amplitude and phase of a sinusoidal input. This design varied from traditional extremum seeking, in that it perturbed the amplitude and relative phase estimates as opposed to the amplitude and phase of the input signal.

Appendix A

Extremum Seeking for a Point Mass for Target Tracking Without Position Measurements

This appendix presents work done with extremum seeking for the tuning of the velocity of a two-dimensional point mass to find the maximum of a signal, which decays away from the source. This work proved to be a valuable learning experience for extremum seeking techniques.

A.1 Introduction

Recent advances in extremum seeking have been followed by several exciting applications in non-model based control and optimization [5, 59, 61, 51, 20]. However, extremum seeking has so far been developed only for plants that are open loop stable [2], with poles that are sufficiently well damped. In this paper we introduce a new idea how to extend the applicability of extremum seeking to marginally stable systems and moderately unstable systems. While the later extension is of general interest, the former comes from an application.

Control of autonomous vehicles is an immensely active area. Typically autonomous agents are allowed information sharing and are supplied with at least

their position measurements. In this paper we use extremum seeking to address a problem with complete autonomy—a vehicle, without any position or velocity information, tracks the source of a scalar valued "concentration"-type signal (for example, the concentration of a chemical agent, or the strength of an acoustic, or an electromagnetic signal). The concentration field is not known, however, it is assumed to be the strongest at the source and to decay away from it. Therefore, the non-model based extremum seeking method is appropriate to approach this problem.

The classical extremum seeking scheme is modified for the stated task by observing that the integrator, a key adaptation element, is already present in vehicle models where the primary forces or moments acting on the vehicle are those that provide thrust/propulsion, i.e., for vehicles that act primarily in the $m\ddot{\vec{x}} = F$ manner, where F is the motion-generating input and $\ddot{\vec{x}}$ is the acceleration vector. In this paper we present results for a point mass model in the plane. An extension to 3D for a fully actuated vehicle is trivial, except that one employs separate probing frequencies in the ES algorithm for the individual axes of motion. The extension to point mass models with extensive losses (due for example to drag) is straightforward by noting that the input-output relationship drops in relative degree, making the problem actually easier. Drift-inducing forces like gravity or buoyancy are automatically accommodated by extremum seeking which auto-tunes the input to compensate for such constant disturbances.

An extension to underactuated or nonholonomic vehicles is not straightforward and is the subject of [89] an our other follow up research.

The stability results we prove are local. The techniques introduced by Tan, Nesic, and Mareels [73] can be used to achieve semi-global versions of our results.

A.2 A Velocity-Actuated Point Mass (Single Integrators)

In the plane, an autonomous vehicle is modeled as a point mass:

$$\dot{x} = v_x\,, \quad \dot{y} = v_y\,, \tag{A.1}$$

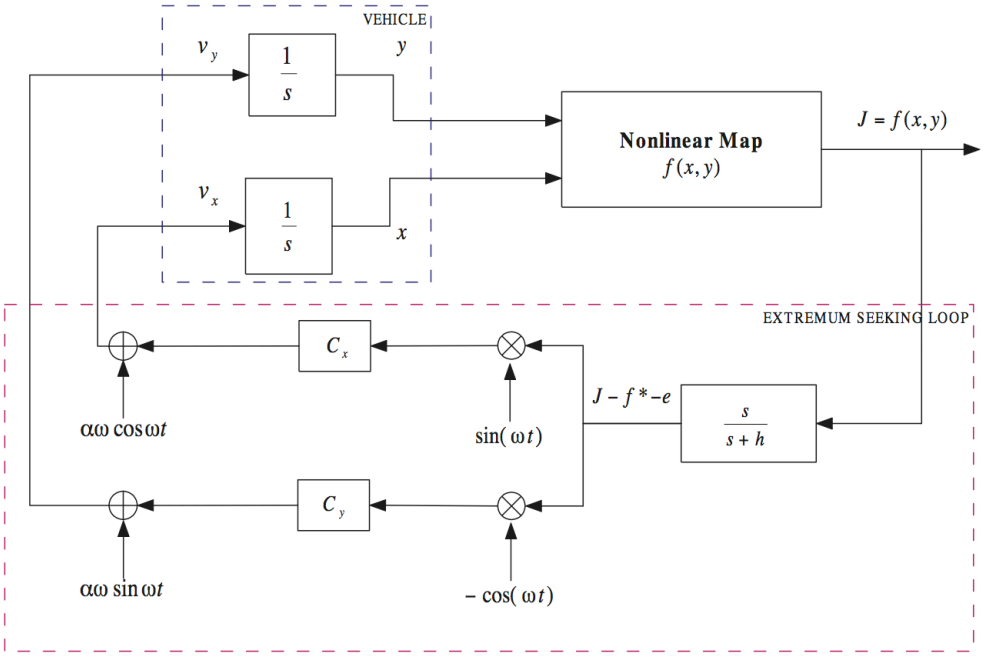

Figure A.1: Extremum seeking for velocity-actuated point mass.

where $[x, y]$ is the position of the point mass and v_x, v_y are the velocity inputs. Our method is extended later in the paper to the case where the inputs are forces, however for clarity in introducing the new concept, we consider the simplest case of a velocity-actuated point mass first.

A block diagram of extremum seeking is shown in Fig. A.1. The nonlinear map represents the distribution of the signal being tracked, whose strength will typically decay away from the origin, thus we assume that the nonlinear map $J = f(x, y)$ has a local maximum and pursue local tracking of that maximum. For clarity we assume that the nonlinear map is quadratic and that its Hessian is diagonal, viz.,

$$J = f(x, y) = f^* - q_x(x - x^*)^2 - q_y(y - y^*)^2, \tag{A.2}$$

where (x^*, y^*) is the *unknown* maximizer, $f^* = f(x^*, y^*)$ is the *unknown* maximum, and q_x, q_y are some *unknown* positive constants. General non-quadratic maps with non-diagonal Hessians are equally amenable to analysis, using the same technique as in [2, 38]. We show next that extremum seeking drives the autonomous vehicle to (x^*, y^*) without employing any knowledge of $f(x, y)$ or the measurements of

(x, y), only the measurement of the output J of the nonlinear map $f(x, y)$. This corresponds to the problem of source localization in an unknown concentration field. The designer chooses the parameters $\alpha, \omega, h, c_x, c_y$ in the block diagram (Fig. A.1), whereas the extremum seeking automatically tunes v_x, v_y to lead the vehicle to the peak of $f(x, y)$.

The analysis that follows employs the averaging method. Let

$$e = \frac{h}{s+h}[J] - f^*, \tag{A.3}$$

then the signal after the washout filter can be expressed as $\frac{s}{s+h}[J] = J - \frac{h}{s+h}[J] = J - f^* - e$. Now, let us introduce the new coordinates

$$\tilde{x} = x - x^* - \alpha \sin(\omega t), \tag{A.4}$$

$$\tilde{y} = y - y^* + \alpha \cos(\omega t). \tag{A.5}$$

Then, in the time scale $\tau = \omega t$, we define:

$$\Delta = (J - f^* - e) = -\left[q_x(\tilde{x} + \alpha \sin\tau)^2 + q_y(\tilde{y} - \alpha\cos\tau)^2 + e\right]. \tag{A.6}$$

So we summarize the system in Fig. A.1 as

$$\frac{d\tilde{x}}{d\tau} = +\frac{1}{\omega} c_x \Delta \sin\tau \tag{A.7}$$

$$\frac{d\tilde{y}}{d\tau} = -\frac{1}{\omega} c_y \Delta \cos\tau \tag{A.8}$$

$$\frac{de}{d\tau} = +\frac{h}{\omega}\Delta. \tag{A.9}$$

The system (A.7)–(A.9) is in the form to which the averaging method is applicable, provided $1/\omega$ is small, i.e., provided ω is large (relative to the other parameters in the extremum seeking scheme and relative to the parameters in the nonlinear map). The average model of (A.7)–(A.9) is

$$\frac{d\tilde{x}_{avg}}{d\tau} = -\frac{1}{\omega}\alpha c_x q_x \tilde{x}_{avg} \tag{A.10}$$

$$\frac{d\tilde{y}_{avg}}{d\tau} = -\frac{1}{\omega}\alpha c_y q_y \tilde{y}_{avg} \tag{A.11}$$

$$\frac{de_{avg}}{d\tau} = -\frac{1}{\omega} h \left[q_x \tilde{x}_{avg}^2 + q_y \tilde{y}_{avg}^2 + e_{avg} + \frac{\alpha^2}{2}(q_x + q_y)\right]. \tag{A.12}$$

Then the equilibrium of the average model (A.10)–(A.12) is

$$\tilde{x}^e_{avg} = 0, \quad \tilde{y}^e_{avg} = 0, \quad e^e_{avg} = -\frac{\alpha^2}{2}(q_x + q_y). \tag{A.13}$$

The Jacobian of (A.10)–(A.12) at $(\tilde{x}^e_{avg}, \tilde{y}^e_{avg}, e^e_{avg})$ is

$$J_{avg} = \frac{1}{\omega}\begin{bmatrix} -\alpha c_x q_x & 0 & 0 \\ 0 & -\alpha c_y q_y & 0 \\ 0 & 0 & -h \end{bmatrix}. \tag{A.14}$$

Given the knowledge that the extremum is a maximum, it follows that q_x, q_y are known to be positive, though their actual values are unknown. Therefore, if we choose $\alpha > 0, c_x > 0, c_y > 0$ and $h > 0$, the Jacobian (A.14) is Hurwitz and the equilibrium (A.10)–(A.13) of the average system (A.12) is locally exponentially stable. Then according to the averaging theorem [35], we have the following result.

Theorem A.1 *There exists $\bar{\omega}$ such that for all $\frac{1}{\omega} \in (0, \frac{1}{\bar{\omega}})$ the system in the Fig. A.1 with the nonlinear map of the form* (A.2) *has a unique exponentially stable periodic solution $(\tilde{x}^{2\pi/\omega}, \tilde{y}^{2\pi/\omega}, e^{2\pi/\omega})$ of period $\frac{2\pi}{\omega}$ and this solution satisfies*

$$\left\| \begin{bmatrix} \tilde{x}^{2\pi/\omega} \\ \tilde{y}^{2\pi/\omega} \\ e^{2\pi/\omega} + \frac{\alpha^2}{2}(q_x + q_y) \end{bmatrix} \right\| \leq O(1/\omega), \quad \forall \tau \geq 0. \tag{A.15}$$

Since $x - x^* = \tilde{x} + \alpha \sin(\omega t) = \left(\tilde{x} - \tilde{x}^{2\pi/\omega}\right) + \left(\tilde{x}^{2\pi/\omega} - 0\right) + \alpha \sin \tau$, the theorem implies that the first term converges to zero, the second term is $O(1/\omega)$, and the third term is $O(\alpha)$. Thus $\limsup_{\tau\to\infty} |x - x^*| = O(\alpha + 1/\omega)$. Similiary, we can obtain $\limsup_{\tau\to\infty} |y - y^*| = O(\alpha + 1/\omega)$. Hence, we get

$$\limsup_{\tau\to\infty} |f - f^*| = O\left(\alpha^2 + (1/\omega)^2\right), \tag{A.16}$$

which characterizes the asymptotic performance of the extremum seeking loop in Fig. A.1. Since we choose α as small and ω as large, the tracking error is very small.

Extremum seeking can be used for tracking of slowly varying trajectories, i.e., for tracking moving signal sources. When the trajectories are periodic our stability proof extends with very minor modifications which we don't present here in the

interest of space. For example, consider a target motion is in the shape of the number eight (8),

$$x^* = a_m \sin(\omega_m t) \tag{A.17}$$

$$y^* = a_m \cos(2\omega_m t + \phi_m)\,, \tag{A.18}$$

where $\omega_m \ll \omega$. If ω and ω_m are commensurate, i.e., if there exist natural numbers N and N_m such that $\omega/\omega_m = N/N_m$, then our proof extends, with averaging applied over a period of $2\pi N$ in the τ-time scale to account for the presence of an additional periodic terms on the right hand sides of (A.7) and (A.8). If, however, ω and ω_m are incommensurate (for example, $\omega = 4\pi\omega_m$ or $\omega = 3\sqrt{23}\omega_m$), the technique of general averaging for 'almost periodic' systems [35, Section 10.6] leads to the same stability conclusions.

We first illustrate the simulation results of seeking a stationary target. The point mass model (A.1) and the quadratic map (A.2) are used in the simulation. We set the parameters of the target as $(x^*, y^*) = (-1, -1), f^* = 1, q_x = 1$ and $q_y = 0.5$. The parameters of the extremum seeking loop are chosen as $\omega = 30, \alpha = 0.08, c_x = c_y = 10$ and $h = 1$. The starting position of the autonomous vehicle is $(x(0), y(0)) = (1, 1)$. As shown in Fig. A.2 (b), the autonomous vehicle starts at $(1, 1)$ by probing around to climb the gradient of the unknown map, eventually circling very closely around the maximizer $(-1, -1)$, the output of the unknown signal J is shown in Fig. A.2 (a), while the control inputs are shown in Fig. A.2 (c) and (d). Note that the simulation results given in Fig. A.2 are not for parameter values that are tuned to exhibit the best possible results. On the contrary, they illustrate the performance one would achieve for particularly poorly chosen parameter of the extremum seeking scheme. The point of showing the "worst case" performance is because the map being optimized is unknown, therefore it makes sense to ask a question about the performance with poorly chosen parameters.

For the slow time varying target (A.17)–(A.18), the simulation results are shown in Fig. A.3, where we let $a_m = 1, \omega_m = 0.1, \phi_m = 3, f^* = 1, q_x = 1, q_y = 0.5$, and $\omega = 30, \alpha = 0.05, c_x = c_y = 15, h = 1$. The starting position of the autonomous vehicle is still $(x(0), y(0)) = (1, 1)$. The autonomous vehicle catches up with the target and then follows it quite closely in its number eight motion.

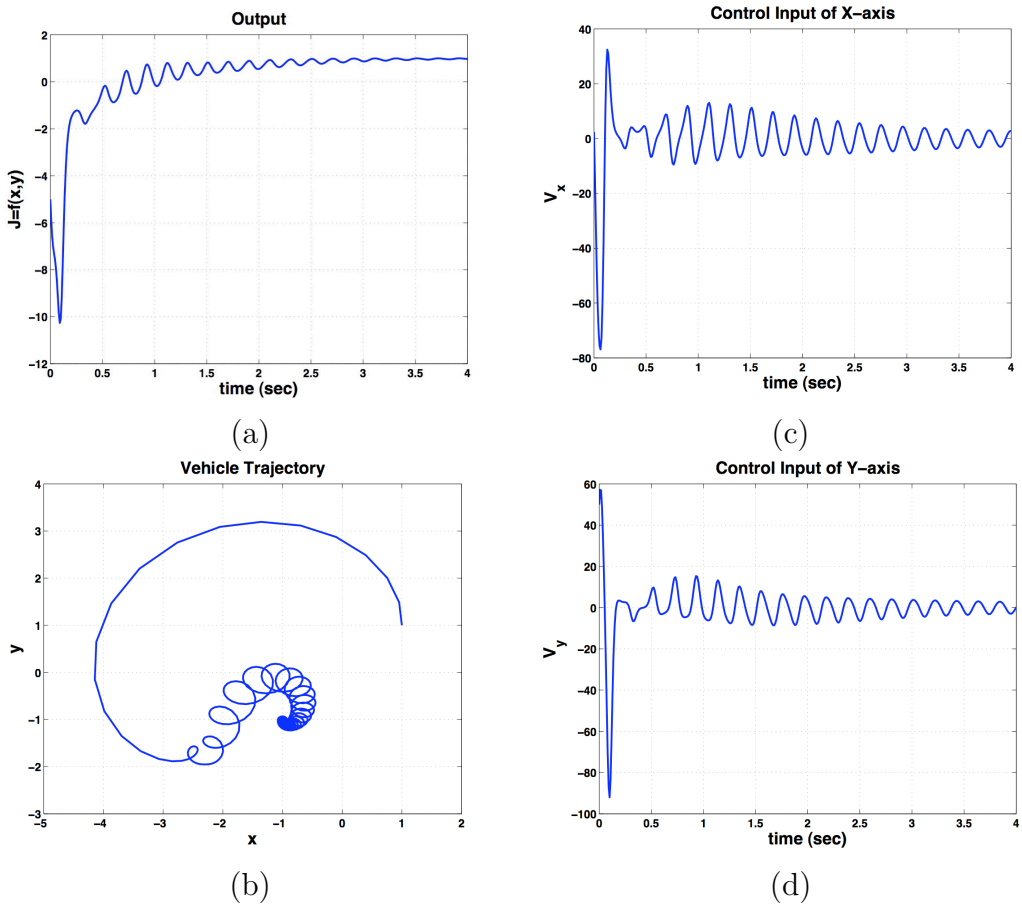

Figure A.2: Extremum seeking for velocity-actuated point mass, stationary case. (a) output; (b) vehicle trajectory starts from (1,1); (c) control input of x-axis; (d) control input of y-axis.

This appendix contains a partial reprint of material as it appears in: C. Zhang, A. A. Siranosian, and M. Krstic, "Extremum Seeking for Moderately Unstable Systems and for Autonomous Vehicle Target Tracking Without Position Measurements," *Automatica*, vol. 43, pp. 1832-1839, 2007.

The dissertation author was the primary investigator of the excerpts from this paper.

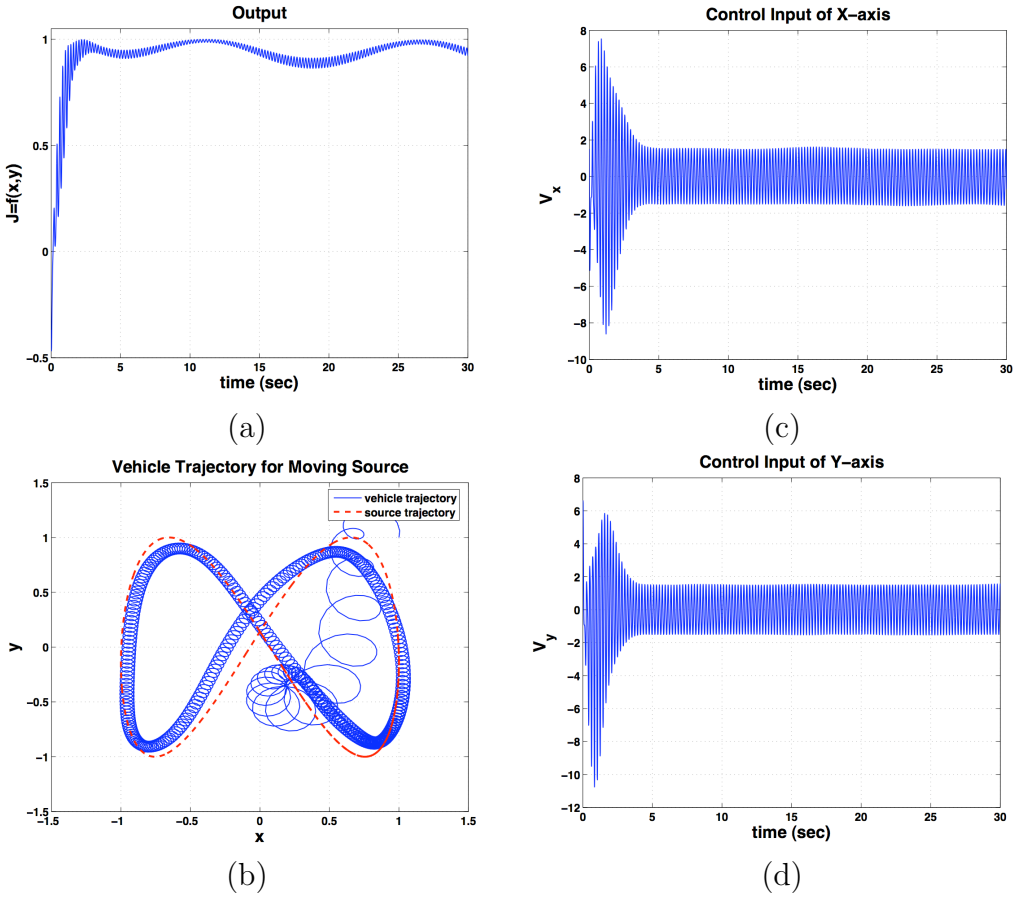

Figure A.3: Extremum seeking for velocity-actuated point mass, slowly time-varying case. (a) output; (b) vehicle trajectory starts from (1,1) and source trajectory starts from (0,0); (c) control input of x-axis; (d) control input of y-axis.

Appendix B

Experimental Vibration Suppression Results

This Appendix presents work done for virtual vibration absorbers (VVAs) with extremum seeking tuned parameters, for suppressing vibrations on the testbed. Experiments were conducted for the testbed without nonlinearities, with no mass, magnets, and steel plates attached to the tip of the beam. They were then conducted for the testbed with locally hardening and softening nonlinearities (magnets or steel plates attached to the free-end, and magnets attached arranged around the free-end of the beam).

Since the goal of this work was to implement a vibration suppression controller on the testbed, the focus of this Appendix is the performance of the controllers as opposed to the ES scheme and its performance.

B.1 Introduction

Vibration absorbers, ex. [29, 22, 33, 87], can be either passive mechanical elements—spring-mass-damper—attached to a system, or active systems (virtual vibration absorbers)—compensators emulating the passive system. Conceptually, a vibration absorber reduces vibrations of a mechanical system it is attached to by resonating near the frequency to be suppressed. Whether passive or active, vibration absorbers

have traditionally been implemented as collocated controllers, where the absorber is used to suppress vibrations at the same location it is attached to. A virtual vibration absorber (VVA) was chosen for this application since it has exhibited satisfactory performance in application, and is readily applicable to systems with acceleration feedback. While a VVA might be sufficient to damp oscillations on both the linear and nonlinear testbed, polynomial weighting (PW) of the testbed output will be used in an attempt to improve performance when applied to the nonlinear testbed.

Extremum seeking was chosen to try to iteratively tune the VVA and PW parameters based on its successful application in [36], and because it could be used to tune the compensator parameters for noncollocated applications where the shaker on the testbed would act like a VVA to reduce vibrations anywhere along the beam.

B.2 The Virtual Vibration Absorber and Polynomial Weighting

The form of the VVA compensator using acceleration feedback, for the testbed without nonlinearities, is [6]

$$C_{vva}(s) = \frac{U(s)}{Y(s)} = m_a \frac{2\zeta\omega_n s + \omega_n^2}{s^2 + 2\zeta\omega_n s + \omega_n^2}\,, \tag{B.1}$$

where $Y(s)$ is the testbed output, $U(s)$ is the control signal, and m_a represents the mass, ζ the damping ratio, and ω_n is the natural frequency of the virtual spring-mass-damper system. When applied to the nonlinear testbed the form of the controller $u(t)$ with PW is

$$u(t) = C_{vva}(s)\left[w_1 y(t) + w_2 y^2(t) + w_3 y^3(t)\right]\,. \tag{B.2}$$

Iterative extremum seeking, which is similar to ES discussed in Chapter 5 in that the it uses sinusoidal perturbation to probe a nonlinear map and an integrator to tune a parameter based on a demodulated map output, will be used to tune m_a, ζ and ω_n and w_1, w_2, w_3. Unlike the tuning schemes in Chapter 5 this implementation works iteratively to tune the parameters. First, an iteration of vibration suppression experiments—consisting of deflecting and holding the tip of the beam away from

Table B.1: Experimental results showing the (a) VVA parameters, and (b) two-percent settling time for the linear testbeds.

	No Mass	Magnets	Steel Plates
m_a	0.735	1.08	1.81
ζ	0.2	0.3	0.35
ω_n	111.37	63.12	59.62

(a)

	Settling Time, $t_{2\%}$ (s)		
	No Mass	Magnets	Steel Plates
disconnected	7.130 ± 0.250	11.920 ± 1.202	16.290 ± 1.629
passive	0.492 ± 0.014	2.407 ± 0.151	2.620 ± 0.169
C_{vva}	0.368 ± 0.011	0.944 ± 0.036	1.251 ± 0.072

(b)

equilibrium, then releasing it and collecting the data from the accelerometer—were conducted. Then an iteration of ES was completed, which consisted of computing the two-percent settling time (cost function), demodulating the cost function, implementing a discrete time integrator, and perturbing the parameter. This process was repeated until parameter convergence was achieved. Details of iterative/discrete ES can be found in [3, 36].

B.3 Experimental Results

Experiments were first conducted for the testbed without nonlinearities. The VVA damping ratio and mass were initialized as $\zeta = 0.5$, and $m_a = 3$ (the mass is dimensionless since the accelerometer voltage signal was used). The natural frequency, initialized near the first mode of the testbed, was chosen as $\omega_n = \{130\,, 70\,, 30\}$ rad/s for the testbed without mass attached, with magnets attached at the free-end, and with steel plates attached at the free-end. Table B.1(a) tabulates the parameters found for each testbed set-up, and highlights the performance of the tuned VVA. The ES tuning did not perform as expected—the first step of tuning produced large jumps in the mass and damping ratio (which would saturate a lower bound), then little tuning afterwards—however the method did manage to find sets of parame-

Table B.2: Results for (a) the polynomial weighting coefficients, and (b) two-percent settling times for the nonlinear testbeds.

	hardening	softening
w_1	0.823	0.860
w_2	2.656	3.777
w_3	3983	3553

(a)

	Settling Time, $t_{2\%}$ (s)	
	hardening	softening
disconnected	18.017 ± 1.802	14.640 ± 2.235
passive	3.013 ± 0.117	2.780 ± 0.132
C_{vva}	1.016 ± 0.022	1.268 ± 0.053
C_{vva} w/ PW	0.780 ± 0.028	1.060 ± 0.011

(b)

ters that perform well. Table B.1(b) highlights the performance of the tuned VVA, comparing its performance to the cases where the shaker was disconnected, and the shaker was connected and used a passive vibration absorber. Three experiments were conducted per iteration, therefore the values are presented as the mean plus or minus one standard deviation.

Next, the parameter values in Table B.1(a) were used for the VVA portion of the nonlinear controller (B.2), and ES tuned only the PW parameters for the testbed with hardening and softening set-ups (as described in Section 2.2.4). The PW parameters were were initialized as a linear controller, i.e. $w_1 = 1$ and $w_2 = w_3 \approx 0$. ES tuning performed well, and found combinations of the parameters which reduced the settling times for both the hardening and softening testbeds. Table B.2(a) shows the parameters found by ES. The accelerometer output voltage $y(t)$ was on the order of tenths, therefore in terms of orders of magnitude of $y(t)$, $y^2(t)$ and $y^3(t)$, w_1 and w_2 tend to be comparable, and w_3 an order of magnitude above them. This is expected with the magnets behaving as cubic nonlinearities. Table B.2(b) highlights the performance of the VVA with tuned PW, comparing its performance for each set-up to the cases with the shaker disconnected, the shaker used as a passive damper, and the VVA without PW.

Bibliography

[1] Y. Aoustin, M. Fliess, H. Mounier, P. Rouchon, and J. Rudolph, "Theory and practice in the motion planning and control of a flexible robot arm using Mikusiński operators," *Symposium on Robot Control, SYROCO97*, vol. 2, pp. 287–294, 1997.

[2] K. B. Ariyur and M. Krstic, *Real-Time Optimization by Extremum-Seeking Control*. Hoboken, NJ: Wiley-Interscience, 2003.

[3] ——, *Real-Time Optimization by Extremum-Seeking Control*. Hoboken, NJ: Wiley-Interscience, 2003.

[4] A. S. Banach and W. T. Baumann, "Gain-scheduled control of nonlinear partial differential equations," *Proceedings of the Conference on Decision and Control*, pp. 387–392, 1990.

[5] A. Banaszuk, S. Narayanan, and Y. Zhang, "Adaptive control of flow separation in a planar diffuser," *41st Aerospace Sciences Meeting & Exhibit*, 2003, paper AIAA-2003-0617.

[6] M. Bement, 2007, personal communications.

[7] D. Boskovic and M. Krstic, "Nonlinear stabilization of a thermal convection loop by state feedback," *Automatica*, vol. 37, pp. 2033–2040, 2001.

[8] ——, "Backstepping control of chemical tubular reactors," *Computers and Chemical Engineering*, vol. 26, pp. 1077–1085, 2002.

[9] ——, "Stabilization of a solid propellant rocket instability by state feedback," *Int. Journal of Robust and Nonlinear Control*, vol. 13, pp. 483–495, 2003.

[10] H. Canbolat, D. Dawson, and S. Nagarkatti, "Boundary control of a flexible cable with actuator dynamics," *Proceedings of the American Control Conference*, pp. 3547–3551, 1997.

[11] H. Canbolat, D. Dawson, C. Rahn, and P. Vedagarbha, "Boundary control of a cantilevered flexible beam with point-mass dynamics at the free end," *Proceedings of the ASME Adaptive Structures Forum*, pp. 1589–1598, 1997.

[12] P. G. Carydis, H. P. Mouzakis, E. A. Vougioukas, C. A. Taylor, and A. J. Crewe, "Comparative shaking table studies at the national technical university of Athens and at Bristol university," *Proc. 10th European Conf. on Earthquake Engineering*, pp. 2993–2997, 1994.

[13] T. H. Chen and C. M. Liaw, "Vibration acceleration control of an inverter-fed electrodynamic shaker," *IEEE/ASME Transactions on Mechatronics*, vol. 4, no. 1, pp. 60–70, 1999.

[14] P. D. Christofides, *Nonlinear and Robust Control of PDE Systems: Methods and Applications to Transport-Reaction Processes*. Boston, MA: Birkhäuser, 2001.

[15] J. R. Cloutier, "State-depedent Riccati equation techniques: An overview," *Proceedings of the American Control Conference*, pp. 932–936, 1997.

[16] J. R. Cloutier and D. T. Stansbery, "Control of a continuously stirred tank reactor using an asymmetric solution of the state-dependent Riccati equation," *Proceedings of the IEEE International Conference on Control Applications*, pp. 893–898, 1999.

[17] ——, "The capabilities and art of state-dependent Riccati equation-based design," *Proceedings of the American Control Conference*, pp. 86–91, 2002.

[18] A. J. Crewe and R. Severn, "The European collaborative programme on evaluating the performance of shaking tables," *Phil. Trans. Roy. Soc. London*, vol. 359, pp. 1671–1696, 2001.

[19] H. Dai, M. K. Sain, and B. F. Spencer Jr., "Using tensors to track earthquakes on hydraulic shaker tables," *Proc. American Control Conference*, vol. 1, pp. 1–5, 1997.

[20] M. S. de Queiroz, D. M. Dawson, S. P. Nagarkatti, and F. Zhang, *Lyapunov-Based Control of Mechanical Systems*. Birkhauser, 2000.

[21] M. S. de Queiroz and C. D. Rahn, "Boundary control and noise in distributed parameter systems: An overview," *Mechanical Systems and Signal Processing*, vol. 16, pp. 19–38, 2002.

[22] J. P. Den Hartog, *Mechanical Vibrations*, 3rd ed. McGraw-Hill, 1947.

[23] Y. Dozono, T. Horiuchi, H. Katsumata, and T. Konno, "Shaking-table control by real-time compensation of the reaction force caused by a non-linear specimen," *Journal of Pressure Vessel Tech.*, vol. 126, no. 1, pp. 122–127, 2004.

[24] F. Dubois, N. Petit, and P. Rouchon, "Motion planning and nonlinear simulations for a tank containing fluid," *Proceedings of the* 5^{th} *European Control Conference*, 1999.

[25] J. L. Fanson and T. K. Caughey, "Positive position feedback control for large space structures," *AIAA Journal*, vol. 28, no. 4, pp. 717–724, 1990.

[26] R. S. Figliola and D. E. Beasley, *Theory and Design for Mechanical Measurements*, 3rd ed. Wiley, 2000.

[27] M. Fliess, H. Mounier, P. Rouchon, and J. Rudolph, "Controllability and motion planning for linear delay systems with an application to a flexible rod," *Proc. of the* 34^{th} *IEEE Conf. on Decision & Control*, pp. 2046–2051, 1995.

[28] ——, "A distributed parameter approach to the control of a tubular reactor: a multi-variable case," *Proceedings of the* 37^{th} *IEEE Conference on Decision & Control*, pp. 439–442, 1998.

[29] H. Frahm, *Device for Damping Vibration of Bodies*, 1911, US Patent No. 525,455.

[30] M. I. Friswell and D. J. Inman, "The relationship between positive position feedback and output feedback controllers," *Smart Mater. Struct.*, vol. 8, pp. 285–291, 1999.

[31] C. J. Goh and T. K. Caughey, "On the stability problem caused by finite actuator dynamics in the collocated control of large space structures," *Int. J. Control*, vol. 41, no. 3, pp. 787–802, 1985.

[32] S. M. Han, H. Benaroya, and T. Wei, "Dynamics of transversely vibrating beams using four engineering theories," *Journal of Sound and Vibration*, vol. 225, pp. 935–988, 1999.

[33] S.-J. Huang and R.-J. Lian, "A dynamic absorber with active vibration control," *Journal of Sound and Vibration*, vol. 178, no. 3, pp. 323–335, 1994.

[34] Keyence Corporation, *LC-2400 Series ultra high accuracy laser displacement meter instruction manual*.

[35] H. K. Khalil, *Nonlinear Systems*, 3rd ed. Upper Saddle Rive, NJ: Prentice Hall, 2002.

[36] N. J. Killingsworth and M. Krstic, "PID tuning using extremum seeking," *IEEE Control Systems Magazine*, vol. 26, pp. 70–79, 2006.

[37] S. Krasheninnikov, 2006, personal communications.

[38] M. Krstic and H.-H. Wang, "Design and stability analysis of extremum seeking feedback for general nonlinear systems," *Automatica*, vol. 36, no. 2, pp. 595–601, 2000.

[39] M. Krstic and A. Balogh, "Backstepping boundary controller and observer for the undamped shear beam," 17^{th} *International Symposium on Mathematical Theory of Networks and Systems*, 2006.

[40] M. Krstic, B.-Z. Guo, A. Balogh, and A. Smyshlyaev, "Control of a tip-force destabilized shear beam by observer-based boundary feedback," *SIAM Journal on Control and Optimization*, vol. 47, pp. 553–574, 2008.

[41] ——, "Output-feedback stabilization of an unstable wave equation," *Automatica*, vol. 44, pp. 63–74, 2008.

[42] M. Krstic, A. A. Siranosian, A. Balogh, and B.-Z. Guo, "Control of strings and flexible beams by backstepping boundary control," *Proceedings of the American Control Conference*, 2007.

[43] M. Krstic, A. A. Siranosian, and A. Smyshlyaev, "Backstepping boundary controllers and observers for the slender Timoshenko beam: Part I—Design," *Proceedings of the American Control Conference*, 2006.

[44] M. Krstic, A. A. Siranosian, A. Smyshlyaev, and M. Bement, "Backstepping boundary controllers and observers for the slender Timoshenko beam: Part II—Stability and simulations," *Proceedings of the IEEE Conference on Decision and Control*, 2006.

[45] M. Krstic and A. Smyshlyaev, "Backstepping boundary control for first-order hyperbolic PDEs and application to systems with actuator and sensor delays," *Systems & Control Letters*, vol. 57, pp. 750–758, 2008.

[46] ——, *Boundary Control of PDEs: A Course on Backstepping Designs*. Philadelphia, PA: SIAM, 2008.

[47] J. Kuehn, D. Epp, and D. Patten, "High-fidelity control of a seismic shaker table," *Earthquake Eng. and Struct. Dyn.*, vol. 28, pp. 1235–12 544, 1999.

[48] A. Kugi, D. Thull, and K. Kuhnen, "An infinite-dimensional control concept for piezoelectric structures with complex hysteresis," *Structural Control and Health Monitoring*, vol. 13, pp. 1099–1119, 2006.

[49] Labworks Inc., *Model ET-132-2 & 203 Electrodynamic Shaker Operation and Installation*, revision 2.

[50] B. Laroche, P. Martin, and P. Rouchon, "Motion planning for a class of partial differential equations with boundary control," *Proceedings on the* 37^{th} *IEEE Conference on Decision & Control*, 1998.

[51] Y. Li, M. A. Rotea, G. T.-C. Chiu, G. Mongeau, and I.-S. Paek, "Extremum seeking control of a tunable thermoacoustic cooler," *IEEE Transactions on Control Systems Technology*, vol. 13, pp. 527–536, 2005.

[52] Z. H. Luo, B.-Z. Guo, and O. Morgul, *Stability and Stabilization of Infinite Dimensional Systems with Applications*. Springer Verlag, 1999.

[53] N. Lus, 2006, personal communications.

[54] T. Meurer and M. Zeitz, "Feedforward and feedback tracking control of nonlinear diffusion-convection-reaction systems using summability methods," *Industrial & Engineering Chemical Research*, vol. 44, pp. 2532–2548, 2005.

[55] H. Mounier, J. Rudolph, M. Fliess, and P. Rouchon, "Tracking control of a vibrating string with an interior mass viewed as a delay system," *ESAIM: Control, Optimisation and Calculus of Variations*, vol. 3, pp. 315–321, 1998.

[56] R. M. Murray, "Trajectory generation for a towed cable system using differential flatness," *IFAC World Congress*, 1996.

[57] D. P. Newell, H. Dai, M. K. Sain, P. Quast, and B. F. Spencer Jr., "Nonlinear modeling and control of a hydraulic seismic simulator," *Proc. American Control Conference*, vol. 1, pp. 801–805, 1995.

[58] E. Oberg, F. D. Jones, H. L. Horton, and H. H. Ryffel, *Machinery's Handbook*, 25th ed. Industrial Press, 1996.

[59] K. Peterson and A. Stefanopoulou, "Extremum seeking control for soft landing of an electromechanical valve actuator," *Automatica*, vol. 40, no. 6, pp. 1063–1069, 2004.

[60] N. Petit and P. Rouchon, "Flatness of heavy chain systems," *SIAM Journal on Control and Optimization*, vol. 40, pp. 475–495, 1998.

[61] D. Popovic, M. Jankovic, S. Manger, and A. R. Teel, "Extremum seeking methods for optimization of variable cam timing engine operation," *Proc. of the American Control Conference*, pp. 3136–3141, 2003.

[62] P. Rouchon, "Motion planning, equivalence, infinite dimensional systems," *Journal of Applied Mathematics and Computer Science*, vol. 11, no. 1, 2001.

[63] W. J. Rugh, "Analytical framework for gain scheduling," *Proceedings of the American Control Conference*, pp. 79–84, 1990.

[64] W. J. Rugh and J. S. Shamma, "Research on gain scheduling," *Automatica*, vol. 36, pp. 1401–1425, 2000.

[65] J. S. Shamma and J. R. Cloutier, "Existence of SDRE stabilizing feedback," *IEEE Transactions on Automatic Control*, vol. 48, pp. 513–517, 2003.

[66] J. S. Shamma and M. Athans, "Analysis of gain scheduled control for nonlinear plants," *Transactions on Automatic Control*, vol. 35, no. 8, pp. 898–907, 1990.

[67] ——, "Gain scheduling: Potential hazards and possible remedies," *Proceedings of the American Control Conference*, pp. 101–107, 1991.

[68] ——, "Guaranteed properties of gain scheduled control for linear parameter-varying plants," *Automatica*, vol. 27, no. 3, pp. 559–564, 1991.

[69] A. A. Siranosian, M. Krstic, A. Smyshlyaev, and M. Bement, "Motion planning and tracking for tip displacement and deflection angle for flexible beams," *Proceedings of the American Control Conference*, 2008.

[70] ——, "Motion planning and tracking for tip displacement and deflection angle for flexible beams," *ASME Journal of Dynamic Systems, Measurement and Control*, to appear.

[71] V. A. Spector and H. Flasher, "Modeling and design implications of non-collocated control in flexible systems," *ASME J. Dynamic Systems, Measurement and Control*, vol. 112, pp. 186–193, 1990.

[72] D. Stoten and E. G. Gomez, "Adaptive control of shaking tables using the minimal control synthesis algorithm," *Phil. Trans. R. Soc. London*, vol. 359, pp. 1697–1723, 2001.

[73] Y. Tan, D. Nesic, and I. Mareels, "On non-local stability properties of extremum seeking control," *Proc. of the 16th IFAC World Congress*, 2005.

[74] S. W. Taylor and S. C. B. Yau, "Boundary control of a rotating Timoshenko beam," *ANZIAM Journal*, vol. 44, pp. E143–E184, 2003.

[75] F. E. Udwadia, "Noncollocated point control of nondispersive distributed-parameter systems using time delays," *Applied Mathematics and Computation*, vol. 42, pp. 23–63, 1991.

[76] ——, "Boundary control, quiet boundaries, super-stability and super-instability," *App. Math. and Computation*, vol. 164, pp. 327–349, 2005.

[77] R. Vazquez and M. Krstic, "Control of 1-D parabolic PDEs with Volterra nonlinearities—Part I: Design," *Automatica*, vol. 44, pp. 2778–2790, 2008.

[78] ——, "Control of 1-D parabolic PDEs with Volterra nonlinearities—Part II: Analysis," *Automatica*, vol. 44, pp. 2791–2803, 2008.

[79] `http://www.labworks-inc.com`, *Labworks PA-119 linear power amplifier data sheet.*

[80] `http://www.ni.com`, *National Instruments model SC-2345 signal conditioning and data acquisition system.*

[81] `http://www.pcb.com`, *PCB Piezotronics model 352C22 accelerometer data sheet.*

[82] J. Wang and W. J.Rugh, "Feedback linearization families for nonlinear systems," *IEEE Trans. on Automatic Control*, vol. 32, no. 10, pp. 935–940, 1987.

[83] ——, "Parameterized linear systems and linearization families for nonlinear systems," *IEEE Trans. on Circuits and Sys.*, vol. 34, no. 6, pp. 650–657, 1987.

[84] L. Wang, "Positive position feedback based vibration attenuation for a flexible aerospace structure using multiple piezoelectric actuators," *Digital Avionic Systems Conf.*, vol. 2, pp. 7.C.1–10, 2003.

[85] M. L. Wang, "Closed-loop random vibration control of a shaker table with a microcomputer," *Soil Dyn. and Earthquake Eng.*, vol. 13, pp. 259–266, 1994.

[86] M. S. Williams and A. Blakeborough, "Laboratory testing of structures under dynamic loads: an introductory review," *Phil. Trans. Soc. London*, vol. 359, pp. 1651–1669, 2001.

[87] S.-T. Wu, J.-Y. Chen, Y.-C. Yeh, and Y.-Y. Chiu, "An active vibration absorber for a flexible plate boundary-Controlled by a linear motor," *Journal of Sound and Vibration*, vol. 300, pp. 250–264, 2007.

[88] B. Yang and C. D. Mote Jr., "On time delay in non-collocated control of flexible mechanical systems," *J. Dynamic Systems, Measurement and Control*, vol. 114, pp. 409–415, 1992.

[89] C. Zhang, D. Arnold, N. Ghods, A. A. Siranosian, and M. Krstic, "Source seeking with nonholonomic unicycle without position measurement and with tuning of forward velocity," *Sys. and Cont. Letters*, vol. 56, pp. 245–252, 2007.

[90] F. Zhang, D. M. Dawson, M. S. de Quieroz, and P. Vedagarbha, "Boundary control of the Timoshenko beam with free-end mass/intertia," *IEEE Conference on Decision and Control*, 1997.

[91] H. L. Zhao, K. S. Liu, and C. G. Zhang, "Stability for the Timoshenko beam system with local Kelvin-Voigt damping," *Acta Mathematica Sinica, English Series*, 2004, published online at `www.ActaMath.com`.